Universitat
Autònoma
de Barcelona

Exploring Arterial Dynamics and Structures in IntraVascular UltraSound Sequences

A dissertation submitted by **Aura Hernàndez i Sabaté** at Universitat Autònoma de Barcelona to fulfil the degree of **Doctora en Informàtica**.

Bellaterra, July 2009

Director: **Dra. Debora Gil Resina**
Universitat Autònoma de Barcelona
Dep. Ciències de la Computació i Centre de Visió per Computador

This document was typeset by the author using LaTeX 2_ε.

The research described in this book was carried out at the Computer Vision Center, Universitat Autònoma de Barcelona.

ISBN 978-84-937261-6-4

Printed by Ediciones Gráficas Rey, S.L.

Al Lluís i els meus pares
Gràcies per ser-hi sempre

Agraïments

L'obtenció del títol de doctora implica assolir el grau acadèmic més alt. Ja he acabat d'estudiar? Potser des del punt de vista acadèmic sí, però segurament no des de cap altre. Durant aquests 6 anys, que es compliran el dia que defensi aquest treball, he après moltíssimes coses a nivell acadèmic, però també a molts altres nivells, sobretot el personal. Ha estat una etapa que s'ha fet llarga a èpoques i molt curta a d'altres.

Una etapa amb llargues hores de discussió per intentar que el món de les ecografies intra-coronàries, entre d'altres, sigui una mica més planer. Hores en que la foscor semblava guanyar terreny i hores en què el cel era a tocar. Però per sobre de tot, hores de dedicació i entusiasme on he après que la intuïció i la perseverança et porten per bons camins. Una etapa acompanyada de tot tipus de persones. Persones que m'han transmès la seva passió per la investigació. Persones que sempre tenen un moment per discutir de qualsevol cosa, ja sigui sobre mètodes de comparació múltiple o de si els de l'obra del davant posen en perill les nostres vides. Hores també de despatx on, a part de treballar i discutir si és millor el windows o el linux, hem fet pessebres, hem rigut, ens hem renyat i hem discutit sobre el nostre futur. He conviscut el dia a dia amb grans persones, que m'han ensenyat a respectar més els altres, que m'han cuidat en els moments baixos i que m'han enriquit amb les seves visions de la vida.

Aquesta etapa també ha tingut les seves hores de docència. Hores en contacte amb alumnes de 20 anys (i alguns més), que et contagien les ganes de menjar-se el món i et recorden que la vida són dos dies i que cal viure-la. Però les classes no haguessin estat les mateixes sense la preparació prèvia. Preparació enriquida amb els diferents punts de vista sobre la filosofia docent. Intercanvis d'opinions vàries sobre quin és el millor mètode a seguir perquè els alumnes aprenguin, perquè no copiïn, perquè no es rebel·lin... i no oblidem les batalletes explicades pels més experts en la matèria, de qui s'aprèn més!

Totes aquestes hores, a vegades més de les que toca, han ocupat la meva jornada laboral. I moltes hores també han estat fora d'aquesta, ja sigui a l'hora de dinar o fent un cafè. Però a l'hora de dinar intentem desconnectar de la recerca i la docència i riure una mica del veí. D'això se n'han encarregat molt bé alguns grans amics i unes bones orelles. Alguns han vingut més tard, altres ja han marxat, altres han vingut de pas i altres vénen de tant en tant, però el requisit principal és saber riure de qualsevol cosa i voler passar una bona estona. Al cap i a la fi, darrere d'aquests escarnis hi ha males persones que van de bones persones que van de males persones. O no era així?!

I també han estat molts cigarrets! Tot i que fa més d'un any que no fumo, ha

estat molt quitrà consumit, controlant les obres i arreglant el món, sempre molt ben acompanyada de persones que, com jo, buscaven 10 minuts per respirar "aire pur". Persones que m'han animat a posar aquests agraïments. Persones que, tot i no fumar, m'acompanyaven mentre feien el cafè, tot mostrant-me amb les seves experiències que la vida no és en blanc i negre, sinó que té 256 nivells de gris i cal pensar en el futur. Amics que saben apreciar una bona caminada pel campus i una bona xocolata i que saps que són allà en moments importants de la teva vida.

Resumint, durant aquests anys he conegut i retrobat grans persones. Persones que han confiat en mi. Persones que m'han fet riure i persones que m'han fet plorar. Persones que sorprenen i persones que apareixen quan menys t'ho esperes. En definitiva, persones que no m'han deixat indiferent al llarg d'aquesta etapa i que m'han ajudat, d'una manera o d'una altra, a créixer en molts aspectes.

Però abans d'aquesta etapa ja hi havia grans persones. Amigues que encara no saben exactament el que faig o que creuen que perdo el temps, però que tot i així em donen suport sempre que el necessito i comparteixen les meves alegries sempre que es pot. Familiars que creuen que faig coses molt rares o que gràcies a mi no es volen dedicar al món de la investigació, però que també estan allà quan cal, ja sigui per escoltar o per celebrar. Com a familiar especial he de parlar del meu fill adoptiu, que també ha estat pels detalls matemàtics que jo ja he oblidat o per escoltar-me quan és necessari. I no m'oblido de les persones més importants de la meva vida fins al moment, els meus pares i el Lluís, que han cregut en mi des del primer moment i han tingut la paciència d'escoltar-me i aguantar-me durant tots aquests anys.

És per tot això que us dono les gràcies a totes les persones que, en els moments més baixos d'aquesta història, heu estat allà, d'una forma o una altra, però també a totes les que heu sabut gaudir dels seus moments àlgids i heu compartit amb mi la seva celebració.

Resum

Les malalties cardiovasculars són una de les principals causes de mortalitat als països desenvolupats. La majoria d'elles són degudes a malalties arterials (especialment les coronàries), que vénen causades per l'acumulació de placa. Aquesta patologia estreny el flux sanguini (estenosi) i afecta les propietats elàstiques i bio-mecàniques (arteriosclerosi) de les artèries. En les últimes dècades, l'Ecografia Intra-Coronària (EIC) ha esdevingut una tècnica usual de diagnòstic per la imatge i seguiment de les malalties coronàries. L'EIC està basada en un cateterisme que mostra una seqüència d'imatges corresponents a seccions de l'artèria sota estudi. La inspecció visual de cadascuna d'aquestes imatges proporciona informació sobre el percentatge d'estenosi, mentre que la inspecció de les vistes longitudinals propociona informació sobre les propietats bio-mecàniques, que pot prevenir un desenllaç fatal de la malaltia cardiovascular. Per una banda, la dinàmica arterial (deguda al batec del cor, entre d'altres) és un dels principals artefactes per poder explorar les propietats biomecàniques. Al mateix temps, les mesures manuals d'estenosi requereixen un traçat manual de les vores del vas, tasca feixuga que consumeix molt de temps i que pot patir variabilitat entre observadors.

Aquesta tesi proposa vàries eines de processament d'imatge per explorar la dinàmica de les artèries i les seves estructures. Presentem un model físic per extreure, analitzar i corregir la dinàmica rígida transversal dels vasos i per recuperar la fase cardíaca. A més, introduïm un mètode estadístic-determinista per a la detecció automàtica de les vores del vas. En particular, l'enfoquem a segmentar l'adventícia. Un protocol de validació acurat per assegurar una aplicació clínica fiable del mètodes és un pas crucial en qualsevol proposta d'algorisme. En aquesta tesi tenim especial cura de dissenyar protocols de validació per a cadascuna de les tècniques proposades i contribuïm a la validació de la dinàmica *in vivo* amb un indicador objectiu i quantitatiu per mesurar la quantitat de moviment suprimida.

Abstract

Cardiovascular diseases are a leading cause of death in developed countries. Most of them are caused by arterial (specially coronary) diseases, mainly caused by plaque accumulation. Such pathology narrows blood flow (stenosis) and affects artery bio-mechanical elastic properties (atherosclerosis). In the last decades, IntraVascular UltraSound (IVUS) has become a usual imaging technique for the diagnosis and follow up of arterial diseases. IVUS is a catheter-based imaging technique which shows a sequence of cross sections of the artery under study. Inspection of a single image gives information about the percentage of stenosis. Meanwhile, inspection of longitudinal views provides information about artery bio-mechanical properties, which can prevent a fatal outcome of the cardiovascular disease. On one hand, dynamics of arteries (due to heart pumping among others) is a major artifact for exploring tissue bio-mechanical properties. On the other one, manual stenosis measurements require a manual tracing of vessel borders, which is a time-consuming task and might suffer from inter-observer variations.

This PhD thesis proposes several image processing tools for exploring vessel dynamics and structures. We present a physics-based model to extract, analyze and correct vessel in-plane rigid dynamics and to retrieve cardiac phase. Furthermore, we introduce a deterministic-statistical method for automatic vessel borders detection. In particular, we address adventitia layer segmentation. An accurate validation protocol to ensure reliable clinical applicability of the methods is a crucial step in any proposal of an algorithm. In this thesis we take special care in designing a validation protocol for each approach proposed and we contribute to the *in vivo* dynamics validation with a quantitative and objective score to measure the amount of motion suppressed.

Contents

List of Tables

List of Figures

Introduction

There is general consensus that cardiovascular diseases (cerebrovascular, peripheral arterial, coronary heart, and strokes among others) are a leading cause of death. According to the World Health Organization[1], they constitute approximately a 30% of all global deaths and they are projected to remain the single leading causes of death. Among cardiovascular diseases, coronary heart pathologies (which can trigger anginas and heart strokes, for instance) constitute the gross of these deaths with a 33%.

Artery diseases are mainly caused by the accumulation of plaque (made up of a combination of blood cholesterol, fat and cells) inside arterial walls [1]. Such plaque accumulation narrows the artery's blood flow (stenosis) and makes arteries inflaming and being less flexible (atherosclerosis). Artery blood flow reduction is measured by the percentage of obstruction in vessel sections and is a usual measurement previous to decide which is the best treatment (either surgical or pharmacological) for an atherosclerotic lesion. Depending on the histological composition of the plaque, its (bio-mechanical) physical behavior will be different, making it more or less unstable (vulnerable plaques) and, thus, resulting in a different risk for the patient [2]. Early detection of plaque composition is a main step for planning the most suitable treatment (angioplasty, stent apposition, ...) and might prevent further thrombosis potentially leading to a fatal heart attack. Tissue bio-mechanical properties play an important role in the diagnosis and treatment of cardiovascular diseases. The main mechanical properties currently under study are radial strain, which is related to plaque type and vulnerability [3], and shear stress, which influences the probability of plaque accumulation [4]. Both measures can be computed by means of the study of vessel tissue deformation along the cardiac cycle.

IntraVascular UltraSound Imaging

IntraVascular UltraSound (IVUS) [5] is a wide used catheter-based technique which provides cross-sectional views of the artery. A guide wire with a catheter inside is threaded through the coronary artery under study. A catheter is composed of a Radio Frequency (RF) emitter and a transducer. The RF emitter sends ultrasound waves whose beams are reflected on arterial tissue particles and collected by the transducer. Images are reconstructed from the reflection of this signal, so, its grey level is related to

[1] `www.who.int`

tissue density of mass [6,7]. The catheter is mechanically pulled back with a constant velocity (usually at 0.5 mm/s) along the artery providing a sequence (digitized at 20-30 frames per second) of IVUS images.

Figure 1 shows a block of IVUS images obtained from a pullback (on the left) and the two kind of images derived from them (on the right). Each sequence frame (on the top right) shows a cross-section of the vessel under study with a complete detail of its morphology. It follows that inspection of IVUS images provides the physician a complete study of the vessel morphology, such as arterial wall layers, lumen area or plaque composition (stenosis assessment). The frames on the left can be intersected by a longitudinal plane including the catheter trajectory (grey plane on fig.1, left graphic), defined by a fixed angle on cross sections. The image obtained in this way is called longitudinal cut of the artery (bottom-right image). The longitudinal cut of the figure corresponds to 401 frames, while the 16 frames on the left correspond to a thin stripe of the whole longitudinal cut. Such views allow observing the evolution of the vessel along the pullback and, thus, their exploring reflects the arterial flexibility and tissue mechanical properties (atherosclerosis).

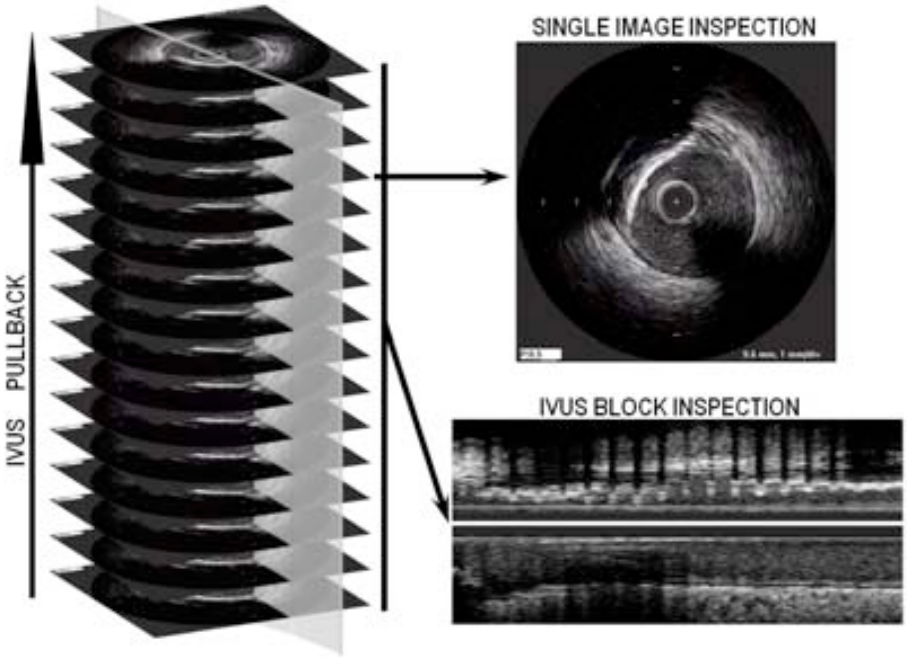

Figure 1: Images derived from an IVUS pullback. The left image is a block of 16 IVUS consecutive frames from a constant pullback. The right top image is a single cross-section of the vessel. The right bottom image is a longitudinal view obtained by intersecting 401 frames with the grey plane at the same angle.

Figure 2 shows the analogy between a cross-sectional histological cut of an artery (left image) and the corresponding IVUS image (right image). In muscular arteries, like coronary arteries, there are frequently three layers [8]. The innermost layer con-

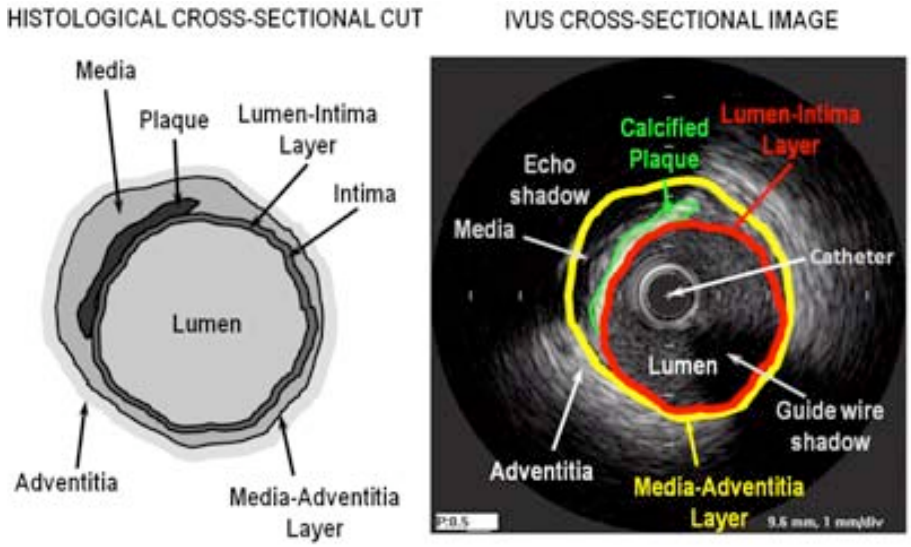

Figure 2: IntraVascular UltraSound single image inspection. On the left, a cross-sectional histological cut of the vessel with its most frequent vessel structures. On the right, its corresponding cross-sectional IVUS image.

sists of a set of three elements: intima, atheroma (in diseased vessels), and internal elastic membrane. Moving outward from the lumen (the inside space where blood flows), the second layer is the media, which is usually less homogeneous than the intima. The third and outer layer consists of the adventitia and peri-adventitial tissues. The membrane separating the second and the third layers corresponds to the external elastic membrane (EEM). Vessel plaque accumulates between intima and media. Depending on the disease of the artery, there exist different kind of plaques: calcified, soft, fibrous, and mixed plaque. On the right side of figure 2 we have the visualization of the layers and plaque in an IVUS cross-section. The contour between lumen and intima, depicted in red, corresponds to the internal elastic membrane. The trailing edge of the intima cannot always be distinguished clearly because in some cases the media may appear artifactually thin because of an intense reflection from the intima or external elastic membrane. In the IVUS image of fig.2, the intima-media layer is not visible. However, a discrete interface at the border between the media and the adventitia is almost invariably present within IVUS images and corresponds closely to the location of the EEM, which is colored in yellow. There is no distinct boundary on IVUS images separating the true adventitia from surrounding perivascular tissues. Regarding plaque, its intensity increases proportionally to its density of mass, so that, soft, fibrous and calcium appear with increasing brightness. In the IVUS image of fig.2, there is a calcified plaque (colored in green) in the second quadrant. The differential feature of calcium is the echo shadow behind it due to its echo opacity. Another shadow usually observed in an IVUS image is the artifact produced by the guide wire reflection (in the fourth quadrant of the image).

The qualitative description of the artery provided by IVUS images enables the

assessment of several measurements such as stenosis, EEM and lumen areas. The percentage of stenosis is computed as the ratio between the area of the lumen and the area of the EEM times 100. Lumen measurements are performed using the interface between the lumen and the leading edge of the intima. All these measurements require an accurate segmentation of vessel borders for the whole sequence block. For a segment of 25 mm. long, it implies exploring about 5000-7500 frames (depending on the frame rate) in a standard intervention. Such huge amount of frames implies that an exhaustive quantitative manual exploring is not feasible in clinical practice. Furthermore, by the low image quality due to speckle noise, a manual processing, apart from being a tedious time consuming task, might suffer from intra- and inter- observer variability. Artifacts such as shadow caused by the catheter guide wire or shadows caused by calcium reflection, hinders performance of standard image processing techniques. This has motivated intensive research for developing segmentation algorithms as automatic as possible.

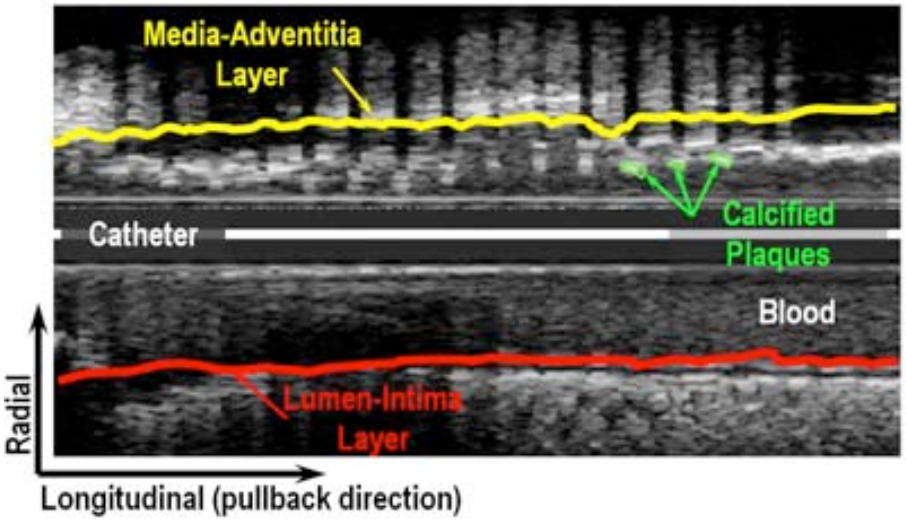

Figure 3: Longitudinal Cut of an IVUS Sequence showing the behavior of the main vessel structures pointed out on the above single image.

Figure 3 shows a longitudinal view of the vessel. The horizontal axis correspond to the pullback direction and the vertical axis to the radial direction of an IVUS frame. Vessel layers are colored as is figure 2. Longitudinal views allow exploring the behavior of the vessel along the pullback for the assessment of radial deformation and elastic properties of structures. Unlike other vascular structures, coronary arteries are placed on the heart surface, partially embedded on the epicardial surface of the cardiac muscles. Heart beating, pulsatile blood flow and intrinsic properties (anatomical, mechanical, physiological and so on) of the vessel, added to breathing of the patient endow the artery with a dynamical behavior. Vessel dynamics during *in vivo* pullbacks and the complex motion of the imaging catheter inside the coronary vessels result in longitudinal and in-plane motion artifacts during the acquisitions.

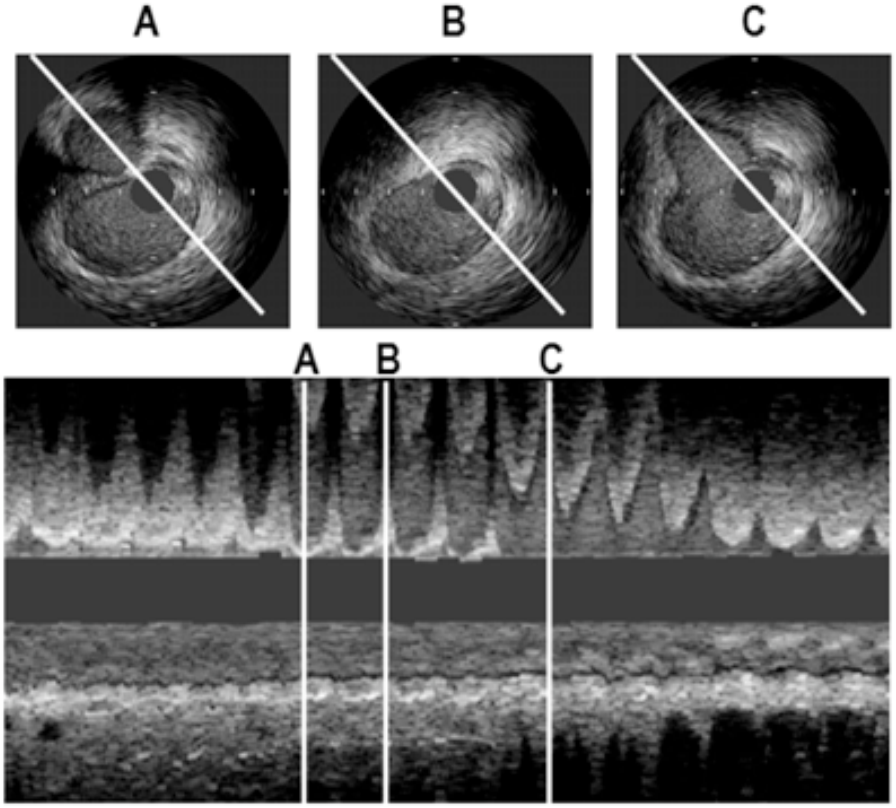

Figure 4: Swinging effect in longitudinal cuts. White lines at the same angle in frames A, B, C (top images) correspond to the vertical lines in the longitudinal cut (bottom image). The swinging bifurcation can be clearly noticed in both, cross-sections and longitudinal cut.

Forward and backward longitudinal translation along the catheter axis [9] results in a swinging effect on the reconstructed images. Such swinging motion produces a sequence block with spatially shuffled frames. The shuffled sequence does not provide a faithful 3D reconstruction, hinders volumetric measurements and affect the appearance of longitudinal views. Figure 4 illustrates the swinging effect caused by off-plane dynamics. At the upper side of the figure, there are three IVUS images at different pullback times. Image A shows a bifurcation on the 2nd quadrant of the image, which disappears in image B and reappears closer to the main artery in image C. The white lines at the same angle on both images correspond to the white lines on the longitudinal cut at the bottom side of the figure, one for each frame. The swinging bifurcation is clearly noticed in the upper profile of this longitudinal cut.

Vessel-catheter in-plane rigid dynamics introduces a misalignment of vessel structures between frames of a sequence block. This artifact causes a saw-tooth shape appearance in longitudinal views and troubles tracking vessel deformation for evalua-

tion of tissue elastic and bio-mechanical properties. Furthermore, it hinders a proper 3D exploring, both, visualization, accuracy of volumetric measurements, and plaque analysis along the sequence [10]. Figure 5 illustrates artifacts induced by in-plane dynamics. The upper profile shows the saw-tooth-shape pattern of the vessel intima wall (dark line) introduced by relative vessel-catheter translation. The bottom profile presents a structure misalignment due to the relative vessel-catheter rotation for an echo-shadowing calcified plaque.

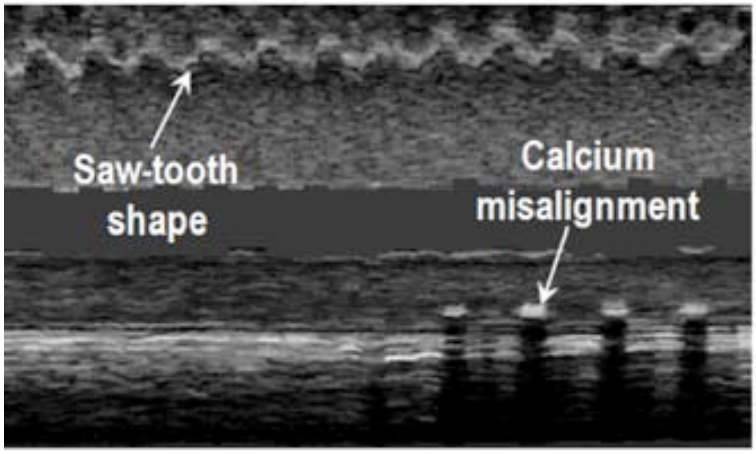

Figure 5: Artifacts in longitudinal cut appearance induced by in-plane dynamics.

Goal of the Thesis

The goal of this work is to develop image processing tools for improving cardiovascular disease diagnoses through the analysis of IVUS sequences. It will cover the following points:

1. **Vessel Dynamics Exploring:** In order to extract bio-mechanical properties and improve vessel physical properties evaluation, we propose an approach to extract, analyze and correct vessel rigid in-plane dynamics. As well, since the swinging effect produced by cardiac motion hinders volumetric measurements, we introduce a first approach to image based ECG gating.

2. **Vessel Structures Exploring:** In order to avoid the time consuming tasks of manual vessel wall segmentation for stenosis measurements, we propose an automatic approach to segment the media-adventitia layer.

3. **Validation Protocols:** Validation of any algorithm is an essential issue for supporting their validity and applicability in clinical practice. Checking the accuracy of the methods allows the evaluation of their performance, bringing up their strengths and limitations. In medical imaging, validation is not easy

to carry out for *in vivo* data. For each contribution we design specific protocols taking special care of *in vivo* assessment.

Vessel Dynamics Exploring

We have split dynamics exploring in longitudinal and in-plane motion estimation

1. Longitudinal Motion

A usual way to minimize the impact of longitudinal motion artifacts is the use of ECG-gated devices [11] and ECG gating methods [12, 13]. Both of them return a static sequence by either capturing frames synchronized with heart dynamics [11] or discarding those frames not synchronized with it [12, 13]. Synchronization can be performed either on-line during acquisitions [12] or off-line by processing a standard non-gated sequence [13]. On-line procedures require a specific hardware (not always available) for acquiring frames at end-diastole. Off-line techniques require delicate processes of the ECG signal for extracting a sequence sampling synchronized at end-diastole given by ECG-peaks. In any case, a simultaneous acquisition of IVUS images and ECG-signal is required. However, such acquisition is not supported by all commercial devices and forces the introduction of two different catheters in the artery which makes the intervention more invasive. Furthermore, without a 4D model of the artery [14], these techniques only provide a reliable static model of the artery at end diastole.

Although IVUS images dynamics, such as lumen area extrema, reflect cardiac motion, the potential of IVUS images processing for retrieving cardiac phase from non-gated sequences without ECG-signal still remains little explored. Existing strategies [15, 16, 17, 18, 19] follow the scheme sketched in figure 6. First, a signal reflecting

Figure 6: Pipeline for Image-based Cardiac Phase Retrieval

cardiac motion is computed from IVUS sequences. Second, the signal is filtered (in the Fourier domain) in order to remove non-cardiac phenomena and artifacts. Finally, suitable sampling of the filtered signal retrieve cardiac phase. According to clinical reports [20], maximum and minimum lumen areas correspond to end-systole and end-diastole. By the physical coupling [21], lumen area evolution is related to other phenomena induced by cardiac motion, such as the evolution along the sequence of tissue density of mass. All authors agree in using the extrema of filtered signals for sampling at end-systole and diastole. The main differences among existing algorithms and thus, the clue for an accurate cardiac phase retrieval, are on the signal computed from the sequence and the filter used to extract the cardiac profile.

Cardiac phase is obtained by exploring the temporal changes of either vessel structures (which needs its previous segmentation [15, 16, 19]) or image grey-level (which

requires a high dimensional feature space to detect coincident frames [18, 17]). Nadkarni et al. [15] bases their approach on the changes of lumen size. Zhu et al [16] propose two different methods, based on average intensity and absolute intensity difference of images along the sequence, to extract the signal containing cardiac phase. Barajas et al [19] use longitudinal cuts to detect any change in structure, morphology or plaque prone to be related to cardiac frequency. Meanwhile, Matsumoto et al. [17] also study different standard similarity measures along the sequence to compute a signal, which is further filtered using wavelets for cardiac profile retrieval. Besides, O'Malley et al [18] bases their method on pairwise frames comparisons by normalized cross-correlation. Regarding the filter used, all approaches agree to using a band-pass filter, which band width and profile is crucial for a proper phase retrieval in large segments. Current approaches use wavelets filters such as Gabor [19], Butterworth [16] and Daubechies [17]. An analysis of the best filter and band-width has not been addressed so far.

2. In-plane Rigid Motion

ECG-gated models are suitable for volumetric measurements, visualization and palpography techniques measuring peak tissue deformation at different intraluminal pressures [22]. Nevertheless, for studying the compliance of the vessel wall [23, 20, 24], as well as determining tissue elastic properties [25, 22], the information of IVUS images during a cardiac cycle is required. In this case, image misalignment due to in-plane motion should be compensated.

Current approaches for motion compensation in IVUS work on three main domains: image intensity [22, 26], vessel geometric appearance [25] and radio frequency (RF) signal [27]. Intensity based approaches rely on either registration [22] or tracking [26] strategies. In the case of large displacements, tracking [26] fails to yield the expected results, while registration [28] requires exhaustive (computationally inefficient) search of the parametric space. Moreover, changes in image intensity from one frame to the next one substantially affect the performance of intensity-based algorithms. Explicit formulae of motion parameters overcome the limitation of capture range, while the impact of morphological changes is reduced by including geometric considerations to the algorithm. In this fashion, the motion artifact reduction developed in [25] achieves good results, as long as, only catheter translation compensation is required. An alternate way of dealing with image intensity changes is considering the RF signal [27]. On one hand, although IVUS images are reconstructed from RF signals, not all IVUS devices allow recording and exporting such signals. On the other one, vessel translation is given by the difference between the position of the center of the catheter and the center of the vessel. Since the RF domain is defined in polar coordinates centered at the catheter, translations are not straightforward and, in fact, existing algorithms based on RF signals only address rotations.

Our Contribution - Physics-based models

The following contributions are proposed for estimating (and compensating) vessel dynamics.

1. Longitudinal Motion

Following the scheme adopted by most of the existing models (see scheme of fig. 6), we approach the first two steps. First, we extract a signal reflecting motion and then we filter it for extracting the cardiac profile. Two different approaches for extracting a signal reflecting cardiac motion are presented: one based on the angle of rotation and another one based on the grey-level local mean. Vessel dynamics is the contribution of three main phenomena, in particular heart beat. It follows that the angle of rotation profile contains information about heart phase. Since in ultrasonic images, pixel intensity reflects the density of mass, the image Local Mean (LM) detects changes in vessel appearance along the sequence. Such changes along the sequences are a consequence of cardiac motion and morphological changes. Regarding the filter used to remove noise and non-cardiac phenomena from cardiac signals, two families of band-pass filters are proposed: Gaussian and Butterworth. For the first time we address determining which strategy for cardiac phase retrieval is better suited, in terms of a statistically significant better performance.

2. In-plane Rigid Motion

We model rigid in-plane dynamics as a rigid body motion [29]. Such motion is given by a translation followed by a rotation. Explicit formulae for motion parameters is provided by combining vessel appearance and shape. The algorithm takes into account vessel geometry appearance for defining translation. In this manner, the method supports morphological changes. By estimating rotation between consecutive frames in the Fourier domain, the model has no limits on capture range. We show that the main contributions to rigid dynamics are heart pumping, breathing of the patient and vessel geometry. We provide a motion decomposition that decouples cardiac signal from breathing motion and geometric evolution.

Vessel Structures Segmentation

Since the early years, many algorithms for a reliable intima detection have been proposed [30, 31, 32, 33, 34, 35, 36, 37, 38, 39, 40, 41]. By its inherent difficulty (its distance from the transducer reduces sharpness in the border visual appearance), adventitia modeling has been more limited [42, 43, 44, 45, 46, 47, 48, 49]. An accurate border detection requires either elaborated strategies in the case of contour based segmentations [46, 47, 48, 49, 50], or a previous plaque and tissue characterization in the case of classification strategies [44].

Usual techniques addressing segmentation of vessel contours (intima and adventitia) rely on a single local image descriptor (usually edges) to guide a snake towards the target structures [30, 31, 32, 33, 44, 45, 46, 47, 48, 49, 51, 52]. Regardless of low quality in IVUS images, adventitia detection adds the difficulty of a large variety of descriptors, a weak visual appearance by a decrease in the ultrasonic pulse energy [7] and incomplete contours due to echo opaque plaques (e.g. calcium) shadowing. It follows that standard segmentation approaches do not suffice by their own and need exclusive strategies to yield proper results. Some authors [30, 31, 32, 49] combine transversal and

longitudinal contours to endow the model with spatial continuity along the sequence. In this case, the use of ECG-gated sequences [32, 33] significantly helps to achieve a reliable segmentation of longitudinal cuts. Other approaches [34,37] manually restrict a region of interest that serves to initialize a snake, although such initialization might need to be updated along the sequence.

A common inconvenience of segmentations based on contour detection is that they require some kind of image filtering to avoid fake responses. The poor image quality as well as large variety of IVUS artifacts (calcium, side-branches, shadows, catheter guide and blood back scatter) make standard anisotropic smoothing [53] fail to achieve optimal results. In order to overcome these drawbacks, several approaches have been proposed. The most simple strategy is to discard those images containing too much artifacts [46]. Although this is a practical way of filtering, it runs the risk of losing too much information for a reliable recovery of vessel borders. Others [38, 54], directly handle radio frequency data and filter impulse responses of the transducer. Unfortunately, raw data acquisition needs of a special device not always available in standard clinical equipments.

Recent approaches [38, 42, 43, 44, 45, 55] use classification strategies to better characterize coronary structures (plaque and vessel borders). Although results are robust to noise and artifacts, most of them [38, 44] require plaque classification to yield, as a side result, lumen and media-adventitia segmentation. The only statistical proposal that directly handles vessel borders detection is discriminant snakes [55], which extract the *a priori* knowledge for the segmentation of the current frame from the previous segmented image. Although they are well suited for border tracking (thus avoiding any interaction along the sequence), they require an accurate segmentation of the first sequence frame for each different case.

Our Contribution - A Deterministic-Statistical Strategy

Vessel borders detection should serve to characterize and quantify vessel plaque rather than follow as a side result of a laborious plaque classification. A robust adventitia segmentation should combine classification strategies with advanced filtering and segmentation techniques [56]. In this thesis, we present a deterministic-statistical strategy for computing medial-adventitia border segmentation.

The strategy we propose is a three-fold algorithm: 1) preprocessing of IVUS images, 2) selection of points on the vessel border and 3) segmentation of the extracted points.

- In the preprocessing step, we present two different filters for sharpen vessel borders appearance in the polar transform of each IVUS frame. The first filter is based on a restricted anisotropic diffusion [57], whereas the second one profits the method presented for suppressing in-plane rigid motion.

- Supervised classification techniques serve to compute 2 binary images: one for calcium sectors and another one for vessel borders. The first image is a mask that discards sectors of ambiguous information. The second one is a collection of fragmented vessel segments that are modeled by computing an implicit closed representation and, then, an explicit B-spline parameterization.

- An anisotropic contour closing [58] yields the implicit closed model of vessel segments conforming to the Gestalt principles of good continuation and avoiding interpolation at calcium and side-branches sectors. Parametric B-spline snake with the initial snake at the outer radius are used to compute the final explicit compact model.

Validation Protocols

In general, a validation protocol should address two main issues: **what** we want to validate (ground truth) and **how** we want to validate it (goodness measure and statistics).

The first question refers to the definition of the *ground truth* or *gold standard*. The main difficulty in medical imaging is that ground truth might not be always available [59] or might suffer from inter- and intra- observer variability. In the case of vessel dynamics estimation, ground truth cannot be easily extracted from *in vivo* images. Current solutions, base validation on either synthetic experiments or quantities reflecting motion. Synthetic data is usually produced by means of mechanical phantoms [26,60,61]. Dynamic physical phantoms require an equipment not available at all laboratories. Besides, we note that dynamic physical phantoms are prone to have two sources of errors: one due to the phantom device and another one introduced by the motion correcting algorithm. Concerning quantities reflecting motion, physical scores obtained by another device [60] or implantation of biological markers [62] are commonly used. Implantation of biological markers is an invasive technique that might not be used in human subjects. Meanwhile, measurements of quantities reflecting motion from other devices are not always feasible. In the case of anatomical structures segmentation, ground truth is defined by manual identification of vessel structures. Since manual identifications are prone to vary across observers, they provide a multiple ground truth. This implies that an analysis of automated errors might not reflect, by its own, the true accuracy of segmentations, since a large variation range might be caused by a significant difference among expert models. A standard way [63] of overcoming the above phenomena is by comparing automated errors to the variability among different manual segmentations (inter-observer variability).

The second question involves defining a suitable "goodness" score providing a reliable measure of the quality of the algorithm we are evaluating [64]. Such index can be either a qualitative (subjective) score, usually obtained by a visual inspection of processed images [12], or a quantitative (objective) measure. In the case of dynamics assessment, in real pullbacks there is no objective error measure indicating the amount of motion suppressed, since motion parameters are unknown. In most cases, quality measures are either subjective measures, based on the visual appearance of sequences and longitudinal cuts [65,13] or rely on extraction of vessel properties (such as strain in [22, 66]). In the case of structures segmentation, comparison to manual results [67, 68, 38, 45, 43, 42, 46, 52, 51, 39] or other measurements as a reference [69, 60] are widely used. Comparison between estimated quantities and ground truth can be done by using Haussdorff or Euclidean distances and might compare areas, means, variances, standard deviations among others [64]. Statistical analysis of such distances

determine if differences between ground truth and estimated quantities are significative or not. The most used statistics are T-Student test, Kolmogorov-Smirnof test and confidence intervals. Correlation also indicates the relationship between ground truth and estimated quantities and it is widely used [69, 60, 61, 67].

Our Contribution - *In-vivo* Protocol Design

In this PhD thesis, we take special care in defining an objective validation protocol for each of the issues addressed along the document in order to ensure a wide clinical applicability.

- For assessing in-plane dynamics, we have created computational phantoms, which parameters define our ground truth. They have been created by applying rigid motion profiles to still sequences distilled from *in vivo* pullbacks. In order to show that the performance of our algorithm is independent of the angular range considered, we have considered synthetic motion profiles sampled to emulate a frame to frame rotational artifact ranging of 1 and 10 degrees. In order to produce motions as realistic as possible (and not simply a perfect, even if noise is added, synthetic profile) we use motion parameters extracted from *in vivo* sequences. In order to ensure accuracy for any vessel, our phantoms cover different morphologies. In the case of *in vivo* sequences we introduce a novel quantitative score, the Conservation of Density Rate (CDR). The score bases on the grounds of fluid mechanics conservation laws [70] and quantifies the changes that the local density of mass (given by the image local mean) undergoes along the sequence before and after motion compensation. Its correlation to motion parameters accuracy is assessed on computational phantoms.

- For assessing longitudinal dynamics, manual samplings of sequences constitute our ground truth. Since maximum and minimum lumen areas are related to cardiac phase, those frames achieving extrema lumen areas in longitudinal cuts have been selected by an observer. Distances between automatic and manual samplings are our goodness measure which ranges are given in terms of means and variances. We use the Nemenyi test to determine which of the proposed strategies is the best for cardiac phase retrieval in terms of a significant statistical difference.

- For assessing adventitia segmentation, ground truth has been defined by manual tracings on IVUS images. In this case, four experts have been considered. Inter-observer variability has been measured by obtaining the error measures between two different observers. The quality measures used for validating this strategy are absolute and signed distances and area differences A Student t-test determines if there is any significant difference between manual and automatic segmentations.

The remains of this thesis are organized as follows. Chapter 1 introduces the main theoretical mathematical concepts supporting the methods developed along this work. Chapter 2 explains the contributions approaching artery rigid dynamics (in-plane and longitudinal) compensation. Chapter 3 details our deterministic-statistic strategy for exploring vessel structures. Chapter 4 describes validation protocols for each of the theoretical contribution (in-plane dynamics, longitudinal motion and adventitia segmentation). The experiments and discussion are presented in Chapter 5, and, finally, conclusions and further lines are outlined at the end of the thesis.

Chapter 1

Theoretical Issues

In this chapter we introduce the theoretical mathematical knowledge used along the thesis. Section 1.1 explains the main transformations that vessels undergo. Fourier development appears in many image processing tasks and it is used for estimating the angle of rotation and it is detailed in 1.2 The processes and equations given in section 1.3 are used for smoothing IVUS images in the strategy for vessel structures segmentation and recovering (completing) unconnected contours. For a compact model of the adventitia contour a snake is required and it is introduced in section 1.4. Finally, propositions supporting the theory of the chapter are proved in section 1.5.

1.1 Affine Maps

The dynamics of coronary arteries is mainly governed by the left ventricle motion, blood pressure, and artery geometric properties [71, 21, 72]. The first order approximation to vessel dynamics is given by a linear transformation combining translation, rotation, and scaling [73]. All of them are particular cases of affine maps. This section formally describes the formulation as well as several properties useful for image processing.

Affine transformations (rotations, translations and scalings) model any linear map between images. Mathematically, they transform affine spaces. An *affine space* ($\mathbb{R}^n$) is described by means of a set of points E and a vector space. If we fix a point $O \in E$, as *origin of coordinates* and a basis of the vectorial space $V : \{\vec{e_1}, \ldots, \vec{e_n}\}$, known as *axis of coordinates*, the set $S = \{O; \vec{e_1}, \ldots, \vec{e_n}\}$ is known as *affine reference system*.

Given an affine reference system, S, it associates to any point $P \in E$ *n affine coordinates*, $(x_1, \ldots, x_n)$ given by decomposing the vector $\overrightarrow{OP}$ in the basis vectors $\{\vec{e_1}, \ldots, \vec{e_n}\}$ (see figure 1.1):

$$\overrightarrow{OP} = (x_1, \ldots, x_n) = \sum_{i=1}^{n} x_i \vec{e_i}$$

or equivalently:

$$P = O + \sum_{i=1}^{n} x_i \vec{e_i}$$

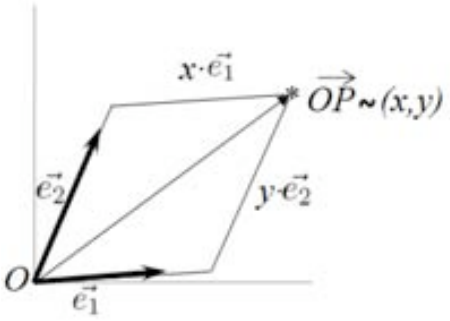

Figure 1.1: Affine Coordinates of a point $P \sim (x, y)$

In the above terms, an *affine transformation* $f : E \to E$ is defined as a linear map which transforms one affine reference system onto another one. Let $S = \{O; \vec{e_1}, \vec{e_2}\}$ and $S' = \{O'; \vec{e_1'}, \vec{e_2'}\}$ be two different affine reference systems. The affine transformation which transforms the points $(x, y) \in S$ of the first system to the points $(x', y') \in S'$ of the second one, can be written as:

$$\begin{pmatrix} x' \\ y' \end{pmatrix} = \begin{pmatrix} a_{11} & a_{12} \\ a_{21} & a_{22} \end{pmatrix} \cdot \begin{pmatrix} x \\ y \end{pmatrix} + \begin{pmatrix} t_1 \\ t_2 \end{pmatrix} = A \begin{pmatrix} x \\ y \end{pmatrix} + \vec{t} \tag{1.1}$$

As figure 1.2 illustrates, an affine transformation is a linear transformation mapping the axis $\{\vec{e_1}, \vec{e_2}\}$ onto $\{\vec{e_1'}, \vec{e_2'}\}$ followed by the translation, which moves the origin O to the other origin O'. The matrix $A : (\vec{e_1}, \vec{e_2}) \to (\vec{e_1'}, \vec{e_2'})$ corresponds to the transformation of the vectorial space:

$$A = \begin{pmatrix} < e_1, e_1' > & < e_1, e_2' > \\ < e_2, e_1' > & < e_2, e_2' > \end{pmatrix}$$

while $\vec{t} = O' - O$ corresponds to the translation of the origin of coordinates.

If A is a 2×2 real matrix, then by Jordan's theorem [74], it is similar to its Jordan canonical form. That is, there exist matrices Λ and Q, which satisfy:

$$A = Q \Lambda Q^{-1} \tag{1.2}$$

where Q is a coordinate change in the vectorial space given by ξ and η:

$$\xi = < e_1, \xi > e_1 + < e_2, \xi > e_2 = \xi_1 e_1 + \xi_2 e_2$$

$$\eta = < e_1, \eta > e_1 + < e_2, \eta > e_2 = \eta_1 e_1 + \eta_2 e_2$$

and Λ is the Jordan canonical form.

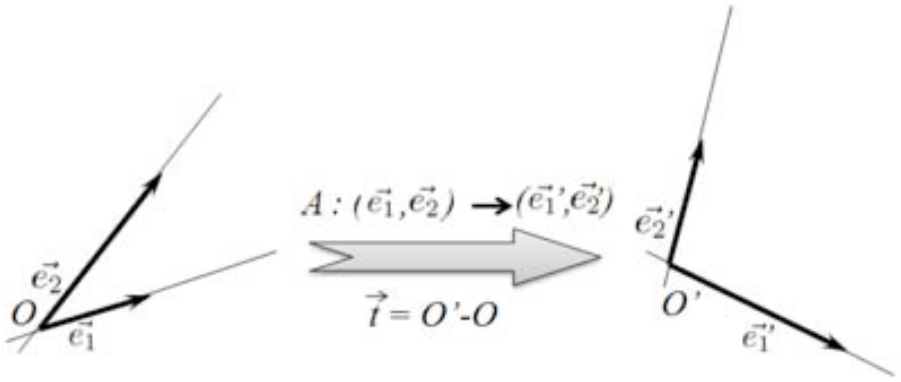

Figure 1.2: Affine Transformation

The matrix Λ can be classified by means of the eigenvalues of A, (λ_1, λ_2):

- In the case that $\lambda_1 \neq \lambda_2 \in \mathbb{R}$,

$$\Lambda = \begin{pmatrix} \lambda_1 & 0 \\ 0 & \lambda_2 \end{pmatrix}$$

  and A has two linear independent vectors e'_1, e'_2

- In the case that $\lambda_1 = \lambda_2 = \lambda \in \mathbb{R}$,

$$\Lambda = \begin{pmatrix} \lambda & 0 \\ 0 & \lambda \end{pmatrix}$$

  if there exist two linear independent eigenvectors, e'_1, e'_2, and

$$\Lambda = \begin{pmatrix} \lambda & 1 \\ 0 & \lambda \end{pmatrix}$$

  if there only exists one eigenvector, e'_1.

- In the case that eigenvalues are not real, $\lambda_1 = \overline{\lambda_2} \in \mathbb{C} \setminus \mathbb{R}$,

$$\Lambda = \begin{pmatrix} |\lambda_1| \cdot \cos(arg\lambda_1) & -|\lambda_1| \cdot \sin(arg\lambda_1) \\ |\lambda_1| \cdot \sin(arg\lambda_1) & |\lambda_1| \cdot \cos(arg\lambda_1) \end{pmatrix} \tag{1.3}$$

In the particular case that A is symmetric, it diagonalizes, since its eigenvalues are real and different, and, thus, its eigenvectors $\vec{\xi} = (\xi_1, \xi_2)$ and $\vec{\eta} = (\eta_1, \eta_2)$ are always linear independent vectors. In fact, they are orthonormal vectors, i.e. they satisfy $\vec{\eta} = \vec{\xi}^{\perp} (\Leftrightarrow (\eta_1, \eta_2) = (-\xi_2, \xi_1))$ and $\|\xi\| = 1$. It follows that Q satisfies $Q^{-1} = Q^t$ and it is a rotation of angle θ, for θ the angle between $\vec{\xi}$ and the first axis vector $\vec{e_1}$:

$$Q = \begin{pmatrix} cos\theta & -sin\theta \\ sin\theta & cos\theta \end{pmatrix}$$

In the case of arterial dynamics, the affine transformations involved are the following particular cases of the general equation (1.1):

1. **Translation**: In this case, A is the identity matrix, so that, the transformation is given by:

$$\begin{array}{rccc} T_{\vec{t}}: & \mathbb{R}^2 & \rightarrow & \mathbb{R}^2 \\ & (x,y) & \mapsto & (x,y)+(t_1,t_2) \end{array}$$

2. **Rotation**: In this case, $\vec{t}=(0,0)$ and the matrix A is a rotation:

$$\begin{array}{rccc} R_\theta: & \mathbb{R}^2 & \rightarrow & \mathbb{R}^2 \\ & (x,y) & \mapsto & \begin{pmatrix} cos\theta & -sin\theta \\ sin\theta & cos\theta \end{pmatrix} \cdot \begin{pmatrix} x \\ y \end{pmatrix} \end{array}$$

3. **Scaling**: In this case also $\vec{t}=(0,0)$ and $A=\Lambda$ is a diagonal matrix, which entries $\lambda=(\lambda_1,\lambda_2)$ are the scaling factor:

$$\begin{array}{rccc} \Lambda: & \mathbb{R}^2 & \rightarrow & \mathbb{R}^2 \\ & (x,y) & \mapsto & \begin{pmatrix} \lambda_1 & 0 \\ 0 & \lambda_2 \end{pmatrix} \cdot \begin{pmatrix} x \\ y \end{pmatrix} \end{array}$$

In the particular case of vessel in-plane dynamics, the main artifacts are rotational and translational (scaling is related to arterial physical properties). Rotation and translation are known as rigid motion since they do not alter shape size.

Rigid motion formulation simplifies in polar coordinates.

1.1.1 Affine Transformations in Polar Coordinates

Polar coordinates are defined by means of the distance to the origin (r) and the angle (α) with the first coordinate axis of the affine reference system. It follows that if (x,y) are the coordinates in the system $\{O;\vec{e_1},\vec{e_2}\}$, then their transform is given by:

$$\begin{cases} r=\sqrt{x^2+y^2} \\ \alpha=atan\left(\frac{y}{x}\right) \end{cases} \tag{1.4}$$

In the particular case of IVUS images, the origin is taken at the image center and the axis positively oriented (x-axis horizontally and y-axis vertically). Figure 1.3 shows an IVUS image in Cartesian coordinates on the left and in polar coordinates on the right. Arrows in both images shows the correspondence for angles at 90º, 180º and 270º in each reference system. Notice that the transducer converts into a straight line, as its center coincides with the center of the image. However, the circular shape of the media-adventitia layer converts into an undulated structure due to the distances of the border to the center of the image vary. Finally, the shadow of the catheter guide wire is radial in cartesian coordinates, so that is vertical in polar coordinates.

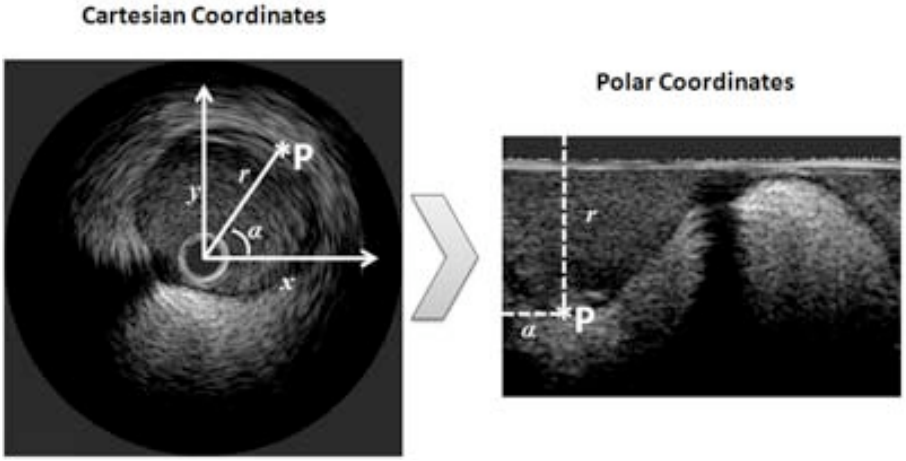

Figure 1.3: IVUS image in Cartesian (left) and polar (right) coordinates

In the case that a body undergoes a rotation and then a dilation, its correspondence in polar coordinates follows from the next proposition.

A rotation followed by an isotropic scaling ($\lambda_1 = \lambda_2 = \lambda$) corresponds to a translation of the angle and a radial scaling:

$$\begin{pmatrix} \tilde{x} \\ \tilde{y} \end{pmatrix} = \begin{pmatrix} \cos\theta & -\sin\theta \\ \sin\theta & \cos\theta \end{pmatrix} \cdot \begin{pmatrix} \lambda & 0 \\ 0 & \lambda \end{pmatrix} \cdot \begin{pmatrix} x \\ y \end{pmatrix} \Leftrightarrow \begin{cases} \tilde{r} = \lambda r \\ \tilde{\alpha} = \alpha + \theta \end{cases}$$

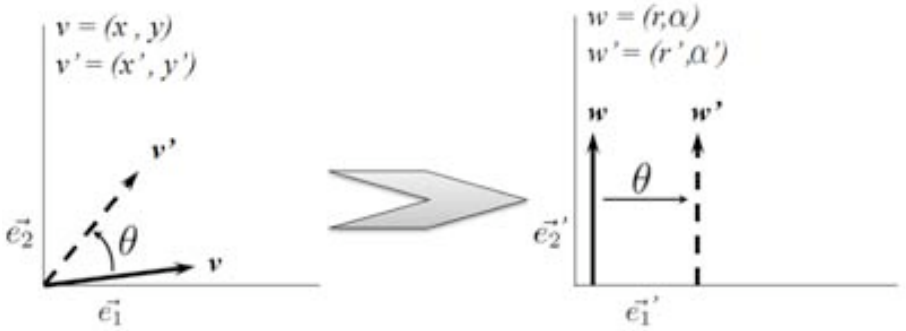

Figure 1.4: Conversion of a rotation in cartesian coordinates (left) to polar coordinates (right)

Figure 1.4 sketches the conversion of a rotation at center $(0, 0)$ from cartesian to polar coordinates. The vector v is rotated by an angle θ in cartesian coordinates on the left of the figure. The new vector v' (in dashed line) has the same modulus as v, $\|v\| = \sqrt{x^2 + y^2} = \|v'\| = \sqrt{(x')^2 + (y')^2}$, but $x \neq x'$ and $y \neq y'$. The formal proof can be found in proposition 1.5.1 in section 1.5.

1.2 Fourier Transform

The Fourier transform is widely used in image processing due to its properties. In particular, estimation of translation between two images is straightforward in terms of Fourier phase.

A periodic function is a function which repeats its values (a given pattern) in regular intervals. The interval of minimum length so that the pattern appears only once is called *period*. The number of times that the pattern occurs is called *frequency*. The basis of functions of period a (a-periodic) are the trigonometric functions $e^{\frac{2\pi in}{a}} = cos(\frac{2\pi n}{a}) + isin(\frac{2\pi n}{a})$. Therefore, any a-periodic signal $f \in L^2([-\frac{a}{2}, \frac{a}{2}])$ can be decomposed in this basis [75]:

$$f(x) = \sum_{n=-\infty}^{\infty} \langle f, e_n \rangle \cdot e_n = \sum_{n=-\infty}^{\infty} c_n e^{x \frac{in2\pi}{a}} \tag{1.5}$$

where

$$c_n = \frac{1}{a} \int_{-a/2}^{a/2} f(x) e^{-x \frac{in2\pi}{a}} dx$$

The right term of equation (1.5) is called *Fourier series* and c_n are called *Fourier coefficients*. Even if $f(x)$ is real-valued, the coefficients c_n are complex numbers.

A complex number, $k \in \mathbb{C}$, is determined by its module, $|k|$, and its argument, $arg(k)$:

$$k = |k| \cdot e^{2\pi i arg(k)} = |k| \cdot (cos(2\pi arg(k)) + isin(2\pi arg(k)))$$

$$\text{where} \begin{cases} |k| = \sqrt{Im(k)^2 + Re(k)^2} \\ arg(k) = \arctan\left(\frac{Im(k)}{Re(k)}\right) \end{cases}$$

for $Im(k)$ and $Re(k)$ the imaginary and real parts of k, respectively. Such decomposition is related to the amplitude (A) and the phase (ρ) of a signal. If a signal $f(x) \in \mathbb{C}$ of period $\frac{1}{b}$ has a single Fourier coefficient, k, $f(x)$ can be written as:

$$f(x) = k \cdot e^{2\pi ibx} = |k| \cdot e^{2\pi i arg(k)} \cdot e^{2\pi ibx} = |k| \cdot e^{2\pi ib\left(x + \frac{arg(k)}{b}\right)}$$

and its amplitude and its phase are:

$$A(f(x)) = |k| \qquad \rho(f(x)) = \frac{arg(k)}{b}$$

Figure 1.5 illustrates the amplitude and phase of the real part of two different functions:

$$f_1(x) = 3 \cdot e^{ix} \quad \text{and} \quad f_2(x) = 3 \cdot e^{i(x + \frac{\pi}{2})}$$

Both functions have the same amplitude, $A(f_1(x)) = A(f_2(x)) = 3$, and the same period, 2π. Meanwhile, their phase is different: $\rho(f_1(x)) = 0$ and $\rho(f_2(x)) = \frac{\pi}{2}$

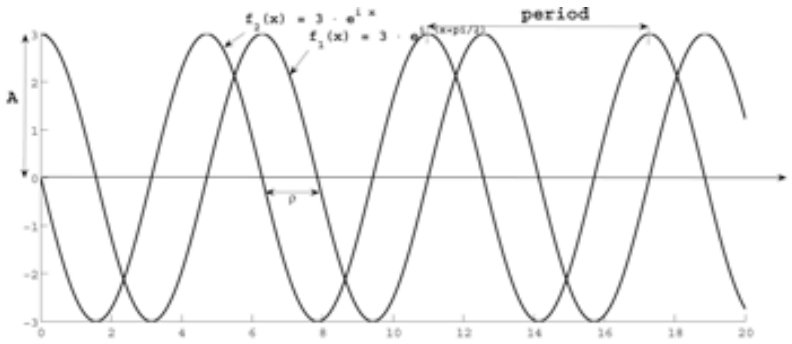

Figure 1.5: Phase and amplitude of a wave

In the case of a pure real function $f(x) \in \mathbb{R}$, since the Fourier coefficients satisfy that $\overline{c_n} = c_{-n}$,

$$f(x) = c_n \cdot e^{x\frac{2\pi in}{a}} + c_{-n} \cdot e^{-x\frac{2\pi in}{a}} = c_n \cdot e^{x\frac{2\pi in}{a}} + \overline{c_n} \cdot e^{-x\frac{2\pi in}{a}}$$

then, the amplitude and phase are:

$$A(f(x)) = 2 \cdot |c_n| \qquad \rho(f(x)) = arg(c_n)$$

The set $\{e^{\frac{2\pi in}{a}}\}_{n\in\mathbb{Z}}$ are an orthonormal basis of the space of functions square integrables ($L^2([-\frac{a}{2}, \frac{a}{2}])$). That is, functions such that:

$$\int_{-\frac{a}{2}}^{\frac{a}{2}} |f(x)|^2 \, dx < \infty$$

If a becomes greater and greater, $(a \to \infty)$, it allows extending Fourier series to any non-periodic function of $L^2(\mathbb{R})$. The continuous *Fourier transform* of f is the function $\hat{f} : \mathbb{R} \to \mathbb{C}$:

$$\hat{f}(\omega) = \int_{-\infty}^{\infty} f(x) e^{-2\pi i\omega x} dx$$

for ω the continuous Fourier frequency.

By their condition of basis, we can recover the original function, $f(x)$ by means of the *inverse Fourier Transform*:

$$f(x) = \int_{-\infty}^{\infty} \widehat{f}(\omega) e^{2\pi i\omega x} d\omega$$

The Fourier transform in $\mathbb{R}^n$ is a straightforward extension of the one-dimensional Fourier transform [75]. In the particular 2-dimensional case (images), the *Fourier transform* is:

$$\hat{f}(\omega_1, \omega_2) = \int_{-\infty}^{\infty} \int_{-\infty}^{\infty} f(x_1, x_2) e^{-2\pi i(\omega_1 x_1 + \omega_2 x_2)} dx_1 dx_2$$

1.2.1 Properties

For any pair of real integrable functions, we have the following properties (see proposition 1.5.2 in section 1.5)

Linearity

The Fourier transformation of a linear combination of functions is a linear combination of their Fourier transforms:

$$\widehat{(\lambda f + \mu g)} = \lambda \widehat{f} + \mu \widehat{g}$$

It follows that one can treat each single signal composing a signal function separately and then to add their Fourier transforms.

Convolution

The convolution between two functions is defined by:

$$(f * g)(x) = \int_{-\infty}^{\infty} f(t)g(x-t)dt$$

The output of a convolution describes the local behavior of an image. It follows that this is a usual operation in many image processing tasks, such as, feature extraction, image filtering or texture detection, to mention just a few. The convolution of a signal with a filter simplifies in the Fourier domain to the product of their transforms.

$$\widehat{f * g} = \widehat{f} \cdot \widehat{g}$$

On one hand, in the case of filters of large support, this operation is faster than convolving in the spatial domain. On the other one, it constitutes a powerful tool to design image filters depending on the frequencies one wants to keep.

Figure 1.6 illustrates image filtering design in the Fourier domain and its effect in an IVUS frame. In this case, we apply a low-pass filtering only keeping low frequencies. The first row shows IVUS frames in cartesian coordinates, original image in fig.1.6(a) and the filtered one in fig.1.6(b). The second row shows the Fourier transforms of the image (fig.1.6(c)) and the low-pass filter (fig.1.6(d)). In fig.1.6(a) we show the original image, which is filtered in fig.1.6(b). The original image is transformed to the frequency domain and shown in fig.1.6(c). Fig.1.6(d) shows the Gaussian of mean $\mu = (0, 0)$ and width $\sigma = 10$:

$$g(\mu, \sigma) = \frac{1}{\sigma\sqrt{2\pi}} e^{-\frac{(x-\mu)^2}{2\sigma^2}}$$

The product of the Gaussian and the image of the Fourier transform is transformed back to the spatial domain to produce the filtered image in fig.1.6(b).

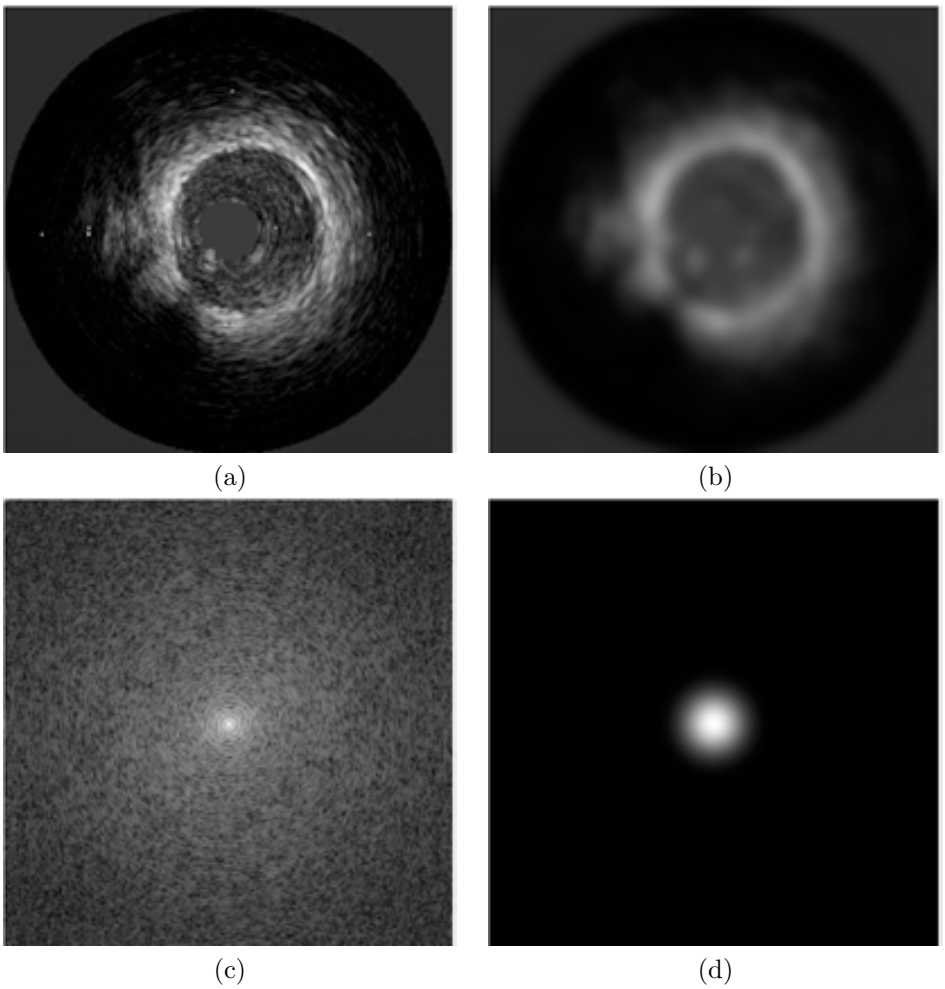

Figure 1.6: Image filtering in the Fourier domain. IVUS image filtered by a gaussian filter of $\sigma = 10$. Top plots are in the space domain: original image in fig.1.6(a) and filtered image in fig.1.6(b). Meanwhile, bottom plots are in the frequency domain: the Fourier Transform, FT, of the original image in fig.1.6(c) and a Gaussian of mean $\mu = (0, 0)$ and width $\sigma = 10$ in fig.1.6(d).

Translation

If two functions differ in a pure translation (t) in the spatial domain, then their Fourier transforms only differ in the phase (the amplitude remains unchanged). That is, the phase of the ratio between the corresponding Fourier transforms of the original functions results in a straight line which slope corresponds to the translation.

$$g(x) = (\tau_t f)(x) = f(x - t) \Rightarrow \widehat{g}(\omega) = \widehat{f}(\omega) e^{-2\pi i \omega t}$$

This property can be used to compute translation between images, which is the

basis of the estimation of the in-plane motion given in chapter 2.

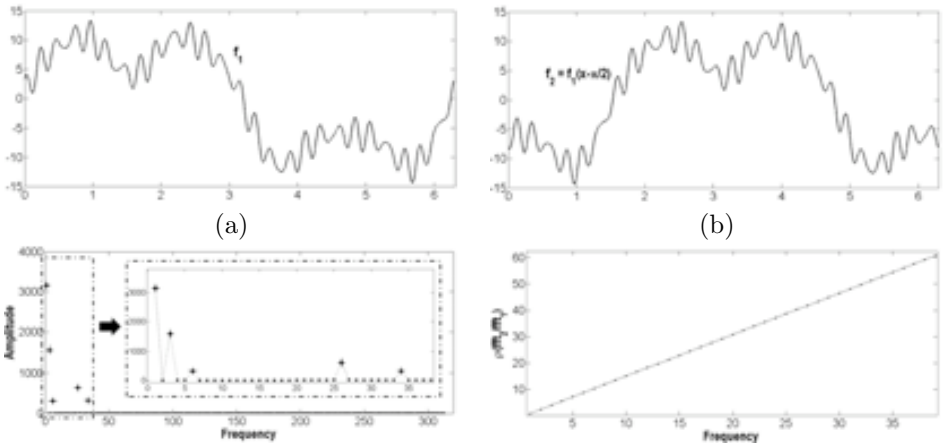

Figure 1.7: Shifted Functions. Original functions on the top row and their corresponding Fourier transforms on the bottom row.

Figure 1.7 illustrates this property. The top plots correspond to two functions in the spatial domain:

$$f_1 = 10sin(x) + 5sin(3x) + cos(6x) + 2cos(26x) + sin(34x)$$

and

$$f_2 = 10sin(x-\frac{\pi}{2}) + 5sin(3(x-\frac{\pi}{2})) + cos(6(x-\frac{\pi}{2})) + 2cos(26(x-\frac{\pi}{2})) + sin(34(x-\frac{\pi}{2}))$$

The second function (fig.1.7(b)), is a translation of $\frac{\pi}{2}$ of the first function (fig.1.7), $f_2(x) = f_1(x - \frac{\pi}{2})$. Plots on the second row correspond to the amplitude of Fourier transforms (fig.1.7(c)) and the phase of the ratio between both functions (fig.1.7(d)). Note that the slope of the phase is $\frac{\pi}{2}$, which corresponds to the shift between both functions in the spatial domain.

Scaling

The scaling of a function is related to its original function by an scaling in the frequency domain.

$$g(x) = f(\lambda x) \Rightarrow \widehat{g}(\omega) = \frac{1}{\|\lambda\|}\widehat{f}(\frac{\omega}{\lambda})$$

1.2.2 Particular Cases of Fourier Transforms

Periodic Functions

As explained at the beginning of the section, the Fourier transform of a periodic signal is a Fourier series. It follows that its spectrum identifies to the entire numbers, which

is a discrete set. On the other side, the Fourier transform of non-periodic signals has a continuous spectrum, that is, it identifies to the real line.

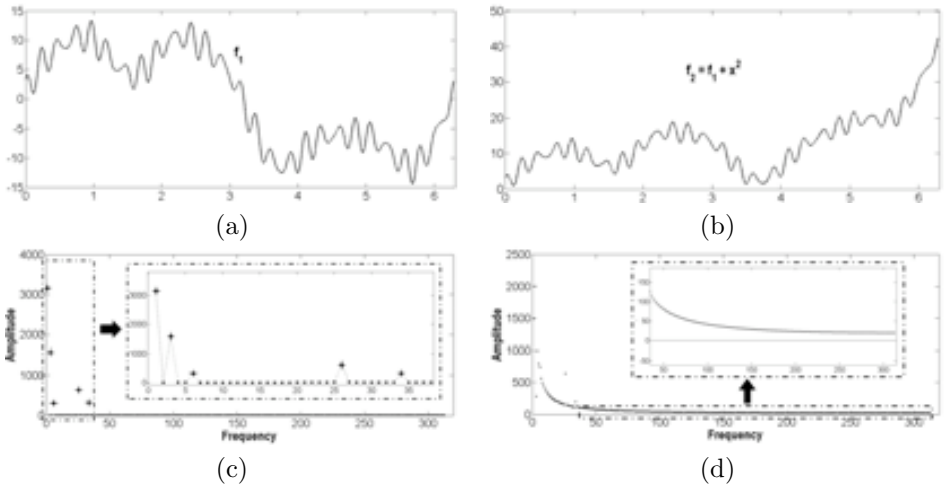

Figure 1.8: Fourier transforms of periodic and non-periodic functions. On the top row, the original functions, periodic (a) and non-periodic (b). On the bottom row, the corresponding Fourier transforms for the periodic function (c) and the non-periodic one (d).

The functions in figure 1.8 illustrate this phenomenon. Top plots show the periodic function,

$$f_1 = 10sin(x) + 5sin(3x) + cos(6x) + 2cos(26x) + sin(34x)$$

on the left (fig.1.8(a)) and the same function with a non-periodic term,

$$f_2 = x^2 + 10sin(x) + 5sin(3x) + cos(6x) + 2cos(26x) + sin(34x)$$

on the right (fig.1.8(b)). Bottom plots show the amplitudes (given by absolute values) of their Fourier transforms. Note that the five non-zero frequencies in the periodic function are reflected as 5 clear peaks in its Fourier transform. Meanwhile, the values of the Fourier transform of the non-periodic function cover the whole Fourier spectrum and present an exponential decay.

Smooth Functions

Regardless of its discrete nature, which is given by the function periodicity, Fourier spectra for functions infinitely differentiable ($\mathcal{C}^\infty$) might be of compact (closed and bounded subset) support or not. Compactness is independent of the discrete nature, since there exist non-compact discrete sets (e.g. the natural numbers) as well as compact non-discrete sets (e.g. the $[0, 1]$ interval). In the case of a differentiable function of compact support, its derivatives are integrable functions. This implies

(proposition 1.5.3) that the Fourier transform of the derivatives exists and satisfies:

$$\widehat{f^{(k)}}(\omega) = (2\pi i\omega)^k \hat{f}(\omega)$$

Since $\widehat{f^{(k)}}(\omega)$ is integrable, $\|\omega^k\|\|\hat{f}(\omega)\| < \varepsilon$ for large values of ω. It follows that $\|\hat{f}(\omega)\| < \frac{\varepsilon}{\|\omega^k\|}$ and, since ω^k is a polynomial, $\widehat{f} \in L^1$ has to be a function of rapid decay. In practical terms, this implies that high frequency coefficients are small enough to be neglected. That is, low-pass filters give a good approximation of this kind of functions.

1.3 Anisotropic Restricted Operators

By their faint and inhomogeneous appearance, in order to detect vessel layers (specially adventitia), IVUS images should be filtered first. In this section, we explain the mathematical formulation of a non-linear filtering operator able to preserve grey-level along transitions between vessel layers without altering their shape. At the same time, if the boundary conditions are changed, the differential operator is able to restore smooth contours consistent with vessel layers geometry.

Solutions to the heat diffusion equation with initial condition a given image, $I_0(x, y)$, provide a time (scale) dependant family, $I(x, y, t)$, of smoothed versions of $I_0(x, y)$. Heat diffusion is given in divergence form as:

$$I_t(x, y, t) = \operatorname{div}(J\nabla I), \quad I(x, y, 0) = I_0(x, y) \tag{1.6}$$

where $\nabla I = (I_x, I_y)$ is the image gradient, div is the divergence operator and J is a 2-dimensional symmetric (semi-) positive defined tensor that locally describes the way grey level re-distributes. It follows that J diagonalizes in an orthonormal basis (see section 1.1). Heat equation is thoroughly described by means of J eigenvectors (ξ, $\eta = \xi^{\perp}$) and eigenvalues (λ_1,λ_2), which describe the preferred diffusion directions of the heat. Symmetric semi-positive defined tensors define a metric in Euclidean space. The unitary vectors associated to the metric are an ellipse with axis of length λ_1, λ_2 oriented along ξ, $\xi^{\perp}$. The shape of such ellipse also describes the preferred diffusion of heat. In this sense, we can talk about isotropic diffusion (equal eigenvalues) and anisotropic diffusion (distinct and strictly positive eigenvalues). By general theory of partial differential equations [76], equation (1.6) has a unique solution provided that λ_1, λ_2 do not vanish. However, in such case, $I(x, y, t)$ converges to a constant image [53], so that the diffusion time (iterations in numeric implementations) is a critical issue for restoring an image preserving meaningful structures (termination problem [77]).

In [57], it is shown that, for null eigenvalues, existence and uniqueness of solutions to (1.6) is guaranteed as long as the eigenvector of positive eigenvalue defines a differentiable curve. In this case, J represents the projection matrix onto the positive eigenvector and diffusion restricts to its integral curves. Depending on the boundary conditions equation (1.6) models a smoothing process (Neumann conditions) or an extension one (Dirichlet).

1.3.1 Structure-Preserving Diffusion

The second moment matrix [78] or Structure Tensor [79] provides a good description of local image structures. The Structure Tensor tensor matrix, $ST_{\rho,\sigma}$ describes the gradient distribution in a local neighborhood of each pixel by averaging the projection matrices onto the image gradient:

$$ST_{\rho,\sigma} = g(\rho) * \left[\begin{pmatrix} I_x(\sigma) \\ I_y(\sigma) \end{pmatrix} (I_x(\sigma), I_y(\sigma)) \right] = \begin{pmatrix} g(\rho) * I_x^2(\sigma) & g(\rho) * I_x(\sigma) I_y(\sigma) \\ g(\rho) * I_x(\sigma) I_y(\sigma) & g(\rho) * I_y^2(\sigma) \end{pmatrix}$$

Image derivatives are computed using gaussian kernels, g_σ, of variance σ (differentiation scale):

$$I_x(\sigma) = g(\sigma)_x * I \text{ and } I_y(\sigma) = g(\sigma)_y * I$$

The projection matrix onto the image gradient, $\nabla I = (I_x(\sigma), I_y(\sigma))$ is averaged using a gaussian of variance ρ (integration scale). Since $ST(\rho, \sigma)$ is the solution to the heat equation with initial condition the projection matrix, its eigenvectors are differentiable (smooth) vector fields that represent image level sets normal (principal eigenvector, ξ) and tangent (secondary eigenvector, $\xi^\perp$) spaces. In the absence of corners (like anatomical contours in bottom right image in fig.1.9), the vector $\xi^\perp$ is oriented along image consistent contours (in the sense of regular differentiable curves [80]). At textured or noisy regions, $\xi^\perp$ is randomly distributed (upper right image in fig.1.9).

The Structure-Preserving Diffusion (SPD) is given by:

$$I_t = \text{div}(Q \Lambda Q^t \nabla I), \quad I(x, y, 0) = I_0(x, y) \tag{1.7}$$

with:

$$Q = \left(\xi^\perp, \xi\right) \text{ and } \Lambda = \begin{pmatrix} 1 & 0 \\ 0 & 0 \end{pmatrix}$$

for ξ the principal eigenvector of $ST(\rho, \sigma)$. By $\xi^\perp$ distribution (fig.1.9), SPD smoothes image grey values along regular structures (bottom right image in fig.1.9) and performs like a gaussian filter at textured and noisy regions (upper right image in fig.1.9). Its geometric nature makes the restricted diffusion evolution equation converge to a non trivial image that preserves the original image main features as curves of uniform gray level [57]. In this manner, SPD output achieves a uniform response to local image descriptors suitable for a further detection and segmentation of image (anatomical) regions.

Let us illustrate the benefits of SPD in medical imaging processing by applying it to cardiac Magnetic Resonance (MR) images of the left ventricle in short axis (SA) and long axis (LA) views. Fig.1.10 shows grey-level images and region segmentation for LA (top rows) and SA (bottom rows) views for, from left to right, non-processed, SPD, anisotropic filtering [53] and median filtering [81]. We have segmented three regions: blood (shown in white), myocardial walls (shown in grey) and background (shown in black). In original views (left columns) magnetic noise miss-classifies some pixels (identified as background) at myocardial regions. Miss-classifications still remain in anisotropic views (third column). SPD (second column) and median (forth column) filters solve this problem, but median views over-classify them, while myocardial walls

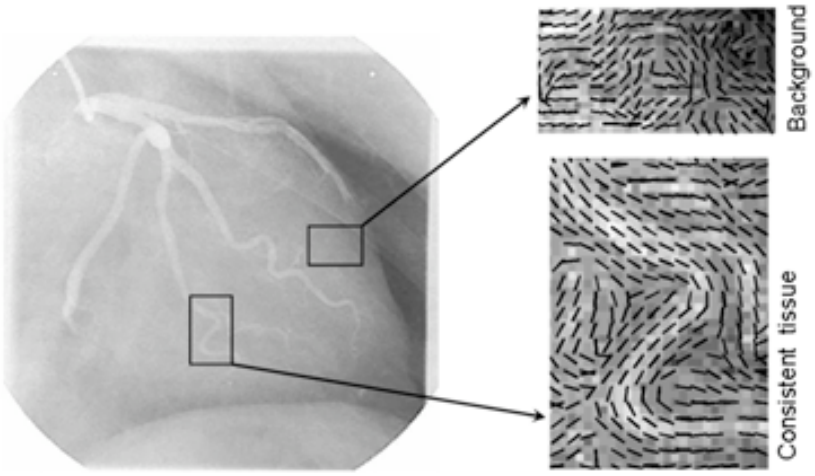

Figure 1.9: Vector field representing level curves of an angiography for a vessel (bottom-right image) and a background structure-less area (upper-right image).

maintain its shape on SPD views. Regarding blood, in original images of LA views we can notice a thin dark line corresponding to a valve, which is detected in SPD view, almost detected in anisotropic view and suspected in median view. We can notice the same effect in SA views for the thin dark line embedding the right ventricle (on the left side of the images) and the trabeculae on the left ventricle, which are over detected in anisotropic view and miss-detected in median view.

1.3.2 Anisotropic Contour Closing

If boundary conditions of equation (1.6) are changed to Dirichlet [76], the process governed by the equation results in a functional extension process. Such processes can be used to complete unconnected contours [58] as follows.

Let γ_0 be the set of points to connect, χ_{γ_0} its characteristic function (a mask) and $\tilde{J}$ the metric defined in equation (1.7). Then, the extension process, named Anisotropic Contour Closing (ACC):

$$I_t = \mathrm{div}(\tilde{J}\nabla I) \quad \text{with} \quad I_{|\gamma_0} = \chi_{\gamma_0} = \begin{cases} 1, & \text{if the pixel belongs to } \gamma_0; \\ 0, & \text{otherwise.} \end{cases} \tag{1.8}$$

converges to a closed model of γ. Intuitively, we are integrating the vector field ξ, that is, we are interpolating the unconnected curve segments along it. This fact endows ACC with two main advantages over other closing techniques, such as snakes [82]. First, the use of a restricted heat equation (1.8) ensures convergence to a closed model of the unconnected curve, whatever its concavity is. Second, because ξ takes into account image level sets geometry, ACC closures are more accurate than other interpolating techniques (such as geodesic snakes [82]) which, at most, yield piece-wise linear models.

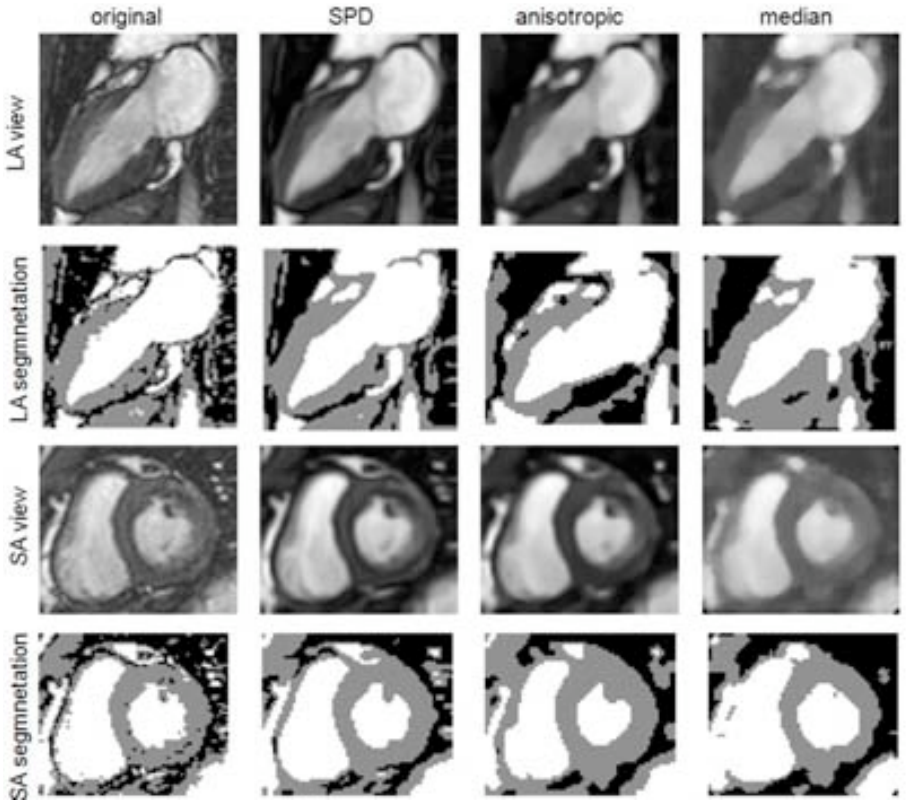

Figure 1.10: Performance of smoothing approaches on cardiac magnetic resonance images.

In order to avoid wrong continuations at noisy areas, the vector ξ is weighted by the coherence of the Structure Tensor. This quantity measures the vector regularity and is given by:

$$coh = \frac{(\lambda_1 - \lambda_2)^2}{(\lambda_1 + \lambda_2)^2}$$

for $\lambda_1 \geq \lambda_2$, $ST_{\rho,\sigma}$ eigenvalues. At regions where ξ is a continuous vector, λ_2 is close to zero, so coh is maximum, meanwhile, at noisy areas, since ξ is randomly oriented, λ_1 compares to λ_2 and $coh \sim 0$.

The vector guiding ACC is defined by:

$$\xi = coh\,\tilde{\xi} \tag{1.9}$$

for $\tilde{\xi}$ the minimum eigenvalue of the Structure Tensor $ST_{\rho,\sigma}$

Figure 1.11 illustrates the performance of ACC on an image of a human brain (fig.1.11(a)). Contours detected using a Canny edge detector are shown in fig.1.11(b). The unconnected contours which should be completed are better shown in the zoom of fig.1.11(c). The mask shown in fig.1.11(d) corresponds to the characteristic function

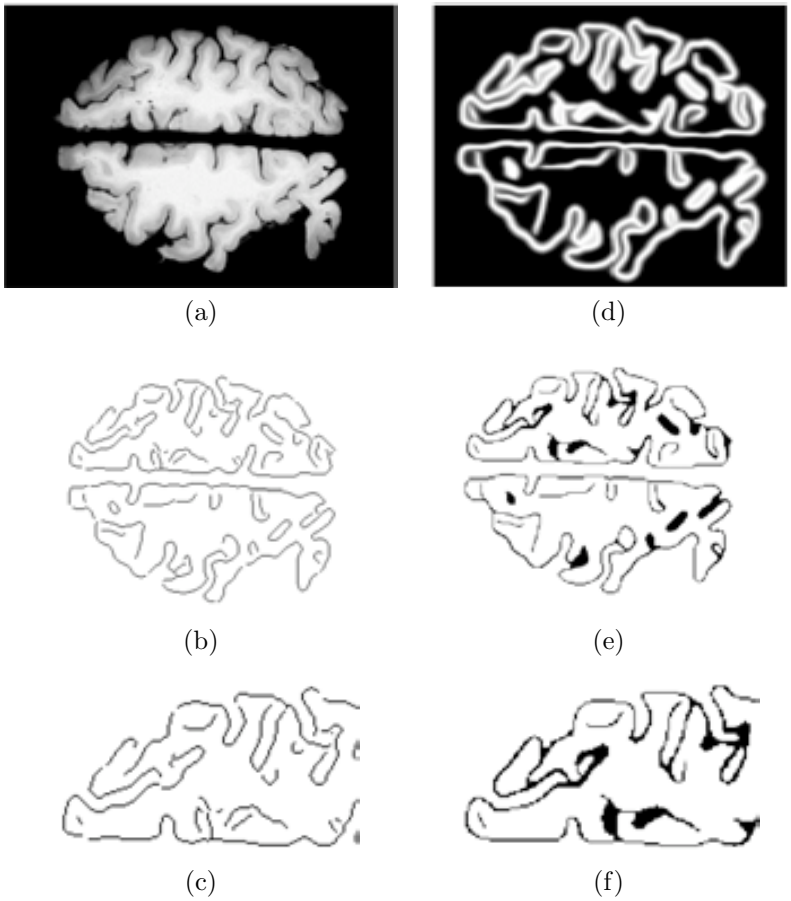

Figure 1.11: Anisotropic Contour Closing

obtained from the extension process (equation (1.8)). Finally, in fig.1.11(e) we show the image ridges of mask yielding the ACC closure. The close-up of figure 1.11(f) shows the completeness of contours and their agreement to the original geometry of the brain folds.

1.4 B-snakes

The amount of images involved in an IVUS sequence suggests searching for a contour representation as compact as possible. This motivates guiding a parametric B-snake towards ACC closure to obtain a compact smooth explicit representation.

A parametric snake is a curve $\gamma(u) = (x(u), y(u))$ which, under the influence of an external force, E_{ext}, and internal constrains, E_{int}, models a target curve γ_τ by

minimizing the energy functional:

$$\begin{aligned} E(\gamma) &= \int_\gamma (E_{int}(\gamma) + E_{ext}(\gamma, \gamma_\tau))du \\ &= \int_\gamma (\frac{1}{2}\alpha\|\dot{\gamma}\|^2 + \frac{1}{2}\beta\|\ddot{\gamma}\|^2 + E_{ext}(\gamma, \gamma_\tau))du \\ &= \int F(\gamma, \dot{\gamma}, \ddot{\gamma})du \end{aligned} \tag{1.10}$$

The external energy, E_{ext}, is an external potential achieving a minimum on γ_τ, which faithfully preserves the target curve. The internal energy, E_{int}, preserves the continuity and smoothness of γ, weighted by $\alpha, \beta \in [0, 1]$.

The minimum of (1.10) is found by canceling the first derivative of E given by the Euler-Lagrange equation [76]:

$$F_\gamma - d_u(F_{\dot{\gamma}}) + d_{uu}(F_{\ddot{\gamma}}) = 0$$

where d_u and d_{uu} correspond to the first and second derivatives, respectively, of the function F. This equation leads to solving the following system of 2 equations:

$$\begin{cases} -\alpha x_{uu} + \beta x_{uuuu} + \frac{\partial E_{ext}}{\partial x} = 0 \\ -\alpha y_{uu} + \beta y_{uuuu} + \frac{\partial E_{ext}}{\partial y} = 0 \end{cases}$$

In the discrete case the curve γ is defined by a sampling of n points $(x_1, \ldots, x_n, y_1, \ldots, y_n)$ so that the energy functional (1.10) converts to:

$$E = \sum_{i=1}^{n} E_{int}(i) + \sum_{i=1}^{n} E_{ext}(i)$$

The corresponding Euler-Lagrange equations are a system of $2n$ equations which can be written in matrix form:

$$\begin{cases} Ax = -\frac{\partial E_{ext}}{\partial x} \\ Ay = -\frac{\partial E_{ext}}{\partial y} \end{cases} \tag{1.11}$$

where A is a penta-diagonal matrix called the stiffness matrix and expressed by:

$$\begin{pmatrix} 2\alpha+6\beta & -\alpha-4\beta & \beta & 0 & 0 & 0 & \ldots & \beta & -\alpha-4\beta \\ -\alpha-4\beta & 2\alpha+6\beta & -\alpha-4\beta & \beta & 0 & 0 & \ldots & 0 & \beta \\ \beta & -\alpha-4\beta & 2\alpha+6\beta & -\alpha-4\beta & \beta & 0 & 0 & \ldots & 0 \\ 0 & \beta & -\alpha-4\beta & 2\alpha+6\beta & -\alpha-4\beta & \beta & 0 & \ldots & 0 \\ \vdots & \vdots & \vdots & \vdots & \vdots & \vdots & \vdots & \vdots & \vdots \\ -\alpha-4\beta & \beta & 0 & 0 & \ldots & 0 & \beta & -\alpha-4\beta & 2\alpha+6\beta \end{pmatrix}$$

The system (1.11) is solved iteratively by writing it as:

$$\begin{cases} (A + \delta I)x = \delta x - \frac{\partial E_{ext}}{\partial x} \\ (A + \delta I)y = \delta y - \frac{\partial E_{ext}}{\partial y} \end{cases}$$

for any scalar δ. Thus we have:

$$\begin{cases} x = (A + \delta I)^{-1}(\delta x - \frac{\partial E_{ext}}{\partial x}) \\ y = (A + \delta I)^{-1}(\delta y - \frac{\partial E_{ext}}{\partial y}) \end{cases}$$

So that, the iterative scheme is given by:

$$\begin{cases} x_{t+1} = (A + \delta I)^{-1}(\delta x_t - \frac{\partial E_{ext}}{\partial x}) \\ y_{t+1} = (A + \delta I)^{-1}(\delta y_t - \frac{\partial E_{ext}}{\partial y}) \end{cases}$$

1.5 Proofs

This section is devoted to mathematically prove some assumptions about polar coordinates transforms and Fourier development made along the chapter.

Proposition 1.5.1 *The points*

$$\begin{pmatrix} \tilde{x} \\ \tilde{y} \end{pmatrix} = \begin{pmatrix} \cos\theta & -\sin\theta \\ \sin\theta & \cos\theta \end{pmatrix} \cdot \begin{pmatrix} \lambda_1 & 0 \\ 0 & \lambda_2 \end{pmatrix} \cdot \begin{pmatrix} x \\ y \end{pmatrix}$$

of a body undergoing a rotation of angle θ followed by a dilation of factor $\lambda = (\lambda_1, \lambda_2)$ in Cartesian coordinates, in polar coordinates corresponds to:

$$\begin{cases} \tilde{r} = \sqrt{(\lambda_1 x)^2 + (\lambda_2 y)^2} \\ \tilde{\alpha} = atan\left(\frac{\lambda_2 y}{\lambda_1 x}\right) + \theta \end{cases} \tag{1.12}$$

Proof By applying (1.12) to equations of (x', y') we obtain the following:

$$\begin{aligned} r^2 = x'^2 + y'^2 &= (\lambda_x x cos\theta - \lambda_y y sin\theta)^2 + (\lambda_x x sin\theta + \lambda_y y cos\theta)^2 \\ &= (\lambda_x x)^2 + (\lambda_y y)^2 \end{aligned}$$

So, $r = \sqrt{(\lambda_x x)^2 + (\lambda_y y)^2}$

The same steps for the angle:

$$\begin{aligned} tan(\alpha) = \frac{sin(\alpha)}{cos(\alpha)} &= \frac{\tilde{y}}{\tilde{x}} \\ \frac{sin(\alpha)}{cos(\alpha)} &= \frac{\lambda_x x sin(\theta) + \lambda_y y cos(\theta)}{\lambda_x x cos(\theta) - \lambda_y y sin(\theta)} \\ sin(\alpha) \cdot (\lambda_x x cos(\theta) - \lambda_y y sin(\theta)) &= cos(\alpha) \cdot (\lambda_x x sin(\theta) + \lambda_y y cos(\theta)) \\ \lambda_x x \cdot (sin(\alpha)cos(\theta) - cos(\alpha)sin(\theta)) &= \lambda_y y \cdot (sin(\alpha)sin(\theta) + cos(\alpha)cos(\theta)) \\ \lambda_x x \cdot sin(\alpha - \theta) &= \lambda_y y(cos(\alpha - \theta)) \\ tan(\alpha - \theta) &= \frac{\lambda_y y}{\lambda_x x} \end{aligned}$$

So, $\alpha = atan\left(\frac{\lambda_y y}{\lambda_x x}\right) + \theta$ □

Proposition 1.5.2 *Let $f, g \in L^1(\mathbb{R})$ be two functions. Then, they satisfy the following properties:*

1. *Linearity.* $(\widehat{\lambda f + \mu g}) = \lambda \widehat{f} + \mu \widehat{g}$
2. *Convolution.* $\widehat{f * g} = \widehat{f} \cdot \widehat{g}$
3. *Translation.* $g(x) = (\tau_z f)(x) = f(x - z) \Rightarrow \widehat{g}(\omega) = \widehat{f}(\omega) e^{-2\pi i \omega z}$
4. *Scaling.* $g(x) = f(\lambda x) \Rightarrow \widehat{g}(\omega) = \frac{1}{\|\lambda\|} \widehat{f}(\frac{\omega}{\lambda})$

Proof 1. $(\widehat{\lambda f + \mu g}) = \lambda \hat{f} + \mu \hat{g}$

$$\begin{aligned}
(\widehat{\lambda f + \mu g})(\omega) &= \int_{-\infty}^{\infty} (\lambda f(x) + \mu g(x)) e^{-2\pi i \omega x} dx \\
&= \lambda \int_{-\infty}^{\infty} f(x) e^{-2\pi i \omega x} dx + \mu \int_{-\infty}^{\infty} g(x) e^{-2\pi i \omega x} dx \\
&= \lambda \hat{f} + \mu \hat{g}
\end{aligned}$$

2. $\widehat{f * g} = \widehat{f} \cdot \widehat{g}$

$$\begin{aligned}
\widehat{f * g}(x) &= \int_{-\infty}^{\infty} (f * g)(x) e^{-2\pi i \omega x} dx \\
&= \int_{-\infty}^{\infty} \int_{-\infty}^{\infty} f(t) g(x - t) dt e^{-2\pi i \omega x} dx \\
&= \int_{-\infty}^{\infty} \int_{-\infty}^{\infty} f(t) g(x - t) e^{-2\pi i \omega x + 2\pi i \omega t - 2\pi i \omega t} dx dt \\
&= \int_{-\infty}^{\infty} \int_{-\infty}^{\infty} f(t) g(x - t) e^{-2\pi i \omega (x - t)} e^{-2\pi i \omega t} dx dt \\
&= \int_{-\infty}^{\infty} f(t) e^{-2\pi i \omega t} dt \int_{-\infty}^{\infty} g(y) e^{-2\pi i \omega (y)} dy \\
&= \widehat{f} \cdot \widehat{g}
\end{aligned}$$

3. If $g(x) = (\tau_z f)(x) = f(x - z)$, then $\hat{g}(\omega) = \hat{f}(\omega) e^{-2\pi i \omega z}$

$$\begin{aligned}
\hat{g}(\omega) &= \int_{-\infty}^{\infty} g(x) e^{-2\pi i \omega x} dx = \int_{-\infty}^{\infty} f(x - z) e^{-2\pi i \omega x} dx \\
&= \int_{-\infty}^{\infty} f(x - z) e^{-2\pi i \omega z} e^{-2\pi i \omega (x - z)} dx = e^{-2\pi i \omega z} \int_{-\infty}^{\infty} f(x - z) e^{-2\pi i \omega (x - z)} dx \\
&= e^{-2\pi i \omega z} \hat{f}(\omega)
\end{aligned}$$

4. If $g(x) = f(\lambda x)$, then $\hat{g}(\omega) = \frac{1}{\|\lambda\|}\hat{f}(\frac{\omega}{\lambda})$

$$\hat{g}(\omega) = \int_{-\infty}^{\infty} g(x)e^{-2\pi i\omega x}dx = \int_{-\infty}^{\infty} f(\lambda x)e^{-2\pi i\omega x}dx = \int_{-\infty}^{\infty} \frac{1}{\lambda}f(y)e^{-2\pi i\frac{\omega}{\lambda}y}dy$$
$$= \frac{1}{\|\lambda\|}\int_{-\infty}^{\infty} f(y)e^{-2\pi i\frac{\omega}{\lambda}y}dy = \frac{1}{\|\lambda\|}\hat{f}\left(\frac{\omega}{\lambda}\right)$$

□

Proposition 1.5.3 *If $f, f', f'', \cdots, f^{(k)} \in L^1(\mathbb{R})$ then, $\widehat{f^{(k)}}(\omega) = (2\pi i\omega)^k\hat{f}(\omega)$*

Proof Integrating by parts we have:

$$\widehat{f'}(\omega) = \int_{-\infty}^{\infty} f'(x)e^{-2\pi i\omega x}dx = \left[f(x)e^{-2\pi i\omega x}\right]_{x\to-\infty}^{x\to\infty} + 2\pi i\omega\int_{-\infty}^{\infty} f(x)e^{-2\pi i\omega x}dx$$

By Cauchy theorem [80]and since f is integrable, the first term vanishes. By induction we obtain $\widehat{f^{(k)}}(\omega) = (2\pi i\omega)^k\hat{f}(\omega)$

□

Chapter 2

Physics-based Models for Vessel Dynamics Exploring

Tissue bio-mechanical properties (like strain and stress) are playing an increasing role in diagnosis and long-term treatment of intravascular coronary diseases. Their assessment strongly relies on estimation of vessel wall deformation. Since IntraVascular UltraSound (IVUS) sequences allow visualizing vessel morphology and reflect its dynamics, this technique represents a useful tool for evaluation of tissue mechanical properties.

Image misalignment introduced by vessel-catheter motion is a major artifact for a proper tracking of tissue deformation. In the first section of this chapter, we assess IVUS rigid in-plane motion due to heart beating. Motion parameters are computed by considering both the vessel geometry and its appearance in the image. In the case of IVUS sequences, due to its acquisition nature, different dynamic components are reflected in these transformations, not only cardiac component. On one hand, breathing forces a periodic displacement of arteries. On the other one, vessel geometry (curvature and torsion) influences on the relative position between catheter and artery. We decompose dynamics into geometric and motion components and identify the role of each term.

On the other side, longitudinal motion artifacts in IVUS sequences hinders a properly 3D reconstruction and vessel measurements. Most of current techniques base on the ECG signal to obtain a gated pullback without the longitudinal artifact by using a specific hardware or the ECG signal itself. The potential of IVUS images processing for phase retrieval still remains little explored. In section 2.2, we present an image-based approach for cardiac phase retrieval from coronary IVUS sequences without ECG signal. Inspired on the fact that maximum and minimum lumen areas are related to end-systole and end-diastole, our cardiac phase retrieval is based on the evolution of physical quantities along the sequence and statistically explores which is the best filter for extracting it.

Finally, the mathematical issues supporting some assumptions made along the chapter are detailed in section 2.3.

2.1 In-plane Dynamics

Different factors such as heart pumping, blood pressure or artery geometric properties mainly contribute to the dynamics of coronary arteries [71, 21, 72]. The first order approximation to vessel in-plane dynamics is given by a linear transformation combining translation, rotation and scaling [73]. Dilation is inherent to the elasticity of the vessel itself and it does not preserve the metric. The rigid part of this approximation can be modeled as a rigid body motion and is given by a rotation followed by a translation.

In body dynamics, the point describing the object response to external forces and torques is determined by means of its center of gravity or mass [83]. The difference between its position and the origin of coordinates is identified to the object translation. In this framework, the object motion is given by a rotation centered at its center of mass, which position is identified to the object translation. If the center of mass of the object at time zero is taken as origin, then the linear application mapping the object at a given time to the object at time zero (section 1.1 of chapter 1) is given by:

$$\begin{pmatrix} \tilde{x} \\ \tilde{y} \end{pmatrix} = \begin{pmatrix} \cos\theta & -\sin\theta \\ \sin\theta & \cos\theta \end{pmatrix} \cdot \begin{pmatrix} x - t_1 \\ y - t_2 \end{pmatrix} \tag{2.1}$$

for $\vec{t} = (t_1, t_2)$ the position of the center of mass and θ the angle of rotation in radians. Rigid motion parameters are computed by combining vessel geometry and appearance as follows.

2.1.1 Translation

Since IVUS sequences are centered at the catheter (which coincides with the center of the image), vessel translation is given by position of the center of gravity of the vessel, namely VCM, at each frame.

Since grey level reflects tissue mass density due to IVUS images reconstruction, the center of mass given by the image intensity, namely ICM, corresponds to the physical center of gravity of the vessel. However, some acquisition devices allow interactive tuning of the image brightness in order to enhance tissue and vessel structures appearance [84]. Such intensity gain is radial [85], and the image is made-up from this tuning. Thus, tissue close to the catheter might look brighter and, for vessels not centered at the catheter, intensity gainings might deviate the position of ICM from the true center of mass. Vessel geometric center, namely GCM, coincides with the vessel center of gravity only in the case of uniform tissue density. However, it serves to compensate the deviation of ICM for non centered vessels. We define the center of mass of the vessel, VCM, by a combination of ICM and GCM achieving a good compromise between vessels whose intensity gain has been tuned and vessels with uniform tissue density.

Image Center of Mass - ICM

Let I be an image of dimensions $n \times m$ and (i, j) be the pixel position in the image. The center of mass of the image (ICM) is given by averaging image pixel positions

weighted by their grey-value intensity:

$$ICM = \left(\frac{\sum_{i=1}^{n} i \sum_{j=1}^{m} I(i,j)}{\sum_{i=1}^{n} \sum_{j=1}^{m} I(i,j)}, \frac{\sum_{j=1}^{m} j \sum_{i=1}^{n} I(i,j)}{\sum_{i=1}^{n} \sum_{j=1}^{m} I(i,j)} \right)$$

Geometric Center of Mass - GCM

The geometric center (GCM) of a set of N image points, $(x_k, y_k)_{1 \leq k \leq N}$, is computed as the average of their positions:

$$GCM = \frac{1}{N} \left(\sum_{k=1}^{N} x_k, \sum_{k=1}^{N} y_k \right)$$

In the case of IVUS sequences, the most reliable geometric center of the vessel is the center of the transition between media and adventitia layers, since it is the vessel structure which best preserves its shape, regardless of morphological changes. Thus, the points chosen to compute the geometric center are a set roughly lying on this transition (which is named adventitia for convenience). The strategy to extract these points is an iterative algorithm based on a temporal analysis along the sequence [56].

1. **Lumen Displacement Reduction.** In polar coordinates with the origin at the center of the image, the vessel appears as a straight band as far as it is centered at the catheter. Any deviation between the vessel and the catheter results in a undulate profile. The lumen displacement along the sequence converts into a dynamic radial wave. Such wave is suppressed by transforming images to polar coordinates with origin fixed at ICM. We name $Ipol$ such polar images.

2. **Negative Edge extraction.** The points roughly lying on the adventitia are extracted by means of negative horizontal edges, e_y, of the polar images, $Ipol$. Edges are computed by convolving $Ipol$ with the y-partial derivative of a 2 dimensional gaussian kernel of variance ρ:

$$e_y(i,j) = g_y(i,j) * Ipol(i,j)$$

$$\text{for} \quad g_y(i,j) = -\frac{j}{2\pi\rho^4} e^{-(i^2+j^2)/(2*\rho^2)}$$

3. **Geometric Displacement Reduction:** The impact of noise and artifacts is minimized by considering the average of e_y for a block of N sequence frames. Vessel curvature displacement produces a blurring of the energy average at curved angular sectors. The number of frames achieving the best compromise between small artifacts removing and tissue blurring is approximately a third of the heart cycle (10 frames in pull-backs at 30 frames per second). We select for each angle (column) those points with the former average below the 5% radial percentile. Spurious edges due to noise and other sparse artifacts (such as blood scatter at branches) are removed by applying a length filtering to the extracted edges that leaves only those connected components of a length above a given

value. In order to endow further continuity to the selected segments, we use the statistical distribution of their radial position along a block of images.

Percentiles computed in the sequence block of 100 frames serve to discard outliers by only considering points within the central percentile range. In order to capture the adventitia curvature, percentiles are computed on angular sectors of 5 degrees. The final radial values serve to compute the new origin of our polar transform.

The more straight the adventitia is, the more reliable the points selected are. At the same time, the more reliable the geometric center is, the more straight the adventitia is. Thus, steps 2 and 3 are repeated until convergence of the central percentile. Finally, the set $(x_k, y_k)_k$ is obtained by transforming the radial and angular coordinates of the above points in the polar image back to the cartesian domain.

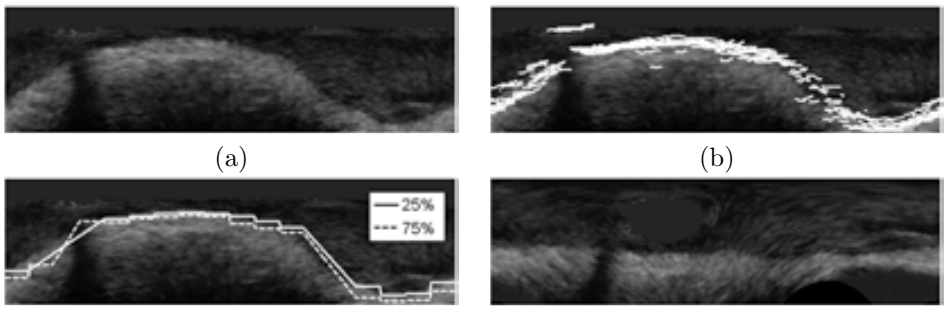

Figure 2.1: Adventitia Straighten Procedure: polar image with origin at the image mass center (a), edges in a sequence block (b), central percentile of edges positions (c) and final polar image (d).

Figure 2.1 illustrates the main steps of the geometric eccentricity suppression. Fig. 2.1(a) shows the polar transform with the origin at ICM. In fig.2.1(b) we show the selected edges in a sequence block. Fig.2.1(c) shows the plot for their central percentile. Steps shown in fig.2.1(b) and fig.2.1(c) are repeated until 25% and 75% percentiles are close enough. The straighten adventitia image is shown in fig.2.1(d). Figure 2.2 shows the points roughly lying on the adventitia layer used to compute GCM for three representative cases: a centered vessel with hardly soft plaque (fig.2.2(a)), a large vessel deviated from its center with calcium plaque (fig.2.2(b)) and a vessel deviated with fibrotic plaque (fig.2.2(c)). Although the points detected on the adventitia are not optimal, they suffice to compute its center.

Vessel Center of Mass - VCM

In those cases that the vessel wall is not centered at the catheter, the geometric center of mass serves to correct the image center of mass. Let us consider the maximum, R_{max}, and minimum, R_{min}, distances of the set $(x_k, y_k)_k$ to the image center:

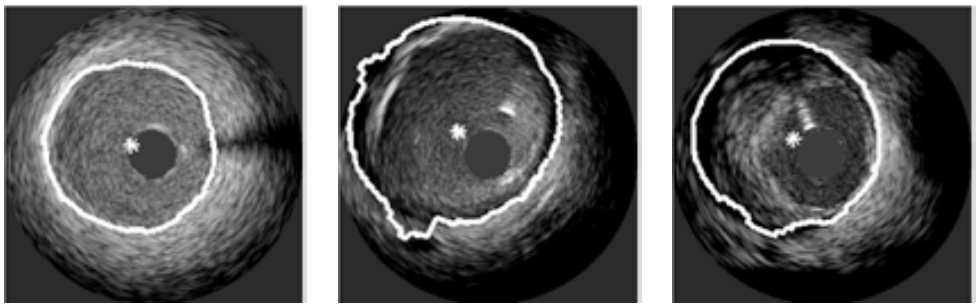

(a) (b) (c)

Figure 2.2: Detection of points roughly lying on the adventitia for different morphologies with the corresponding geometric center. A centered vessel with hardly soft plaque (a), a vessel not centered at the catheter with fibrotic plaque (b) and a large vessel not centered at the catheter with calcium plaque (c).

$$R_{max} = \max_k \left(\sqrt{x_k^2 + y_k^2} \right) \quad R_{min} = \min_k \left(\sqrt{x_k^2 + y_k^2} \right)$$

and, denoted by DR, the vessel-catheter deviation rate given by:

$$DR = \frac{R_{min}}{R_{max}}$$

Then, the vessel center of mass, VCM, is defined as:

$$VCM = DR \cdot ICM + (1 - DR) \cdot GCM \tag{2.2}$$

Figure 2.3 shows the three different centers of mass for a vessel not centered at the imaging catheter. In fig.2.3(a), ICM appears nearly centered in the image, but not centered in the vessel. In fig.2.3(b), GCM is centered in the vessel, so it corrects ICM to the final VCM in fig.2.3(c).

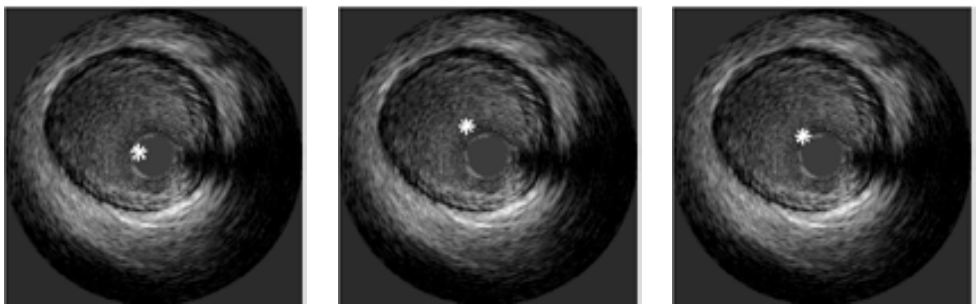

(a) (b) (c)

Figure 2.3: Center of gravity computations: ICM (a), GCM (b) and VCM (c).

2.1.2 Rotation

Once vessel translation has been compensated, two global motions still remain: rotation and radial scaling. According to (subsection 1.1.1), in the polar domain with origin VCM, they convert into a horizontal translation (corresponding to rotation) and a vertical scaling, (corresponding to radial scaling). Let I_1, I_2 be two consecutive polar frames (with origin at VCM) of the sequence and let us assume an isometric dilation. By proposition 1.5.1 they are related via:

$$I_2(i,j) = I_1(i+\theta, \lambda j)$$

where θ corresponds to the angle of rotation and λ to the dilation.

In the case of human coronary arteries, scaling is very close to 1 [86], so $\lambda = 1+\varepsilon$ becomes a perturbation of identity given by ε. Furthermore, we restrict computations to a band around the media-adventitia layer, given by $j = j_0 + \Delta j$. By Taylor's formula [80], it follows that the first order approximation to I_2 is given by:

$$\begin{aligned} I_2(i,j) &= I_1(i+\theta, j+\varepsilon j) \sim I_1(i+\theta, j) + \varepsilon j \partial_j I_1(i+\theta, j) \\ &= I_1(i+\theta, \Delta j + j_0) + \varepsilon j \partial_j I_1(i+\theta, j) \end{aligned}$$

for ∂_j denoting the partial derivative with respect to the second variable.

Since t and j_0 are constant shifts, the first order approximation to I_2 can be computed by applying the Fourier transform [87] and using phase correlation [88]. Let $\widehat{I_1}$, $\widehat{I_2}$ be the Fourier transforms of I_1, I_2 and let us assume that they differ in a pure translation:

$$I_2(i,j) = I_1(i-t_1, j-t_2) \;\; [= I_1(i+\theta, \Delta j + j_0)]$$

then their Fourier transforms are related (proposition 1.5.2) via:

$$\widehat{I_2}(\omega) = \widehat{I_1}(\omega) e^{-i\langle \omega, t\rangle}$$

for $\omega = (\omega_1, \omega_2)$ the Fourier frequency, $\vec{t} = (t_1, t_2)$ and $\langle \omega, \vec{t} \rangle = \omega_1 t_1 + \omega_2 t_2$ the Euclidean scalar product.

If we consider the phase, $\rho(\omega)$, of the ratio between the two Fourier transforms [89], we have that:

$$\rho(\omega) = \rho\left(\frac{\widehat{I_2}(\omega)}{\widehat{I_1}(\omega)}\right) = \rho\left(e^{-i\langle \omega, t\rangle}\right) = \langle \omega, t\rangle \;\; = \omega_1 t_1 + \omega_2 t_2$$

so that the points $(\omega_1, \omega_2, \rho(\omega))$ lie on a plane, Π, with the slopes given by the translation:

$$\Pi : \rho(\omega) = t_1\omega_1 + t_2\omega_2$$

In practice, noise and texture introduce a scatter in the set $(\omega_1, \omega_2, \rho(\omega))$, especially for those frequencies with smaller amplitudes. We reduce noise-scatter by only considering those frequencies common to both images with an associated amplitude larger than a given percentile. Such frequencies with the phase ρ yield a point

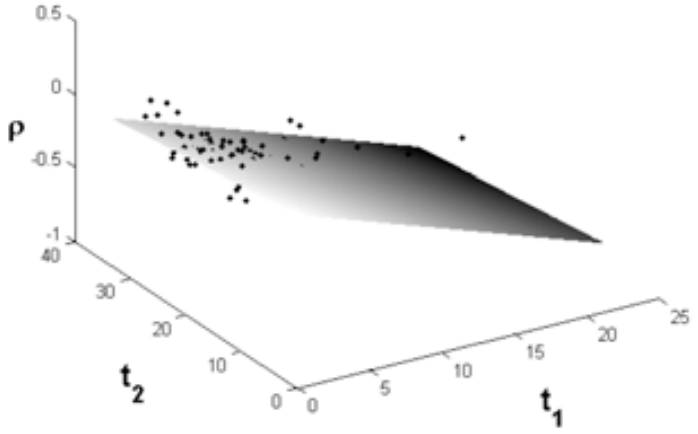

Figure 2.4: Regression plane approximating Fourier phase correlation between two shifted images.

cloud, like the one shown in figure 2.4, which regression plane provides a least-square estimator of the plane Π.

The first slope of the regression plane estimates the angle of rotation between two consecutive frames. Since polar coordinates cover 360 degrees, rotation angles are given in the range $[-\pi, \pi] \equiv [-180^{\text{o}}, 180^{\text{o}}]$. This range covers all possible rotational motions because a rotation angle is determined modulus $2k\pi$ radians due to such a rotation does not affect the appearance of the image/structure undergoing it. The rotation of each image at time k with respect to a reference frame at time 1 is computed by accumulating all frame-to-frame rotation angles. That is, let $\theta^{k-1,k}$ be the rotation angle between two consecutive frames at times $k-1$ and k, then the rotation angle aligning the k-th frame to a first one is given by:

$$\theta^{k} := \sum_{j=1}^{j=k} \theta^{j-1,j} \tag{2.3}$$

The reliability of the rotation angle is related to the regression plane fitting error (residuals). Large residuals indicate a poor linear dependency between frequency and phase. In this cases, the estimated parameter does not properly approach the rotation angle and should be discarded. Since polar images are 360 pixels wide, anomalous cases are detected by a mean fitting error over 1 (degree/pixel). Such angles constitute less than 6.43% of the data analyzed and their values are interpolated along the sequence using the preserved angles.

For a detailed explanation of the mathematical argumentations supporting the assumptions made in our estimation of the rotation angle, the reader can have a look at section 2.3.

2.1.3 Dynamics Decomposition

The rigid motion that cardiac vessels undergo is a complex dynamical process which results from the combination of several contributions. In general, it presents a geometric component related to the artery 3D shape and a dynamic one induced by breathing and cardiac movements [7]. Depending on the particular problem to approach, each of the terms should have specific treatment. Exploring artery geometry might be derived by analyzing the geometric component [90], whereas extraction of cardiac dynamics concerns the cardiac dynamical contribution [16]. In the case of vessel biomechanics analysis, the goal is to produce a static model allowing a better tissue tracking along the segment. Firstly, the reader should note that, without further analysis, the geometric component does not reach a reliable 3D representation of the vessel geometry, which might lead to wrong static models. Secondly, even if one could infer the true 3D geometry from it, by compensating vessel tortuosity there is no guarantee of a better alignment of vessel plaque. This suggests only correcting the dynamical terms of the translation and rotation for stabilizing the sequence. In order to allow a complete comprehension of vessel dynamics, this subsection is devoted to provide the mathematical tools for decoupling each of the terms.

The translation and rotation parameters are functions of the time s. If the geometric term of a motion parameter is denoted by the subindex $_g$, the cardiac term, induced by heart beating, is denoted by the subindex $_c$ and breathing contributions are denoted by the subindex $_b$, the angle and translation decompose into:

$$\begin{aligned} t(s) &= t_g(s) + t_b(s) + t_c(s) \\ \theta(s) &= \theta_g(s) + \theta_b(s) + \theta_c(s) \end{aligned} \tag{2.4}$$

Focusing on the Fourier series of these components, breathing and cardiac terms are periodic and, thus, have a discrete Fourier spectrum, whereas geometry has a broad-band (non-discrete) spectrum [87]. As usual, Fourier transforms are indicated by a hat ($\hat{}$) over functions. Principal harmonics have been learned by supervised classification of the spectrum of a training set of 30 patients without apparent lesions used in a study for assessment of myocardial perfusion in contrast angiography [91]. Confidence intervals of the 95% yield the expected ranges for the principal frequency of each of the periodic components. For breathing it is $(10, 45)$ repetitions per minute (rpm), while for cardiac motion it is $(45, 200)$ rpm. Each term in (2.4) is approached as follows.

Geometric Component

Since the artery length is finite, the geometric component is a function of compact support and, thus, the derivatives of the geometric component are integrable functions. By proposition 1.5.3, $\hat{f_g}$ is a function of rapid decay, so that, high frequency coefficients are small enough to be neglected [86].

The geometric term is approximated with the low-frequency spectrum of the signal (low-pass filter [92]). Although part of the geometric component is categorized into the cardiac and breathing components, the range 1-10 rpm has (experimentally) proved to be a good approximation. Thus, the geometric term is enclosed by frequencies between 1 and 10 rpm.

Breathing Component

The study reported in [91] indicates that, in spite of being periodic, breathing can be defined by the whole spectrum in the interval (10,45) rpm. The ranges reported in [91] were obtained from a study on patients without apparent lesions performed in our laboratory for assessment of myocardial perfusion in contrast angiography [91]. The frequency range was learned by supervised classification of the spectrum of a training set of 30 patients. For each patient three different sequences were recorded:

- A sequence without contrast injection and the patient normally breathing in order to learn diaphragm movements and background noise
- A sequence with contrast injection and the patient holding breathing for learning the frequency range of heart beating and myocardial staining.
- A test sequence with contrast injection and the patient normally breathing.

The values of the local mean for all sequence frames provides each pixel with a function, namely LM, that describes the average contrast absorbed by the tissue along time. Such signal is the contribution of four main phenomena: breathing, heart beating, myocardial dyeing and noise. The amplitudes of the spectrum of the LM patterns define a probability density function (pdf) in the frequency domain, which we modeled with a mixture of Gaussians [93]. The Bayes classifier for the four classes gave the frequency ranges for the physiological phenomena reported in the article. We note that ranges coincide with clinical evidence: a living human does not breath more than 45 times per minute and its heart does not beat more than 200 times per minute.

Cardiac Component

Finally, cardiac motion principal harmonic, ω_c, is defined as the first local maximum in $I_{\omega_c} = (45, 200)$ rpm and the term is approximated by the first 10 harmonics, $(k\omega_c)_{k=1:10}$. For the sake of an efficient algorithm, ω_c is approximated by the global maximum of Fourier transform amplitude for frequencies in the range $I\omega_c$.

It follows that the motion terms of a sequence lasting N_{Sec} seconds are given by:

$$\begin{aligned} t_g(s) &= \frac{1}{T}\int_{I_g} \widehat{t}(\omega)e^{i\omega s}d\omega \qquad \theta_g(s) = \frac{1}{T}\int_{I_g} \widehat{\theta}(\omega)e^{i\omega s}d\omega \\ t_b(s) &= \frac{1}{T}\int_{I_b} \widehat{t}(\omega)e^{i\omega s}d\omega \qquad \theta_b(s) = \frac{1}{T}\int_{I_b} \widehat{\theta}(\omega)e^{i\omega s}d\omega \\ t_c(s) &= \frac{1}{T}\sum_{k=1}^{k=10} \widehat{t}(k\omega_c)e^{ik\omega_c s} \quad \theta_c(s) = \frac{1}{T}\sum_{k=1}^{k=10} \widehat{\theta}(k\omega_c)e^{ik\omega_c s} \end{aligned} \tag{2.5}$$

where the period $T = N_{Sec}/60$ is the sequence length (in minutes) and defines the domains of integration as $I_g = (-10T, 10T)$ and $I_b = (-45T, -10T) \cup (10T, 45T)$.

Since, even in healthy cases, the heart rate varies along the pullback, the peaks in the Fourier series are spread around the theoretic harmonic frequencies. The more

irregularities in periodicity are, the more spread around the theoretic harmonic the Fourier development is. The harmonics less corrupted by noise are obtained by optical filtering [94]. The technique, widely used in electron crystallography, selects Fourier peaks by thresholding the difference between the amplitude achieved at the harmonic and an average of neighboring amplitudes. Harmonics selected by optical filtering are the only contributions to the sums in (2.5).

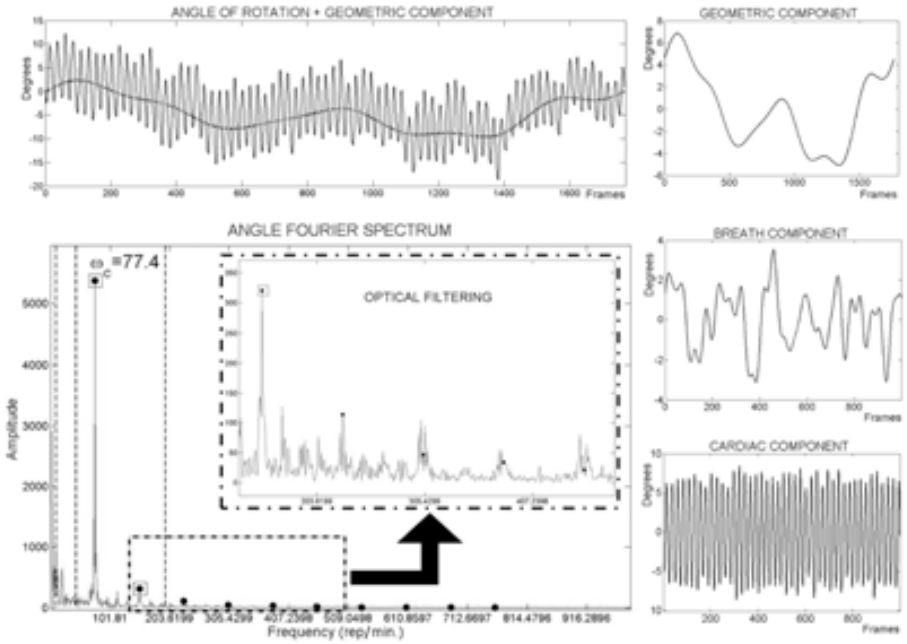

Figure 2.5: Motion Decomposition. Rotation angle and its Fourier decomposition on the left; geometric, breathing and cardiac terms on the right.

Figure 2.5 shows the Fourier terms decoupling for the rotation angle in the top left plot. Vertical lines in the Fourier spectrum of the signal (bottom left plot) indicate the ranges defined for the 3 phenomena. Dots mark the 10 cardiac harmonics and squares the ones selected after optical filtering. The 3 components of the angle are shown in right plots.

2.2 Longitudinal Dynamics

The first step for modeling longitudinal motion in IVUS sequences is retrieving cardiac phase information. Following the general scheme shown in figure 2.6, our image-based algorithm to approach ECG sampling splits in three steps:

1. **Extraction of Signal Reflecting Cardiac Motion**: By the physical coupling [21], luminal area evolution is synchronized to other vessel cardiac phenomena,

Figure 2.6: Pipeline for Image-based Cardiac Phase Retrieval

such as tissue motion or rigid motion. We propose using the latter two to retrieve a signal reflecting motion.

(a) Tissue Motion: Due to the ultrasound properties, image intensity reflects the density of mass and, thus, changes along the sequence either come from morphological changes or contain information about cardiac phase. The evolution of the image Local Mean (LM) for each pixel along the sequence is a 1-dimensional signal, which profile is a combination of the morpho-geometric arterial changes and the periodic variation due to heart beat. Vessel motion is not reflected in the whole vessel section, but only at some salient areas such as plaque or vessel walls. In order to minimize the impact of these image areas we only analyze LM from those pixels reflecting motion by an optical filtering on $\widetilde{LM}$ which selects them.

(b) Rigid Motion: Since rigid in-plane motion comes from artery motion due to heart pumping, the rotation motion profile (θ) computed in section 2.1 also gives information about the cardiac phase.

2. **Signal Filtering for Cardiac Profile Extraction**: In general, the signals reflecting cardiac motion are a combination of morpho-geometric arterial changes and arterial dynamics (including heart beat and breathing). Furthermore, cardiac phase is not constant along the sequence. This suggests that the profile reflecting cardiac motion should be filtered. Following the literature, we use a band-pass filter in order to control the regularity of the signal.

3. **Cardiac Phase Retrieval**: Minimums and maximums of the filtered signals retrieve cardiac phase at end-systole and diastole.

The extraction of the cardiac frequency, ω_c, is necessary for the first two steps. We define ω_c like in the subsection 2.1.3 [91], as the most prominent local maximum in the interval $I\omega_c = (45, 200)$ repetitions per minute of the Fourier development of either LM or θ. In the case of LM signals, this process provides a ω_c for each image pixel and the average of all ω_c for a uniform sample of pixels constitutes our approximation to cardiac frequency.

2.2.1 Step 1 - Extraction of Signal Reflecting Cardiac Motion

1. Tissue Motion

We compute LM in sliding windows of size (empirically set) 9×9 pixels. Since cardiac motion is a periodic signal, $\widehat{LM}$ for those pixels reflecting motion should be as close to a discrete series (given by ω_c multiples) as possible. Other dynamic phenomena,

such as breathing, morphological changes along the sequence and irregularities in heart beat distort the ideal discrete profile. In particular, the theoretic harmonic peaks result in a set of peaks spread around ω_c harmonics. The more irregular the profile is, the more spread around the theoretic harmonic the harmonics of $\widehat{LM}$ are. We consider that points reflecting cardiac motion are those points which its $\widehat{LM}$ has a well-defined harmonic frequencies profile and, at the same time, $\widehat{LM}$ has a large amplitude at ω_c.

From the initial uniform sampling of pixels, only those points with cardiac amplitude over the 80% percentile of all $\widehat{LM}$ amplitudes are considered (figure 2.7). This

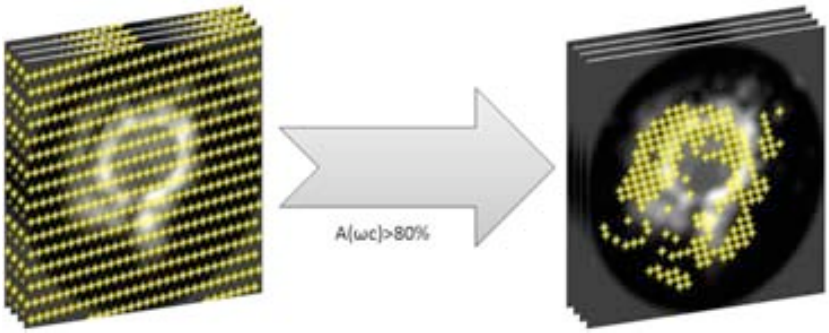

Figure 2.7: First Selection of pixels reflecting motion along the sequence

set will be noted by $\mathcal{MP}$. There might be pixels with a large amplitude but an irregular profile, so that they do not reflect cardiac motion as figure 2.8 shows. Top plots correspond to a pixel reflecting motion while bottom plots correspond to a pixel not reflecting motion. Note the erratic pattern of the last. We remove those pixels with a signal corrupted by noise by means of an optical filtering [94] centered at the principal harmonic ω_c. Optical filtering selects only those Fourier relevant peaks by thresholding the difference between the amplitude achieved at the harmonic and an average of neighboring amplitudes. The signals reflecting cardiac motion are given by the optical filtering of LM signals computed in the set $\mathcal{MP}$. Figure 2.9 shows the set of pixels lastly selected. Finally, we extract a single signal by averaging all signals for selected pixels.

2. Rigid Motion

The rotation angle of the IVUS sequences is due to heart pumping and motion, among other factors (see section 2.1). The process explained in subsection 2.1.3 for extracting the rotation motion profile can be used for extracting the cardiac phase. Although θ is a global score which is prone to be influenced by random motion of background pixels, its computation reduces the impact of random motion by optical filtering.

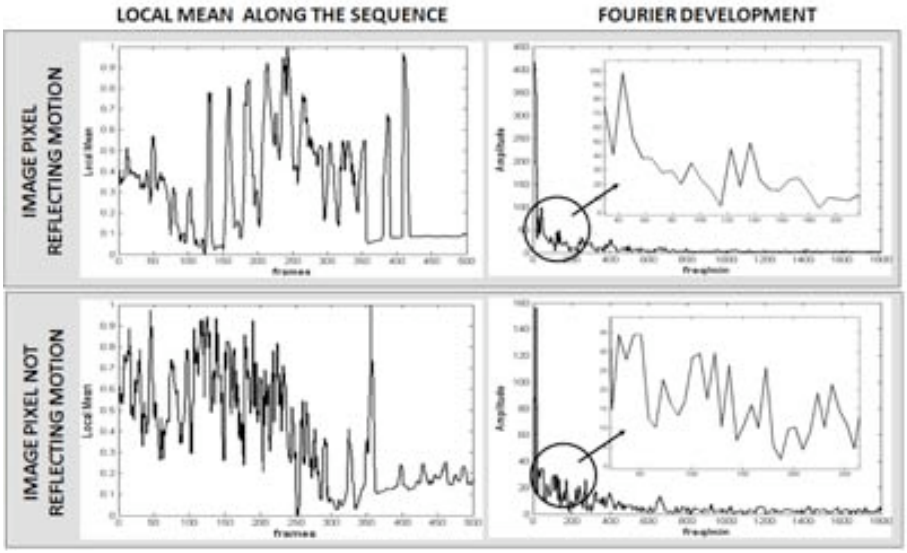

Figure 2.8: Regular Profile (on top) versus irregular profile (on bottom)

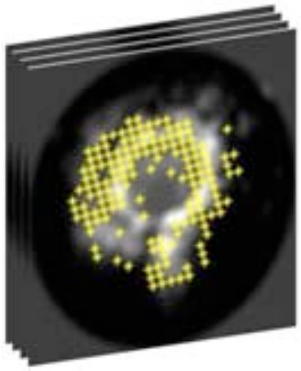

Figure 2.9: Final selection of points reflecting cardiac motion

2.2.2 Step 2 - Signal Filtering for Cardiac Profile Extraction

Even in healthy subjects, cardiac frequency does not keep constant along the sequence, which introduces (among other phenomena) irregularities in the Fourier transform of the cardiac motion profile. Such irregularities corrupt the location of local extrema and, thus, the signal reflecting motion should be filtered. We model the extraction of cardiac phase by filtering the cardiac profile with a bandpass filter. We use two families of filters: Butterworth (B) [16] and Gaussian-based (g) [17]. Both of them are centered at the cardiac frequency ω_c.

The Butterworth filter is defined as follows:

$$B(\omega) = \frac{1}{\sqrt{1 + \left(\frac{|\omega| - \omega_c}{0.6\Delta\omega_c}\right)^{2n}}}$$

where n is related to the filter decay and $\Delta\omega = \delta\omega_c$ to its support. Figure 2.10 shows

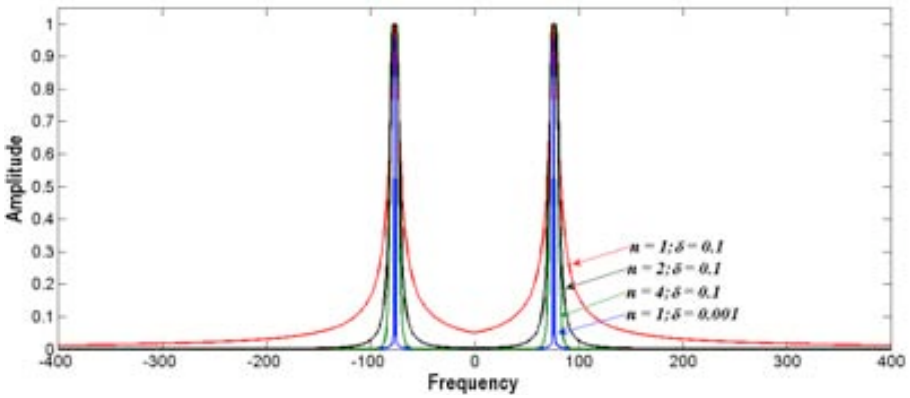

Figure 2.10: Butterworth filters for different parameters

Butterworth filters centered at $\omega_c = 76.5$ rep/min for four different parameters set, $P_1 = \{n = 1; \delta = 0.001\}$ in blue, $P_2 = \{n = 4; \delta = 0.1\}$ in green, $P_3 = \{n = 2; \delta = 0.1\}$ in lilac, and $P_4 = \{n = 1; \delta = 0.1\}$ in red. The last three filters have equal support with $\delta = 0.1$ (including low frequencies) but decreasing decays. P_4 has the less decay, so, low frequencies of the signal would remain. P_3 reduces the impact of low frequencies and P_2 almost suppress them. Concerning P_1, although it has equal decay than P_4, it is the most located around ω_c as δ is the lowest one.

The Gaussian filter is defined as follows:

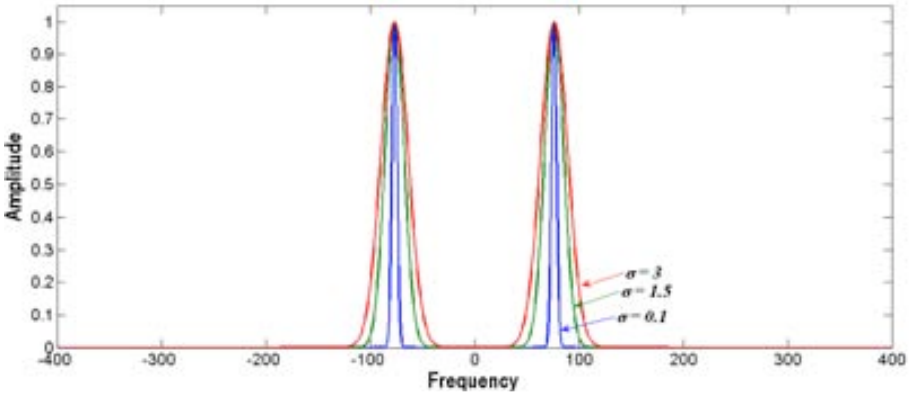

Figure 2.11: Gaussian filters for different parameters

$$g(\omega, \sigma) = \frac{1}{\sigma\sqrt{2\pi}} e^{-(|\omega|-\omega_c)^2/(2\sigma^2)}$$

In the case of a Gaussian-based filter, the decay cannot be handled (it is always exponential) and only its support might be tuned by its deviation σ. Figure 2.11 shows Gaussian filters centered at $\omega_c = 76.5$ rep/min for three different deviations: $\sigma_1 = 0.1$ in blue, $\sigma_2 = 1.5$ in green, and $\sigma_3 = 0.1$ in red. We note that the filter with σ_1 is the most localized around ω_c, while the one with σ_3 is the most permissive with low frequencies.

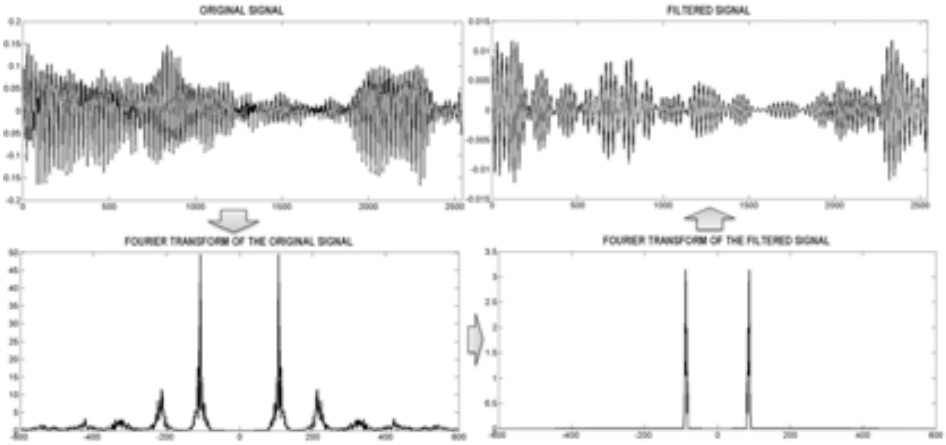

Figure 2.12: Signal filtering with a Butterworth filter with parameters $n = 2; \delta = 0.1$

Figure 2.12 shows a signal obtained in Step 1 by the tissue motion approach filtered by a Butterworth filter with parameters $n = 8, \delta = 0.1$. In the top left image, we present the original filter. The Fourier transform is computed and shown in the bottom left image. The result of the product between its Fourier transform and the filter is shown in the bottom right image. The final result is shown in the top right image.

Finally, the real part of the inverse Fourier transform of the filtered cardiac profile is a smooth signal for the cardiac phase retrieval. Regardless of the filter used we will denote it by $Filt$.

2.2.3 Step 3 - Retrieval of Cardiac Phase

Maximums and minimums of the filtered signal give a sampling at end-systole and end-diastole and, thus, retrieve cardiac phase for each selected pixel. Extrema positions are computed in the Fourier domain using the equation (proposition 1.5.3)

$$\widehat{f'} = 2\pi i\omega \hat{f}$$

for speeding up the process, since $\hat{f}$ has already been computed in step 2.

2.3 Mathematical Issues

As we explained in section 2.1, in the polar domain with origin CM, the remaining affine transformations (rotation and scaling) convert into a horizontal translation (rotation) and a vertical scaling (scaling). In general, the latter would invalidate any computation of the angular translation by means of Fourier analysis and linear regression. In this section we detail the mathematical arguments that support the assumptions made in section 2.1.

In the case of human coronary arteries, scaling is very close to 1 [86], so $\lambda = 1+\varepsilon$ becomes a perturbation of identity given by ε. Furthermore, we restrict computations to a band around the media-adventitia layer, given by $j = j_0 + \Delta j$. By Taylor's formula, it follows that the first order approximation to I_2 is given by:

$$I_2(i,j) = I_1(i+t, j+\varepsilon j) = I_1(i+t,j)+\varepsilon j \partial_j I_1(i+t,j) = I_1(i+t, \Delta j+j_0)+\varepsilon j \partial_j I_1(i+t,j)$$

for ∂_j denoting the partial derivative with respect to the second variable. Since t and j_0 are constant shifts, it follows that the first order approximation is a perturbation of a pure translation which can be written as:

$$I_2 = I_1(i+t_1, j+t_2) + \varepsilon j \partial_j I_1(i+t, j) \tag{2.6}$$

for $t_1 = t$, $t_2 = j_0$ and the second independent variable $j = \Delta j$. We claim that (2.6) only introduces a small (negligible) perturbation in the point cloud generated by $(\omega_1, \omega_2, \rho(\omega))$ not dropping regression accuracy. If we consider the ratio between the Fourier transforms of I_1 and I_2, we have that:

$$\frac{\widehat{I_2}}{\widehat{I_1}} = e^{i\langle \omega, t\rangle} + \varepsilon \frac{\widehat{j\partial_j I_1}}{\widehat{I_1}}$$

and that the phase ρ is given by:

$$\rho\left(\frac{\widehat{I_2}}{\widehat{I_1}}\right) = Imag\left\{\log\left(e^{i\langle \omega, t\rangle} + \varepsilon \frac{\widehat{j\partial_j I_1}}{\widehat{I_1}}\right)\right\}$$

for $Imag\{\cdot\}$ denoting the imaginary part of a complex number and log the complex logarithm. Developing again by Taylor, the first order approach to the above logarithm in a neighborhood of $\varepsilon = 0$ is given by:

$$\log\left(e^{i\langle \omega, t\rangle} + \varepsilon \frac{\widehat{j\partial_j I_1}}{\widehat{I_1}}\right) = \log(e^{i\langle \omega, t\rangle}) + \varepsilon e^{-i\langle \omega, t\rangle} \frac{\widehat{j\partial_j I_1}}{\widehat{I_1}} = i\langle \omega, t\rangle + \varepsilon e^{-i\langle \omega, t\rangle} \frac{\widehat{j\partial_j I_1}}{\widehat{I_1}}$$

Therefore, the points $(\omega_1, \omega_2, \rho(\omega))$ lye on a plane perturbed by:

$$\rho(\omega) = t_1\omega_1 + t_2\omega_2 + \varepsilon Imag\left\{e^{-i\langle \omega, t\rangle} \frac{\widehat{j\partial_j I_1}}{\widehat{I_1}}\right\}$$

Figure 2.13 illustrates the impact of the perturbation, ε, in the shape of the point cloud given by $(\omega_1, \omega_2, \rho(\omega))$ and the coefficients of the regression plane (reported

in the top boxes). We show the point cloud in the case of a pure rotation (given by $\theta = 12$) without scaling and the point cloud perturbed by a scaling equal to $1 + \varepsilon = 1.01$ (central plots) and $1 + \varepsilon = 1.045$ (bottom plots). The non-perturbed point clouds are in circles, while the perturbed ones are in crosses. Two different morphologies have been considered (see images in most top row): a calcified segment (left) and a soft plaque one (right). We observe that the impact of a perturbation ε is either negligible (in the sense that accuracy in regression coefficients is small) as shown in figure 2.13 (central plots) or it results in a random regression plane (fig. 2.13 (bottom plots)).

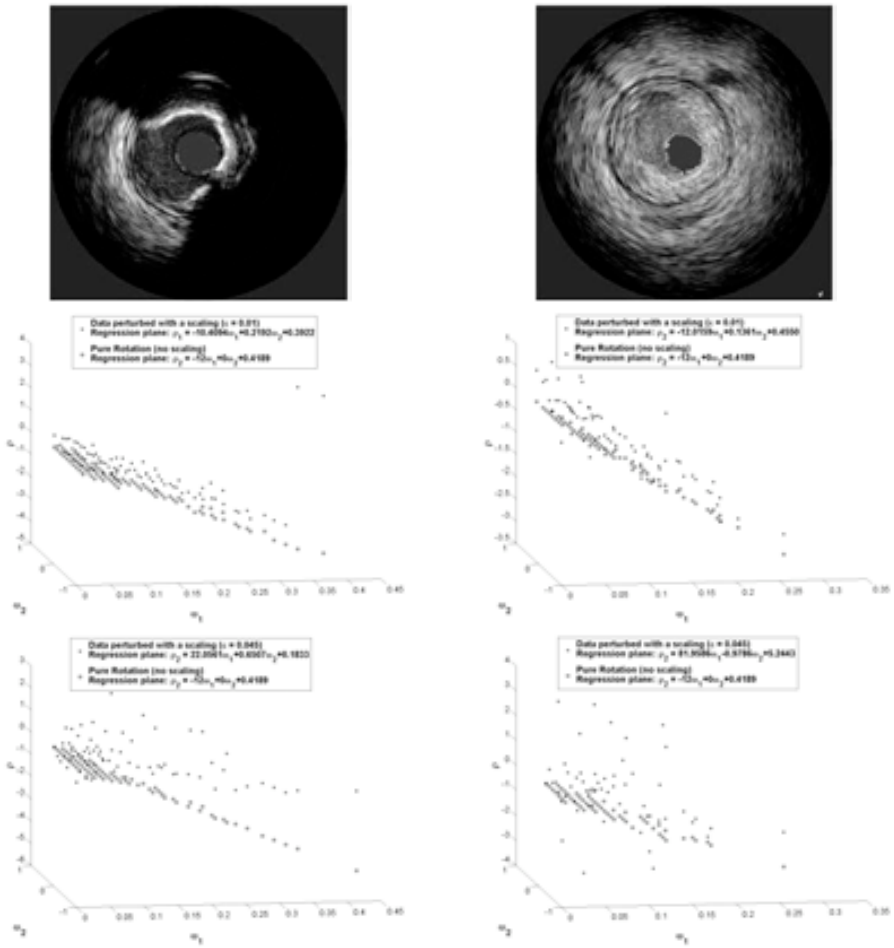

Figure 2.13: Comparison between point clouds given by $(\omega_1, \omega_2, \rho(\omega))$ in the case of a pure rotation (circles) and a rotation perturbed by a scaling (crosses) for two different morphologies, calcium (left) and soft plaque (right). The perturbation on the central plots is $\varepsilon = 0.01$ while $\varepsilon = 0.045$ corresponds to the perturbation on the bottom plots.

The dependency between perturbation and error in translation (first slope of regression plane) is illustrated in the plot in figure 2.14, which shows the error of perturbations for the image shown in the top of the first column of figure 2.13. We note that, in this case, $\varepsilon = 0.025$ (dotted vertical line) is the bound for sub-pixel accuracy (left close-up) in angular translation error and perturbations above $\varepsilon = 0.025$ return a random regression plane with an arbitrary error in the estimated angular translation.

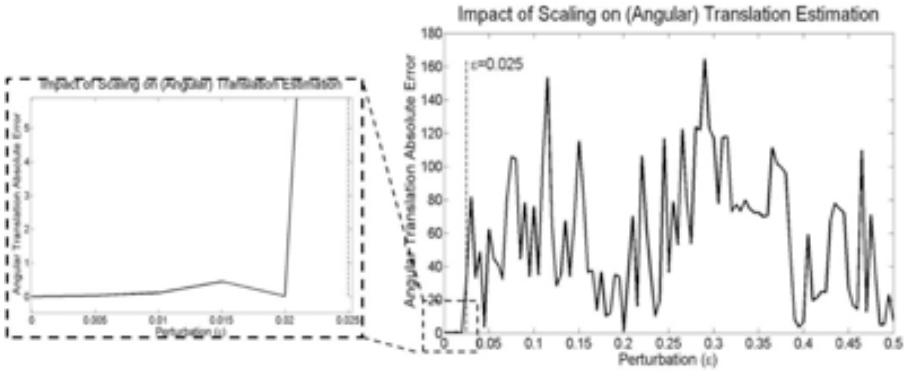

Figure 2.14: Relation between perturbation and error in translation.

We claim that for human coronary arteries, the scaling between two consecutive frames of sequences acquired at 30 fps (which is our digitalization rate) does not reach the critical perturbation of identity. That is, let r_{sys} and r_{dias} denote the arterial radii at end systole and diastole, respectively. Assuming a uniform radial scaling (given by λ) along the cycle, we have that:

$$r_{sys} = \lambda^{NFr} r_{dias} \tag{2.7}$$

for NFr the number of frames per systolic cycle. In devices at 30 frames/sec., the average cardiac cycle length in adults is about 24 frames (75 beats per minute). Since systole approximately constitutes 40% of the cardiac cycle [95], we have that:

$$r_{sys} \approx \lambda^{10} r_{dias} \tag{2.8}$$

Radial deformation of cardiac arteries mainly depends on blood pressure and vessel wall elastic properties. By Hooke's law, the radial increment, Δr, is proportional to the gradient of blood pressure, ∇P, via the relation [71, 21]:

$$\Delta r = (\kappa \nabla P/\pi)^{1/2}$$

where κ is the elasticity coefficient of the coronary artery. Standard values $\kappa = (0.010 \pm 0.020) mm/mmHg$ and $\nabla P \approx 40\ mmHg$ yield that the systole-diastole radial increment is $\Delta r \approx 0.35\ mm$ [96]. Taking into account that the radii of coronary segments [97] are in the range $r = 2.64 \pm 0.3\ mm$, we have that, in average, equation (2.3) equals:

$$r_{sys} = r_{dias} + \Delta r \approx 2.64 + 0.35 = 2.99 \approx \lambda^{10} 2.64$$

which gives an average scaling between consecutive frames of $\lambda = 1.0125$, and, thus, a perturbation $\varepsilon = 0.0125$.

We have computed the error in translation for $\varepsilon = 0.0125$ in a set of images representative of the different vessel morphologies extracted from *in vivo* pullbacks. The corresponding error range is 1.09 ± 0.67. We conclude that, in most cases, the perturbation induced by artery radial scaling does not significantly affect the computation of the angular rotation.

Chapter 3

Deterministic-Statistical Strategies for Structures Exploring

Vessel plaque assessment by analysis of IntraVascular UltraSound sequences is a useful tool for cardiac disease diagnosis and intervention. Manual detection of luminal (inner) and medial-adventitial (external) vessel borders is the main activity of physicians in the process of lumen narrowing (plaque) quantification. Difficult definition of vessel border descriptors, as well as, shades, artifacts, and blurred signal response due to ultrasound physical properties trouble automated adventitia segmentation. In order to efficiently approach such a complex problem, in this chapter we propose combining deterministic tools and statistical classification techniques into a vessel border modeling strategy. By the challenge of the problem, we focus on the detection of the medial-adventitial border.

3.1 General Strategy

The strategy for media-adventitia (simply adventitia from now on) segmentation we suggest summarizes in the following three main steps:

STEP I - IMAGE PREPROCESSING

The preprocessing step splits into :

A. **Polar Transformation of IVUS images**

Advanced techniques for medical imaging segmentation [98] use *a priori* knowledge of the target structure shape. Active shape contours [99] are the usual way to incorporate such knowledge to the model. In the case of the adventitia border, its circular appearance can be imposed by simply transforming images to polar coordinates with the origin at the geometric center of the vessel border. In this coordinate system, the adventitia transforms into a horizontal curve, which significantly simplifies border feature extraction.

B. **Image Filtering** IVUS images are particularly noisy, as well as, in most of cases, adventitia appears as a very weak contour. In order to enhance significant structures while removing noise and textured tissue, it is necessary filtering. We propose two different approaches.

1. ***Structure-Preserving Diffusion (SPD)***
   This diffusion [57], detailed in subsection 1.3.1, modifies classic anisotropic ones [100, 53] by suppressing any diffusion across image level curves. The associated image operator homogenizes image structures grey values according to their geometric continuity and, thus, results in a more uniform response to image local descriptors (edges, valleys, ridges).
2. ***Sequence Stabilization***
   After rigid motion compensation (see section 2.1), image pixel intensity, which is related to tissue density of mass, remains more uniform along frames. It follows that the mean of stabilized sequence blocks enhances vessel structures, while blurring texture and speckle.

STEP II - STATISTICAL SELECTION OF BORDER POINTS

The goal of our classification stage is to compute two binary images (masks), one for vessel borders segments and another for calcium sectors. Extracting vessel borders and calcium points requires defining the functions that best characterize each set, as well as, their most discriminating values. We learn, both, feature space and parametric threshold values by applying supervised classification techniques to a training set of manually segmented images.

A. **Feature Space Design**

Our feature space is designed to discriminate among the set adventitia/intima, calcium and fibrous tissue. Calcium discrimination is needed to discard angular sectors of ambiguous information and fibrous tissue to avoid miss detections of vessel borders. By the polar coordinate system chosen, horizontal edges are the main descriptors of the set adventitia/intima. Image simple statistics (standard deviation and cumulative means) serve to formulate the functions characterizing calcium and fibrous plaque.

B. **Extraction Parameters**

In a segmentation procedure there are two kind of parameters, those that best discriminate among different structures in the feature space and those acting as a filter of fake responses. Discriminating parameters are values acting as a threshold on the feature space, while filtering parameters remove spurious detections from the extracted segments. Both parameters are chosen and tuned to yield an optimal segmentation for a training set of manually traced borders.

STEP III - SEGMENTATION STAGE

The selection stage produces two binary images: adventitia/intima points and calcium sectors. Vessel border segments are modeled by computing an implicit closed representation and, then, an explicit snake representation using B-splines.

A. **Implicit Anisotropic Contour Closing (ACC)**

For the implicit closing we suggest using an Anisotropic Contour Closing [58] based on functional extension principles to complete curve segments in the image mask domain. The use of restricted diffusion operators enables to take into account image geometry and discard calcium and side branches sectors. Since ACC interpolates line segments along image level curves, the implicit reconstruction provides with a faithful closed model of vessel borders. We endow 3-dimensional continuity to such implicit reconstruction by topological area considerations.

B. **Explicit B-Snakes Representation**

We define vessel contours at branching and calcified segments by interpolating ACC radial values in the polar domain with a B-spline snake. B-snakes yield a smooth representation encoded with N control points and conforming to the completion mechanisms of human vision [101]. In the cartesian domain the final smooth model yields an elliptical shape at sectors where no information is available.

3.2 Step 1 - Image Preprocessing

3.2.1 Polar Coordinates

In an IVUS plane, the media-adventitia border is an elliptic-like shape with a relatively small eccentricity (fig. 3.1(a)). In polar coordinates with the origin at the geometric center of the vessel, the adventitia converts into a nearly horizontal line that can be parameterized by the radius. The geometric center does not coincide with the

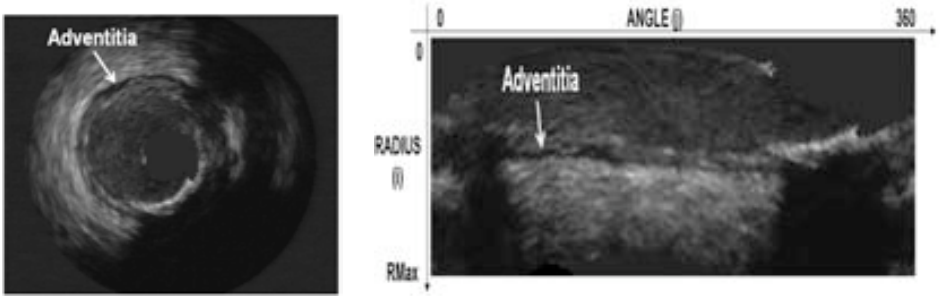

(a) (b)

Figure 3.1: Adventitia images in cartesian (a) and polar coordinates (b).

ultrasound probe (image center) and has to be computed. Its computation it is widely explained in chapter 2 and can be split in three main steps:

1. **Lumen displacement reduction:** In polar coordinates, adventitia is a straight line in the measure that the origin of coordinates is placed at its geometric center (figure 3.2). Any deviation from its geometric center results in an undulation

in its pattern. One source of deviation is lumen displacement due to heart dynamics. The impact of lumen displacement is reduced by taking as origin the image center of mass ICM.

2. **Negative edges extraction:** Negative horizontal edges provide points roughly lying on the adventitia. The geometric center of these points approximates the vessel geometric center.

3. **Geometric displacement reduction:** Displacement due to vessel curvature is reduced by transforming images to polar coordinates with origin the new geometric center computed in step 2.

Steps 2 and 3 are repeated until convergence.

Figure 3.2: Scheme of the strategy for approaching the geometric center of mass

Figure 3.2 shows the three main steps for extracting the points roughly lying on the media-adventitia layer (upper side of the image) and the final result of the image in polar coordinates with the geometric center of mass as origin. For an exhaustive explanation see chapter 2.

From now on, we will work with images in polar coordinates. We will note $AdvPol(i, j)$ the discrete polar transform of an IVUS frame, for the radius, i, and the angle, j, given by:

$$i = 1, \ldots, \min(Nc, Nr) \quad \text{and} \quad j = 1, \ldots, 360$$

where Nc, Nr are the dimensions (columns and rows) of the original IVUS image.

3.2.2 Image Filtering

1. Structure-Preserving Diffusion

   We apply the Structure-Preserving Diffusion (SPD) described in subsection 1.3.1 with smoothing parameters set to $(\sigma, \rho) = (0.5, 2)$. One drawback of SPD smoothing is the computational cost since it is an iterative process. In order to increase its computational efficiency, SPD is applied in a band of interest containing the adventitia layer. This strategy reduces 50% the computation time. The band is automatically defined by the minimum and maximum of the central percentile of pixels used for computing the geometric center. Figure 3.3

shows an original IVUS image in polar coordinates (fig.3.3(a)), the same image filtered in a band by SPD (fig.3.3(a)) and its Sobel edges (fig.3.3(c)).

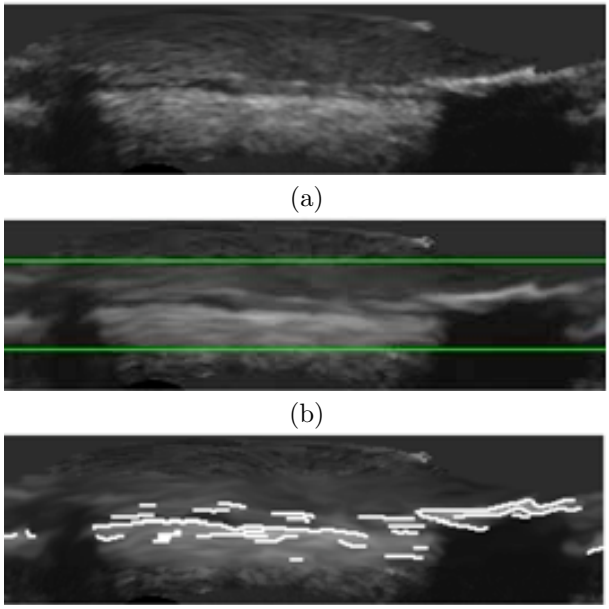

(a) (b) (c)

Figure 3.3: Image SPD Filtering. Polar transformation (a), the SPD image (b) and edges computed by Sobel detector (c)

2. Sequence Stabilization The method explained in section 2.1 has the potential clinical application of tracking continuous vessel structures, such as vessel walls. Stabilized sequences preserve the local density of mass of structures along time in the measure that morphology remains unchanged along the sequence. It follows that the mean of a small number of frames enhances structures, and blurs texture and speckle. In order to achieve a good compromise between morphologic changes and a minimum of frames for blurring non-structure areas, we take blocks of 10 frames. Although the result of this filtering process is less accurate than the one given by SPD, the computational cost of SPD is significantly lower than SPD filtering. Figure 3.4 shows an image filtered by computing the mean over 10 frames (fig.3.4(a)) and its Sobel edges (fig.3.4(b)).

Note that Sobel edges shown in figures 3.3 and 3.4 give continuous profiles of the adventitia for both image filtering methods.

3.3 Step 2 - Statistical Selection of Border Points

The inner and outer vessel borders appearance is so similar that they are assumed to constitute a single class in the training process. Their distinct radial position

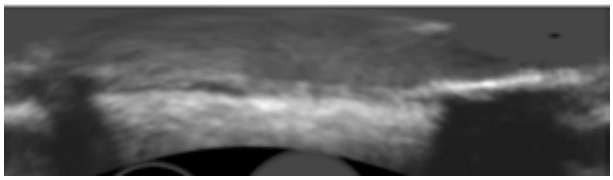

(a)

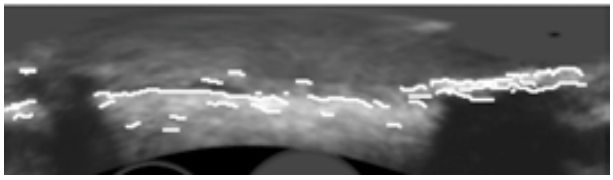

(b)

Figure 3.4: Stabilized Sequence Filtering. Image filtered by the mean of a block of stabilized sequences (a), and edges computed by Sobel detector (b)

suffices to discriminate them [50] in the absence of echo opaque structures, such as calcium. In such cases, the adventitia does not appear and the detection is misled towards the intima. Since the best solution is to discard echo opaque sectors, the training stage also addresses their characterization. We also include fibrous tissue discrimination because it is a main artifact confusing with the adventitia that forces the use of longitudinal cuts [50]. For the sake of simplicity, echo opaque structures will often be referred to as calcium.

3.3.1 Feature Space Design

Based on visual perception, we mainly distinguish adventitia/intima by horizontal edges and echo opaque structures by their shadow underneath. Let $AdvPol$ and (i, j) be the image in polar coordinates and their pixel position respectively. The feature space we propose is a three dimensional space tuned to describe the adventitia/intima set and echo opaque structures.

1. *Horizontal Edges*

   Since in the coordinate system chosen, the adventitia layer is a horizontal dark line, horizontal edges constitute our main descriptor (see chapter 2 for their definition).

   The only image structures yielding large values for e_y are intima, adventitia, calcium and fibrous tissue. Intima and adventitia correspond to negative values, while calcium and fibrous structures yield a negative and a positive response, one for each of their bordering sides.

   The descriptors we have chosen to detect echo opaque plaques and fibrous tissue

are their outstanding brightness and, for calcium, the dark shadow underneath. We propose the following particular functions to quantify such features.

2. *Radial Standard Deviation*

   Striking brightness corresponds to an outlier of the pixel grey value in the radial distribution. We measure it by means of the difference between the pixel gray value and the radial mean. For each pixel (i, j), we define it as

   $$\sigma(i,j) = (AdvPol(i,j) - \nu(\theta))^2$$

   where $\nu(\theta))$ is the radial (i.e. column-wise) mean of the polar image:

   $$\nu(\theta) = \frac{1}{R_{max}} \sum_{i=1}^{R_{max}} AdvPol(i,\theta)$$

   The magnitude of σ is maximum at bright structures (calcium and fibrous plaque) and minimum near the adventitia. In order to distinguish between calcium and fibrous plaque, we add the following shadows detector:

3. *Cumulative Radial Mean*

   For each angle j consider the following cumulative mean:

   $$CS_j(i) = \frac{\sum_{n=R_{max}}^{n=i} AdvPol(n,j)}{R_{max} - i}$$

   For angles with calcium, the function $CS_j(i)$ presents a step-wise profile in contrast to a more uniform response in the presence of fibrous plaque. It follows that the total energy:

   $$ecs(j) = \sum_{i=1}^{i=R_{max}} CS_j(i)$$

   achieves its minimum values only at angles with calcium.

The feature space achieving a maximum separability for our training set is given by:

$$(X, Y, Z) = (e_y, sign(e_y)\sqrt{|e_y\sigma|}, ecs) \tag{3.1}$$

Figure 3.5 shows the feature space for a calcified (1st column) and normal (2nd column) cross-sections. The original images are in the first row, energy from the first derivative in vertical direction in the second row, Radial Standard Deviation in the third and Cumulative Radial mean in the fourth row. From ey energy images (fig.3.5(b),(f)) we extract negative horizontal edges. Radial Standard Deviation (fig.3.5(c),(g)) shows a maximum in calcium sectors (fig.3.5(c)),and fibrous plaques

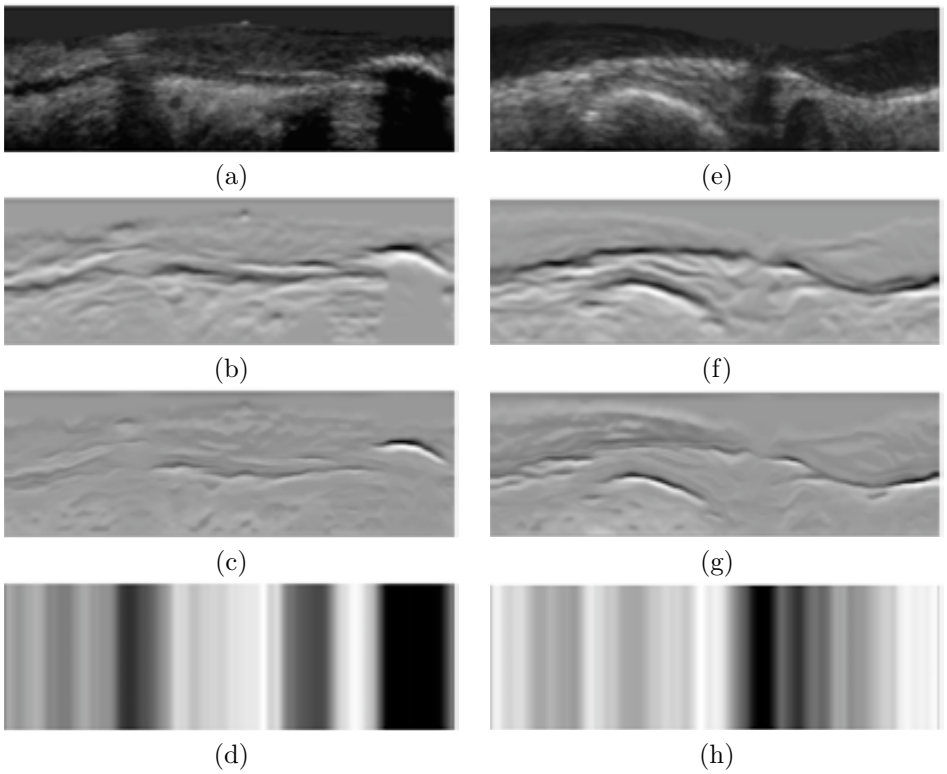

Figure 3.5: Image descriptors. Original images (a),(e) and Vessel Structures Descriptors: Horizontal Edges (b),(f), Radial Standard Deviation (c),(g) and Cumulative Radial Mean (d),(h).

(fig.3.5(g)) and finally, Cumulative Radial Mean (fig.3.5(d),(h)) shows a minimum in calcium sectors (last columns in fig.3.5(d)) and angles with lack of information (middle columns in fig.3.5(h)).

3.3.2 Statistical Parameter Setting

For the computation of the vessel borders and calcium binary images, the classification problem we must face is discriminating among 4 different sets: adventitia/intima (Adv), calcium (Cal), fibrous structures (Fbr) and the rest of pixels (RP). Instead of addressing the 4-class problem as a whole, we will solve several 2-class problems in 2 dimensions.

For its simplicity and proven efficient performance, Fisher linear discriminant analysis [93] serves to reduce dimensionality of the feature spaces. Linear Discriminant Analysis searches for the linear subspace, W, that achieves a maximum separability among the projected classes. In the case of Fisher, separability is measured in terms of maximum separation between class means and minimum within-class scatter. Mathematically, this criterion is formulated in terms of the ratio between the between-class,

S_B, and the within-class, S_W, scatter matrices:

$$\mathbf{S_B} = \sum_{\mathbf{i=1}}^{\mathbf{c}} (\mu_\mathbf{i} - \mu)(\mu_\mathbf{i} - \mu)^\mathbf{t}$$
$$\mathbf{S}_W = \sum_{\mathbf{i=1}}^{\mathbf{c}} \sum_{\mathbf{j=1}}^{\mathbf{N_i}} (\mathbf{Y_j} - \mu_\mathbf{i})(\mathbf{Y_j} - \mu_\mathbf{i})^\mathbf{t}$$

for c the number of classes, N_i the samples per class, μ_i the mean vector of each of them and μ the mean of all samples (Y_j). Fisher discriminant criterion reduces to finding the subspace, W, maximizing:

$$J(\mathbf{W}) = \frac{|\mathbf{W}^t \mathbf{S}_B \mathbf{W}|}{|\mathbf{W}^t \mathbf{S}_W \mathbf{W}|}$$

Because S_B encodes the projection onto the linear subspace given by $\mu_1, \ldots, \mu_c$, it has, at most, rank $c-1$, which bounds W dimension by $\dim W \leq c-1$. In the particular case of a 2-class problem in 2 dimensions, Fisher space is a straight line (solid line in fig.3.6(a)) and discrimination between the two classes is achieved by a threshold on the projection space (line labeled τ_{PF1} in fig.3.6(b)), which induces a splitting of the feature space in two half planes. We will use a Bayesian approach [93] to select thresholding values in terms of miss classification errors. In the two class problem, the classic Bayesian strategy searches for the value that achieves a suitable compromise between the percentage of false positives and false negatives. The approach selects a threshold in terms of how many true positives are detected without considering the amount of noise introduced in the positive detections. Although the criterion is widely used in classification problems, in the case of severe unbalanced classes or object segmentation [102] it is more efficient to select thresholds in terms of the trade-off between precision and recall. Precision is defined as the data retrieved and relevant over all the data retrieved, while recall is the data retrieved and relevant over all the data relevant as the following formulas show:

$$\text{PRECISION} = \frac{|TP|}{|TP+FP|} \qquad \text{RECALL} = \frac{|TP|}{|TP+FN|}$$

In probabilistic terms, precision is the probability that an object is relevant, given that it is retrieved, that is, an estimate of the conditional probability $P(C_1|R)$. Recall corresponds to the probability that a relevant object is retrieved, that is, an estimate of the conditional probability $P(R|C_1)$. Following the usual set-up in information retrieval, we define a decision rule in terms of our given observation vector X, to determine which data is classified as C_1 (the acceptance criterion). In this case the cost function is the following:

$$\alpha_1 P_1(FN) + \alpha_2 P_2(FP)$$

This is the strategy we propose for the computation of the Adv and Cal mask images.

A. Vessel Borders Mask

Borders extraction is achieved by addressing 2 classification issues: discriminate C_1=(Adv,RP) and C_2=(Cal, Fbr) in the (X, Y) plane and, then, separate Adv from RP using X values.

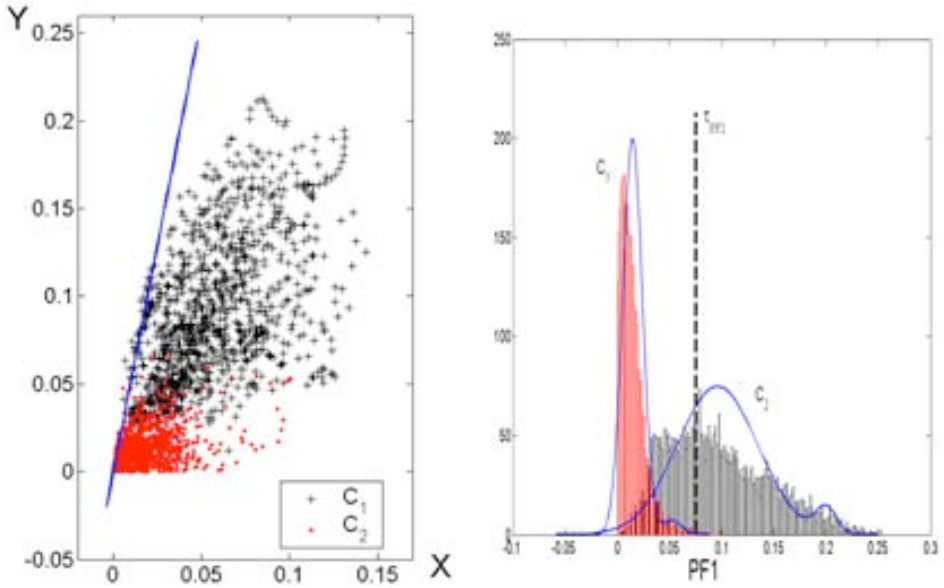

(a) (b)

Figure 3.6: Adventitia/Intima vs Calcium/Fibrous Tissue sets Discrimination. Feature Space (a) and discrimination on the Fisher Projection Line (b)

We remind that Adv, Cal and Fbr are the only tissues yielding large response for X values. It follows that the clustering proposed (C_1, C_2) ensures that after discriminating between Adv and RP, the set classified as Adv will not include any other structures but vessel borders. This avoids the use of longitudinal cuts [50] to distinguish between intima and adventitia, since they are directly identified by their radius.

We discriminate C_1 (positives) and C_2 (negatives) by projecting onto the Fisher space, $PF1$, (see fig.3.6(a)). Since our discriminating problem is detecting as much points on the adventitia as possible, we tune the standard Bayesian threshold in order to achieve a maximum number of true C_1 detections regardless of false positives (see fig.3.6(b)). Such miss classifications are discarded in the subsequent discriminating and filtering steps. Among all thresholds ensuring at least 90% of true C_1 detections, we choose the value, τ_{PF1}, that, in combination with the rest of parameters, yields optimal segmentation results. Figure 3.6 summarizes the main steps of the discrimination between C_1 and C_2. Figure 3.6(a) shows the feature space chosen and the Fisher projection line. Figure 3.6(b) the projected classes onto $PF1$ and a threshold discriminating line τ_{PF1}.

Discrimination between Adv and RP is achieved in the X coordinate domain, as Adv corresponds to large negative values. Large range of Adv values among different patients, suggests the use of an image sensitive threshold rather than a common value for all cases. We adopt a strategy in the fashion of discriminant snakes [55], [103] and select a different value for each column. Radial (column-wise) percentiles (ρ_X)

are used to compute such threshold. Finally, small structures in the vessel borders image can be removed by applying either a length or an area filtering. Although a length filtering is more flexible some 3D continuity might be lost. In contrast, an area filtering is fixed for all frames but takes into account 3D continuity. In our case, we use a length filtering, so that only segments of length above a given percentile (ρ_F) are kept.

If we note by $PF1$ the projection of the (X, Y) space onto the Fisher line, then, for every frame, points are labeled as Adv if they fulfill:

$$PF1 < \tau_{PF1}, \qquad X < \rho_X$$

and their segment length is above ρ_F.

Figure 3.7 illustrates the extraction of adventitia/intima points. In fig.3.7(a) we have the output of the discrimination step and in fig.3.7(b) the result after applying a length filtering.

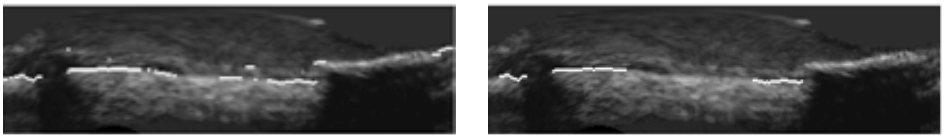

(a) (b)

Figure 3.7: Vessel Borders Point Extraction (1). Adventitia mask resulting from the classification (a) and the final one after length filtering (b)

B. Calcium Mask

The feature space chosen to discriminate calcium from fibrous tissue is given by the projection $PF1$ and the Z coordinate. A threshold on the Fisher space, $PF2$, for the 2D space $(PF1, Z)$ separates Cal and Fbr. Instead of following a Bayesian approach we consider precision-recall curves (as the one in figure 3.8) to select thresholding values, as we can not run the risk of identifying too much Fbr and artifacts (noise) as calcium.

As in the computation of the vessel borders mask, we tune thresholding values and among all thresholds admitting, at most, a 10% of noise , we choose the value, namely τ_{PF2}, that ensures a better segmentation of our training set.

It follows that, calcium points are those pixels that satisfy:

$$PF1 \geq \tau_{PF1} \quad \text{and} \quad PF2 > \tau_{PF2}$$

Figure 3.9 shows the points classified as calcium in white.

The thresholding parameters (τ_{PF1}, ρ_X, ρ_F and τ_{PF2}) hinge on the ultrasonic acquisition device characteristics. The specific values used in our experiments are given in section 5.3.

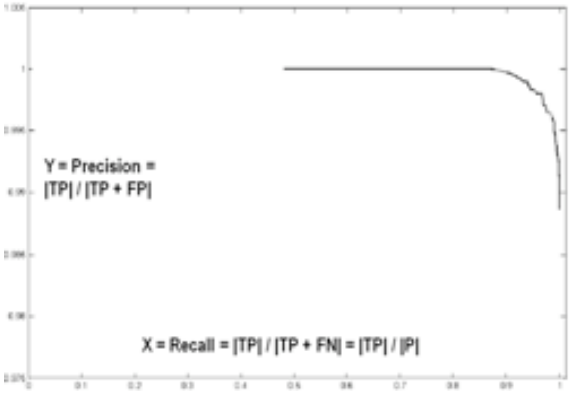

Figure 3.8: Precision-Recall curve to select thresholding values for the computation of calcium mask

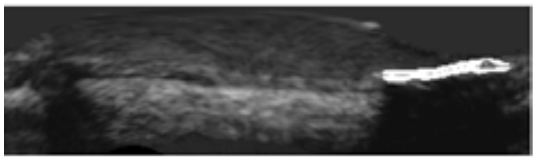

Figure 3.9: Vessel Borders Point Extraction (2). Calcium mask

3.4 Step 3 - Closing Stage

The selection stage produces two mask (binary) images: one for calcium and another one for vessel borders. In the case of non circular patterns (caused by either catheter tilting or vascular modeling in eccentric plaques), the adventitia mask might result in a sparse collection of fragmented curve segments which omits the most curved sectors of the border. In order to correctly restore the vessel geometry, while recovering a smooth representation, we close the adventitia layer in two steps. First we complete them in the mask image domain by an interpolation process based on extension principles. Then, an explicit snake is used to compute a B-spline model of the adventitia.

3.4.1 Anisotropic Contour Closing

We recall that ACC is defined by:

$$I_t = \mathrm{div}(Q\Lambda Q^t \nabla I) \quad \text{with} \quad I_{|\gamma_0} = \chi_{\gamma_0} = \begin{cases} 1, & \text{if the pixel belongs to } \gamma_0; \\ 0, & \text{otherwise.} \end{cases}$$

for

$$Q = \left(\xi^{\perp}, \xi\right), \quad \Lambda = \begin{pmatrix} 1 & 0 \\ 0 & 0 \end{pmatrix}$$

and γ_0 the set of points of the adventitia layer to connect. The vector ξ is the vector guiding ACC and is the eigenvector of minimum eigenvalue of the Structure Tensor,

$ST_{\rho,\sigma}$, computed over the edge map e_y. ACC is implemented using the numeric quick approximation given in section 3.5.2.

The main artifacts to obtain a reliable closed model are side branches, sensor shadows and calcium sectors. In order to avoid wrong continuations at side branches and sensor shadows, ξ is weighted by the coherence of the Structure Tensor:

$$\tilde{\xi} = coh\,\xi \tag{3.2}$$

where

$$coh = \frac{(\lambda_1 - \lambda_2)^2}{(\lambda_1 + \lambda_2)^2}$$

for $\lambda_1 \geq \lambda_2$, $ST_{\rho,\sigma}$ eigenvalues. Concerning calcium sectors, since ξ is well-defined, we modify the weight of (3.2) by a function w_ξ, so that it cancels at calcium sectors. Therefore, the vector guiding ACC is:

$$\begin{array}{l} \tilde{\xi} = w_\xi \xi \\ \text{and} \quad w_\xi(i,j) = \left\{ \begin{array}{ll} 0, & \text{if } (i,j) \in \text{Calcium} \\ coh, & \text{otherwise} \end{array} \right. \end{array}$$

for ξ the minimum eigenvalue of the Structure Tensor $ST_{\rho,\sigma}$

Finally, in order to endow 3D continuity to the final model, we apply a morphological opening (area filtering) of the surface given by blocks of N consecutive ACC closings.

3.4.2 B-snakes

Although ACC closure already contains all available information, by the discrete implementation used, the implicit model is an irregular step-wise model that still presents gaps at side branches and calcium sectors. Besides, the amount of images involved in the sequence suggests searching for a contour representation as compact as possible. This motivates guiding a parametric B-snake towards ACC closure to obtain a compact smooth explicit representation. The general iterative process given in section 1.4 significantly simplifies in our particular case.

In polar coordinates, as the adventitia is convex, we have that $\gamma(s) = (\theta(s), R(s))$ can be represented as a function of the angle, $\gamma = \gamma_\theta = (\theta, R(\theta))$. It follows that the functional (1.10) simplifies to:

$$\begin{array}{rcl} E(R(\theta)) & = & \displaystyle\int_0^{360} E_{int}(R_\theta, R_{\theta\theta}) + E_{ext}(R, R_\tau) d\theta \\ & = & \displaystyle\int_0^{360} (\alpha \|R_\theta\|^2 + \beta \|R_{\theta\theta}\|^2 + (R - R_\tau)^2) d\theta \end{array} \tag{3.3}$$

for R_τ the radius of the target curve and R_θ, $R_{\theta\theta}$ the first and second derivatives of the radius. We parameterize R by a B-Spline given by N control points (R_i, θ_i) where $\theta_i = \frac{360i}{N}$, $i = 1, \ldots, N$. Given that θ_i are uniformly spaced, $\theta(s) = \sum_i c_i(s)\theta_i$ is a linear coordinate change in the angular domain with the parameter relation

$d\theta = \theta_s ds = \lambda ds$, for λ a constant. It follows that the energy functional (3.3) converts to a function of the N control points:

$$E(R_1, \ldots, R_N) = \int_0^{N-1} \left(\lambda^{-1} R_s\right)^2 + \left(\lambda^{-2} R_{ss}\right)^2 + (R(s) - R_\tau(s))^2 \lambda ds$$

for the B-spline radius given by:

$$R(\theta(s)) = R(s) = \sum_i c_i(s) R_i, \text{ for } s \in [0, N-1] \tag{3.4}$$

Since we seek for the control points R_i, $i = 1, \ldots, N$ that minimize the former energy, they must satisfy the system:

$$\frac{\partial E}{\partial R_j} = 0, \forall i \in \{1, \ldots, N\}$$

The jth equation is:

$$\left(\frac{2}{\lambda^2}\right) \sum_i \left(\int \dot{c_j} \dot{c_i}\right) R_i + \left(\frac{2}{\lambda^4}\right) \sum_i \left(\int \ddot{c_j} \ddot{c_i}\right) R_i + \sum_i \left(\int c_j c_i\right) R_i = \int c_j R_\tau$$

It follows that the system of equations (3.4) can be written in matrix form as:

$$(B_1 + B_2 + B_0) R = BR = F_\tau \tag{3.5}$$

where the entries of B_j are sums of the jth derivatives of the spline coefficients c_i. The term $(B_1 + B_2)$ corresponds to the stiffness matrix for B-splines snakes and B_0 is the extra term coming from our particular external energy. The forces F_τ induced by the target curve are computed via the parameter change $R_\tau(\theta(s))$, for $\theta(s) = \sum_i c_i(s)\theta_i$.

Equation (3.5) can be either solved iteratively (gradient descent of the energy (3.4)) or, since F_τ does not depend on R, given by the matrix inversion,

$$R = B^{-1} F_\tau$$

In the first case, the initial snake should be the maximum radius of all points of the ACC mask. In case of using the explicit solution, the target radius is defined, for each angle, as the maximum radius along the i-essim column corresponding to such angle. The cartesian transform of the polar spline given by the above radial control points is our final adventitia model.

Figure 3.10 shows the whole adventitia closing process. The adventitia mask (fig.3.10(a)) obtained from the classification stage is first closed with ACC (fig.3.10(b)) and finally approached with a B-snake (fig.3.10(c)). the green curve in (fig.3.10(c)) is the final snake one would obtain from the initial snake in red.

3.5 Numerical Issues

In this section we address the numerical issues involved is the computation of the adventitia border segmentation.

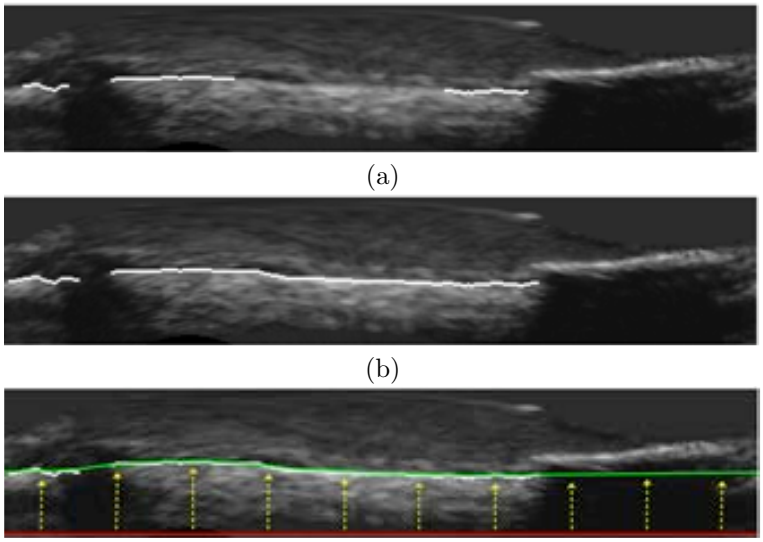

(a)

(b)

(c)

Figure 3.10: Adventitia Closing Step. Adventitia mask (a), ACC closing (b) and final snake (c).

3.5.1 Parameters Tuning

Filtering parameters remove spurious fake detections from the discrimination stage. There are two main candidates to act as filtering parameters of the vessel borders masks, length filtering and area filtering. An exhaustive study determines which is the best set of parameters achieving an optimal segmentation of manually traced borders. By collecting all the parameters controlling the segmentation algorithm, we obtain an error function of 4 variables, $E(\tau_{PF1}, \rho_X, \rho_F, \tau_{PF2})$. The best way of setting the parameters achieving an optimal segmentation is seeking out the global minimum of E. For the sake of a reduction in the computational time required in the training stage, we adopt the following strategy. First, we note that the only way to obtain a global minimum of the function E is by an exhaustive search in its parameter space $(\tau_{PF1}, \rho_X, \rho_F, \tau_{PF2})$, as we lack of an analytic expression for the cost error function. On one hand, we have to choose the thresholds for vessel borders mask, $\tau_{PF1}, \rho_X, \rho_F$. For τ_{PF1}, we have to choose it among all thresholds ensuring at least 90% of true C_1 detections, so τ_{PF1} is a sample of thresholds that ensures this percentage of detections. ρ_X is a radial percentile used to compute an image sensitive threshold for discriminating between adventitia points and the rest of the pixels classified by τ_{PF1}, so ρ_X is a sample of percentiles. Finally, we have to decide between an area filtering or a length filtering and choose the number of pixels as area or the percentile as length, so ρ_F divides in ρ_A and ρ_L and they convert in variables. On the other hand, we have to choose the threshold for calcium mask, τ_{PF2} among all thresholds that ensure at most a 10% of noise, so τ_{PF2} is another sample of thresholds. In this way, for every set of values $\tau^j_{PF1}, \rho^j_X, \rho^j_F, \tau^j_{PF2}$, we obtain a value of our error

function. It follows that we need the computation of the whole process for every set of frames, increasing the computational cost of our study. For the moment, in this work and after a little study of a few patients, we have heuristically fixed ρ_X at 6% and the samples of τ_{PF1} and τ_{PF2} at 3 different values. We perform the filtering parameter learning by analyzing the mean and maximum absolute segmentation errors for a training set of 12 vessel segments which are representative of all kinds of plaques and vessel morphologies. The different samples are:

$$\begin{aligned} \rho_A &= \{90, 100, 110, 120, 130, 140, 150, 160, 170, 180, 190, 200, 210\} \\ \rho_L &= \{77, 78, 79, 80, 81, 82, 83, 84, 85, 86, 87, 88\} \end{aligned}$$

for each combination (τ_{PF1}, τ_{PF2}) of the thresholding parameters, obtaining a different function of ρ_A as an area filtering and ρ_L as a length filtering. These combinations of thresholding parameters are:

$$\begin{aligned} \text{Adv0Cal1} &= (0.0567, -0.1241) \\ \text{Adv0Cal2} &= (0.0567, -0.1468) \\ \text{Adv0Cal3} &= (0.0567, -0.1295) \\ \text{Adv1Cal1} &= (0.0578, -0.1241) \\ \text{Adv1Cal2} &= (0.0578, -0.1468) \\ \text{Adv1Cal3} &= (0.0578, -0.1295) \\ \text{Adv2Cal1} &= (0.0619, -0.1241) \\ \text{Adv2Cal2} &= (0.0619, -0.1468) \\ \text{Adv2Cal3} &= (0.0619, -0.1295) \end{aligned}$$

Figures 3.11 and 3.12 show the different error functions, maximum absolute error functions (fig.3.11) and mean absolute error function (fig.3.12), both for area and length filtering parameters. Each curve corresponds to a combination (τ_{PF1}, τ_{PF2}) with area or length filtering parameters as a variable. As we can see, both minimum of error functions correspond to the combination Adv0Cal1 and the length filtering parameter $\rho_L = 85\%$, obtaining the following results.

3.5.2 Quick ACC

For the sake of a computational cost as small as possible, the following quick algorithm for solving equation (1.8) is used. First recall that the final image yielded by ACC is a mask (i.e. 1's and 0's) of the closed curve and that the whole process might be regarded as integrating the field ξ. Recall that we seek for solutions to the following extension problem:

$$\operatorname{div}(\tilde{J}\nabla I) = 0 \quad \text{with} \quad I_{|\gamma_0} = \chi_{\gamma_0}$$

For a better understanding, we refer to heat equation 1.6. Let us consider the image I as a mass distribution. The vector field $\vec{j} = \tilde{J}\nabla I$ locally describes the direction towards the initial mass moves. On one hand, concerning the final heat distribution, steady states of (1.6) can be described by means of their level sets. On the other hand, in the basis $\{\xi, \xi^{\perp}\}$, $\tilde{J}\nabla I$ develops as:

$$\tilde{J}\nabla I = \lambda_1 \langle \nabla I, \xi \rangle \xi + \lambda_2 \langle \nabla u, \xi^{\perp} \rangle \xi^{\perp} = \langle \nabla I, \xi \rangle \xi$$

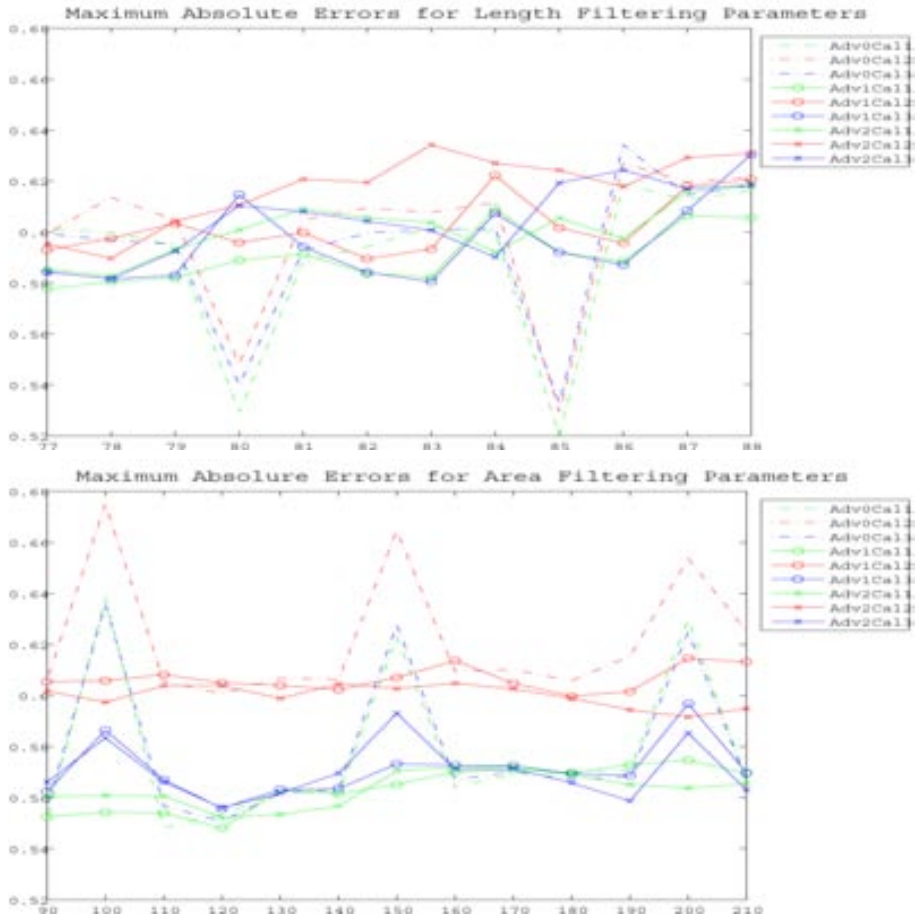

Figure 3.11: Maximum Absolute Error function for Length and Area Filtering Parameters

so, if we denote by Ω the region enclosed by a level curve γ then, $\vec{j} = \langle \xi, \nabla u \rangle \xi$ is tangent to γ. It follows that the Divergence formula yields that the evolution of I_t fulfils:

$$\int_{\Omega} I_t = \int_{\Omega} \mathrm{div}(j) = \int_{\gamma} \langle \vec{j}, \xi \rangle$$

Since our initial mask γ_0 belongs to a level curve and the effect of the diffusion redistributes the mass along it, we have that, for each border point of a segment, the next pixel to be set to 1 is the neighbor in the direction ξ (cross in fig.3.13(b)). Such pixel achieves the maximum correlation between ξ and the gradient of the distance map to the uncomplete curve (dot in fig.3.13(c)). In this way the whole closing process is of the order of the gap (pixel) size.

Figure 3.13 illustrates the grounds of the quick algorithm: For an unconnected

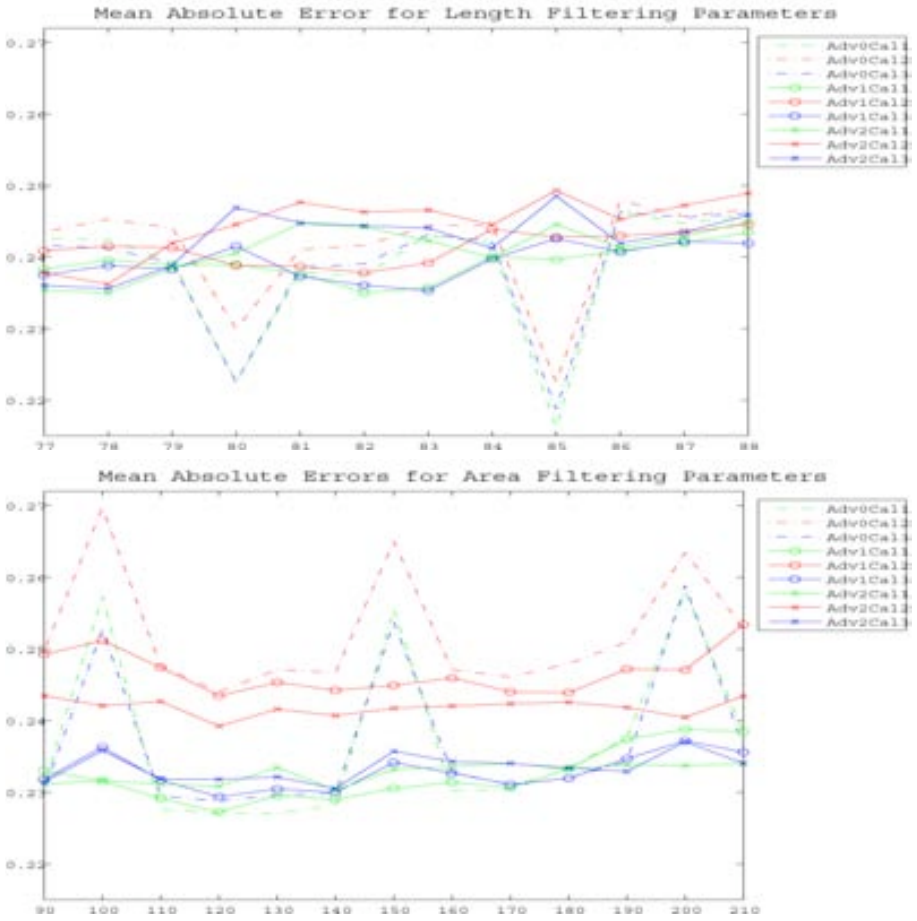

Figure 3.12: Mean Absolute Error function for Length and Area Filtering Parameters

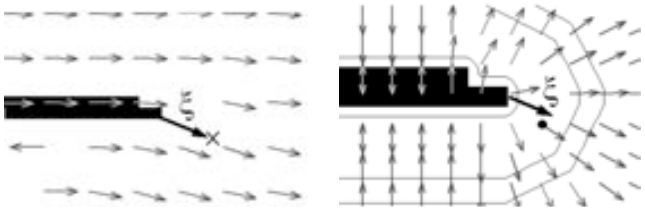

(a) (b)

Figure 3.13: Quick Anisotropic Contour Closing.

segment, fig.3.13(a) shows the vector to be integrated and fig.3.13(b) the distance map gradient used to compute ACC.

Chapter 4

Validation Protocols

An objective evaluation of any technique is a crucial step for ensuring its clinical applicability as reliable as possible. This chapter is devoted to explain the validation protocol designs used for each contribution.

4.1 In-plane Dynamics

Once the rigid in-plane motion of the artery is compensated, it is necessary to know which level of stabilization has been achieved. In real pullbacks there is no objective error measure indicating the amount of motion suppressed, since motion parameters are unknown. In most cases, quality measures are either subjective measures, based on the visual appearance of sequences and longitudinal cuts [12], [65] or rely on extraction of vessel properties (such as strain in [22]). Since that important issue deserves special attention, subsection 4.1.1 is devoted to report a quality score, the Conservation of Density Rate (CDR), for validation of motion compensation in *in vivo* pullbacks. Synthetic experiments serve to validate the proposed score as measure of motion parameters accuracy and compute the accuracy of the motion parameters estimation. *In vivo* pullbacks serve to show the reliability of the presented methodologies in clinical cases.

4.1.1 Conservation of Density Rate

In order to obtain an objective measure of the amount of motion suppressed two main issues should be addressed. Firstly, a similarity measure quantifying image changes along the sequence should be defined. The evaluation of the similarity measure on sequences before and after motion compensation provides two motion scores. A second stage concerns defining a criterion for comparing such scores.

Usual similarity measures (such as normalized mutual information [104] or normalized cross-correlation [81]) yield scalar values based on image intensity (overall) differences. Since they reach an extreme value for aligned images, they are successfully applied to motion detection [105, 22]. In the case of assessing motion compensation in IVUS sequences, they present two main limitations:

- **Computation is sensitive to image digital quality**. In the case of intensity-based metrics (cross-correlation, sum of square differences...) texture and speckle might decrease their accuracy and force a previous image filtering [105]. In the case of probabilistic approaches (e.g. normalized mutual information) values are substantially affected by the number and distribution of histogram bins, which depend on grey-values range and resolution.

- **They provide a global estimation of the alignment rate**. Usual similarity measures are scalar scores computed, at most, over a region of interest. However, vessel motion is not visually noticed at all image pixels but only at some salient areas, such as calcium transitions or adventitia points of extreme curvature. This motivates adopting a local approach and tracking image motion for each pixel. Although cross-correlation and sum-of-square-differences support reliable computation in small neighborhoods (compared to information measures, which need a minimum number of samples for a reliable computation [104]), they are highly affected by image backscatter [105]. Thus, for small sets of pixels, their values might be (random) quantities due to noise.

Regarding the comparison criterion for motion scores computed before and after compensation, it should be noticed that:

- **Extreme values are influenced by the anatomic and morphological differences along the vessel segment.** After motion correction, vessel displacement has disappeared, but morphological changes still remain. That is, even in the best case, comparison of aligned images along the sequence is prone to be a non-constant function depending on the particular morpho-geometric changes of the vessel segment. We claim that, in order to properly quantify vessel alignment, only the dynamic components should be taken into account.

By the above considerations, both, the similarity measure and the comparison criterion, should discard image areas where motion is not observed. Otherwise the score is prone to detect a random motion (due to dark areas, blood, and other artifacts) rather than the true vessel motion. Although the alignment is global, these facts lead to considering a local approach for the definition of both quantities and only use values computed for those pixels which contribute relevant information about global alignment.

Inspired on strategies of classic fluid mechanics [70], we propose exploring the conservation of a physical quantity along the sequence. In particular, we use the local density of mass as it might be approximated by the image local mean, LM (see subsection 2.2.1). As in chapter 2, the LM values for all images provide a pixel-wise function describing the conservation of the local density of mass along the sequence.

Concerning comparison before and after motion compensation, we propose comparing only cardiac terms [29]. Let $\widehat{LM}_0$ and $\widehat{LM}_1$ be the Fourier transforms of LM (or any other similarity score) before (LM_0) and after (LM_1) correction and consider the cardiac frequency ω_c as given in Sect. 2.1.3. We define the Cardiac Alignment Rate (CAR) as:

$$CAR := 1 - \frac{A_{\widehat{LM}_1}(\omega_c)}{A_{\widehat{LM}_0}(\omega_c)} \tag{4.1}$$

for $A_{\widehat{LM}_0}(\omega_c)$ and $A_{\widehat{LM}_1}(\omega_c)$ the amplitudes corresponding to the cardiac frequency of $\widehat{LM}_0$ and $\widehat{LM}_1$, respectively. The CAR index is close to 1 in the case that cardiac motion has been suppressed, whereas approaches zero (or becomes even negative) for a poor rate of motion reduction.

The CAR score is well suited for evaluating cardiac motion suppression at specific image areas (those showing motion in our case). In order to measure the reduction of (global) motion a score involving all valid CAR values should be defined.

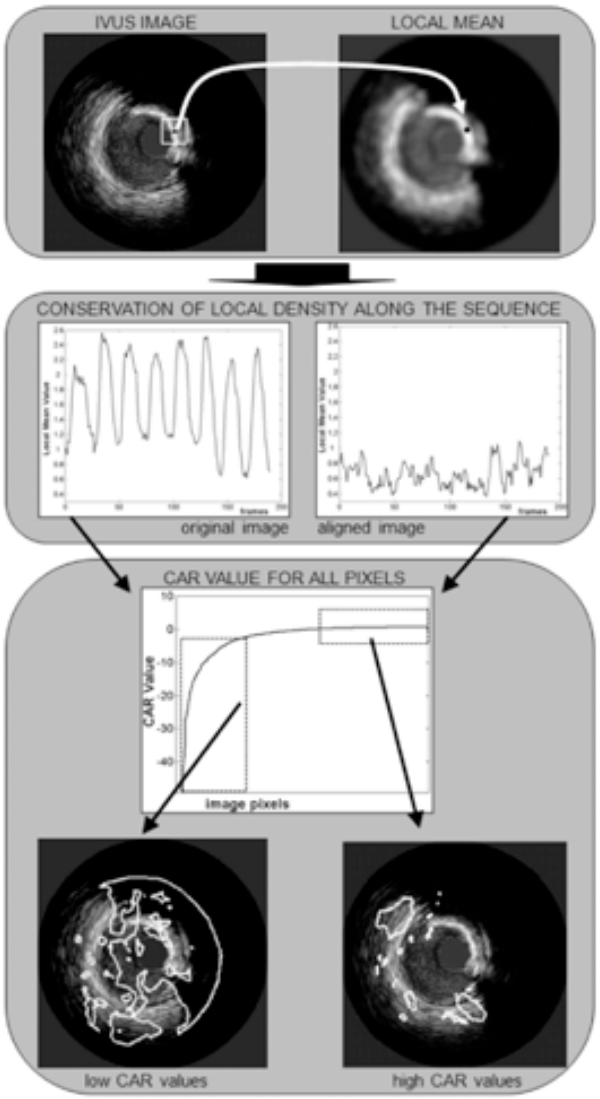

Figure 4.1: Quality Measure Computation

Figure 4.1 sketches the main steps involved in the computation of our quality mea-

sure: computation of the image descriptor (top block), conservation of local density along the sequence (middle block) and the CAR value for all pixels (bottom block). The first block illustrates the modeling of the local density of mass in terms of the image local mean. The local mean of the image (shown on the right hand side) is obtained by computing, for each pixel, the image mean on a window (white square on the left image) centered on each pixel (black point). In the second block, we have the evolution of the local mean at a single pixel before (left) and after (right) image alignment. The plot obtained before alignment presents a well defined periodic behavior; afterwards, although the periodic pattern has been suppressed, the function still presents a variability due to noise and morphologic changes. The third block shows the (sorted) CAR values obtained for all image pixels on the top plot, as well as, the position on the images of those pixels achieving extreme values (dotted squares on the CAR plot) at the bottom. Since we deal with a global movement, all pixels in an image should present a similar CAR value. However, at blood, uniform, and outer areas CAR achieves extreme low values (left bottom image), while pixels showing motion (like calcium-tissue transition on the right image) present a uniform (high) CAR value.

We define our Conservation of Density Rate (CDR) as the trimmed mean [106] of the CAR value:

$$CDR := \mu(\{CAR \mid CAR > prct\}) * 100$$

for $prct$ a given percentile. We have experimentally checked that CDR computed for the superior 66% percentile statistically compares (in the sense of random variables) to the angle relative accuracy (see subsection 4.1.2 and [107]).

4.1.2 Ground Truth

Our ground truth serves to validate the accuracy of the CDR and the accuracy of motion estimation parameters. In order to do so, and since manual definition of ground truth motion is not feasible, computational phantoms have been created. Meanwhile, performance in *in vivo* data shows CDR reliability in clinical cases.

Synthetic Experiments

Our synthetic experiments focus on addressing:

- **Accuracy of the motion parameters estimation.** Rigid motion requires computing two parameters: translation and rotation. Translation accuracy depends on the vessel center of mass, while rotation angle relies on the ability of Fourier analysis for computing global translation. The center of mass bases on the estimation of vessel walls geometry and, thus, its accuracy depends on the appearance of vessel morphology. Concerning angle estimation, the first component of the translation given by Fourier analysis on polar images estimates the rotation angle as far as the center of mass is accurate. Any deviation makes the horizontal component underestimate the rotation angle, since it would also decompose into a vertical shift. We have generated computational dynamic phantoms simulating different vessel morphologies and motion patterns.

- **Reliability of *CDR* as measure of parameters accuracy.** The motion parameters used for generating the phantoms constitute the ground truth. The absolute and relative errors for the difference between estimated and ground truth parameters are our quality measures. In order to validate *CDR* we have compared it to the relative accuracy of the rotation angle (see subsection 4.1.3). We have chosen the angle relative accuracy since its computation depends on the center of mass and, thus, it reflects the overall error. We also report results obtained for the cross-correlation (*CC*) computed on LM images.

Our computational phantoms have been created by applying a rigid motion (given by eq.(2.1)) to still sequences distilled from real pullbacks. We have considered two motion models:

1. **Synthetic Profiles.** In order to illustrate that there are no limits in parameters range, synthetic motions simulate a frame-to-frame angular step of 1^o and 10^o. Two different patterns have been considered: a periodic sinusoidal motion (with several amplitudes and frequencies in the cardiac range) and a quadratic function.

2. ***In vivo* Profiles.** In order to produce motions as realistic as possible we have used motion parameters extracted from *in vivo* sequences using our methodology. Since performance relies on the translation accuracy (strongly dependant on vessel appearance), errors do not benefit from using motion patterns computed with our methodology. We have considered 5 *in vivo* motion patterns.

Regarding vessel morphologies, we have used two models:

1. **Static Model.** It is based on a unique image repeated 200 times simulating a sequence block of a motion-less artery pullback. Errors for this model constitute the lower bound for the methodology accuracy.

2. **Sequence-based Model.** It is obtained by compensating motion of *in vivo* pullbacks and detects the sensitivity to varying morphologies (see fig. 5.1). We have taken 5 vessel segments not belonging to the set used for extracting motion patterns.

In-vivo Data

Performance in real pullbacks has been validated in 32 vessel segments from clinical cases of the Hospital Universitari "Germans Trias i Pujol" in Badalona, Spain:

- 17 Left Anterior Descending (3 ostial, 2 proximal, and 12 medium)
- 11 Right Coronary (2 ostial, 5 proximal, and 4 medium)
- 4 Left main Coronary (2 medium and 2 distal)

Sequences have been recorded using a Galaxy-BostonSci device at 40 MHz with a rotating single transducer and constant pullback (0.5 mm./s.). The digitalization rate was 30 fps and digitized images were 480×480 pixels with a resolution of 0.04

mm/pixel. The segments analyzed are 5-6 mm long (200-300 frames per pullback) and cover different plaques (from soft to calcified), morphologies (including branches), and motion artifacts (such as longitudinal motion).

4.1.3 Goodness Measures

Let us note $\wp^k = \{t_x^k, t_y^k, \theta^k\} = \{p_1^k, p_2^k, p_3^k\}$ the set of motion parameters used to generate the kth frame of a synthetic sequence and $\tilde{\wp}^k = \{\tilde{t}_x^k, \tilde{t}_y^k, \tilde{\theta}^k\} = \{\tilde{p}_1^k, \tilde{p}_2^k, \tilde{p}_3^k\}$ the parameters estimated by our algorithm. For each frame k and motion parameter i, we consider the absolute errors (E_i^k) and relative accuracies (ε_i^k) defined [107] as:

$$E_i^k = |p_i^k - \tilde{p}_i^k| \qquad \varepsilon_i^k = (1 - \frac{|p_i^k - \tilde{p}_i^k|}{p_i^k}) * 100$$

These quantities provide, for each sequence (seq) and motion parameter, an accuracy function. In order to obtain a single quality score for each sequence, we consider the maximum and average of accuracy functions over all sequence frames:

$$E_{i,seq}^{\infty} = \max_k E_i^k, \quad E_{i,seq}^1 = \frac{1}{N}\sum_{k=1}^{N} E_i^k, \quad \varepsilon_{i,seq}^1 = \frac{1}{N}\sum_{k=1}^{N} \varepsilon_i^k \tag{4.2}$$

for N the number of frames of each synthetic sequence.

The statistical ranges of the norms (4.2), given by the mean $\pm$ the variance for all phantoms, indicate the overall accuracy (mean) and stability (variance) of the method. Error ranges are given in pixels for the translation and in degrees (pixel precision in polar coordinates) for the rotation angle.

In the case of CC, normalized cross-correlation [81] is computed between the (whole) image at time k and the reference one and 3 scores are considered:

- CC_0: CC average along the original sequence.
- CC_1:CC average along the processed sequence.
- CAR *on* CC: defined by (4.1) as $1 - \frac{A_{\widehat{CC}_1}(\omega_c)}{A_{\widehat{CC}_0}(\omega_c)}$

Image misalignment in IVUS sequences mainly follows from rigid motion [73] and, in our simulated IVUS sequences, only depends on it. It follows that, in our synthetic experiments, images in processed sequences are aligned in the measure that such rigid motion has been properly compensated. Motion is correctly compensated if and only if motion parameters are correctly estimated. Thus, a measure of the increase in image alignment (CDR) and the accuracy in the estimated parameters (ε_3^1) are two different procedures for assessing the same concept (at least in synthetic tests). Statistical analysis comparing means (paired Student t-test with confidence intervals, CI, at 95%) and pdf's (Kolmogorov-Smirnov goodness-of-fit) are used to check whether there is any significant difference between alignment measures and ε_3^1. We also report Pearson correlation coefficient and regression coefficients for CDR and ε_3^1.

4.2 Longitudinal Dynamics

For the assessment of cardiac phase retrieval, we compare each automatic phase retrieval to a manual sampling of the sequence. Furthermore, each combination of the motion profile extracted with a filter applied retrieves a different sampling. Thus, in order to determine the best strategy, we use the statistical method described in [108] for detecting any significant difference in the performance of the strategies.

4.2.1 Ground Truth

We have analyzed 22 vessel segments 420-690 frames long (7-11.5 mm approximately) from the IVUS database of InCor (Hospital das Clínicas da Faculdade de Medicina, Universidade de São Paulo). Sequences were recorded with a Galaxy-BostonSci device at 40 MHz with a rotating single transducer and constant pullback with speed of 0.5 mm./s. The digitalization rate was 30 fps.

Automatic samplings were compared to the frames achieving extrema lumen areas. These extrema were manually detected by exploring longitudinal cuts by selecting minimums and maximums of intima/lumen and media-adventitia transition profiles. Figure 4.2 shows an example of manual samplings reflecting minimums of lumen area.

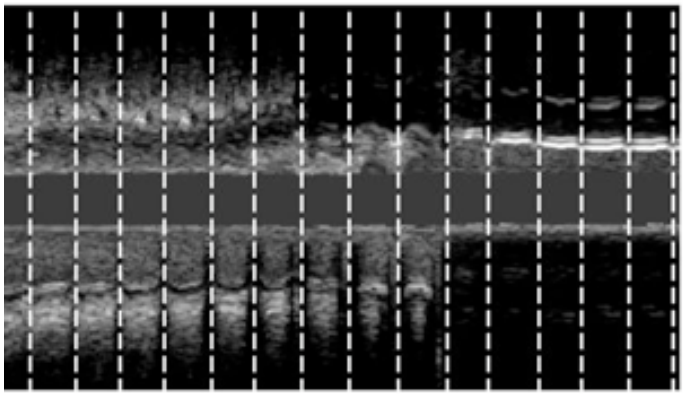

Figure 4.2: Manual Sampling for a Sequence

4.2.2 Goodness Measures

The distances between each manual detected frame and the automatic one most close to it were computed. That is, if s^k and $\tilde{s}^k$ are frame positions in the sequence for a manual and automatic sampling respectively, we define their distance as the absolute differences between their positions:

$$E^k = |s^k - \tilde{s}^k|$$

The distances of all frames provide a distance map for each patient. As for in-plane dynamics, we retrieve a single quantity for each sequence (seq) by averaging E^k over

all sampled frames (N):

$$E^1_{seq} = \frac{1}{N}\sum_{k=1}^{N} E^k$$

Statistical ranges (given by the mean $\pm$ the variance, $\mu \pm \sigma$) of errors for all patients indicate the accuracy of each of the method.

The Nemenyi Test

For each combination of the motion profile extracted with a filter specific, a particular sampling is retrieved. In order to detect if there are any sampling method significantly different, we use the multiple comparison methodology proposed by Demsăr in [108].

The goal is to compare a set of k filters (or configurations for a certain algorithm) over N data sets (signals in our case). Let c_i^j be the performance score (distances in our case) of the $j-$th algorithm on the $i-$th data set. The goal is to decide whether, based on the values c_i^j, the algorithms are statistically significantly different. In addition, when there are more than two algorithms, we are also interested in finding out a particular algorithm differing in performance from the others. In the case of multiple repetitions of the experiments, we can only take into account the variance values σ_i^j if all the observations are independent. In general, the standard validation methodologies do not accomplish this assumption, that is, most of the observations are shared between the different repetitions of the experiment (i.e. in a $K-$fold cross validation, at least $K-2$ groups of samples are shared between two consecutive learning cycles). Since our experiments cannot guarantee independence between observations, from now on the variances will be deprecated, and only the mean value will be considered for the statistical analysis.

In significance testings, the null hypothesis states that all tested algorithms are equivalent. The first step in any significance testing is to determine whereas the null hypothesis can be rejected. In this context, there are two kinds of errors that can appear during the statistical analysis:

Type I: A true null hypothesis is incorrectly rejected. The probability of a *Type I* error is commonly designated by α and is called the *Type I error rate*.

Type II: A false null hypothesis is failed to be rejected. The probability of a *Type II* error is commonly designated by β and is called the *Type II error rate*. A Type II error is only an error in the sense that an opportunity to reject the null hypothesis correctly was lost. It is not an error in the sense that an incorrect conclusion was drawn since no conclusion is drawn when the null hypothesis is not rejected.

The issue of multiple hypothesis testing is a well-known statistical problem. The usual goal is to control the family-wise error, the probability of making at least one *Type I* error in any of the comparisons.

Let r_i^j be the rank of the $j-$th of k algorithms on the $i-$th of N data sets. The Friedman test compares the average ranks of algorithms, $R_j = \frac{1}{N}\sum_i r_i^j$. Under the null-hypothesis, all the algorithms are equivalent and their average ranks R_j are equal.

Thus, the Friedman statistic, given by:

$$\chi_F^2 = \frac{12N}{k(k+1)} \left[\sum_j R_j^2 - \frac{k(k+1)^2}{4} \right] \tag{4.3}$$

is distributed according to χ_F^2 with $k-1$ degrees of freedom when N and k are grater than given numbers (i.e $N > 10$ and $k > 5$). For a small number of algorithms and data sets, exact critical values have been computed [109, 110].

In [111], Iman and Davenport showed that Friedman's χ_F^2 is undesirably conservative and proposed a better statistic, given by:

$$F_F = \frac{(N-1)\chi_F^2}{N(k-1) - \chi_F^2} \tag{4.4}$$

this statistic is distributed according to the F-distribution with $k-1$ and $(k-1)(N-1)$ degrees of freedom. The null-hypothesis will be rejected only if F_F is smaller than the critical value of the F-distribution for a given confidence value α. The critical values can be found in any statistics book, and a representation is shown in table 4.1 and table 4.2.

Table 4.1
F Distribution critical values for $\alpha = 0.1$

$v_1 \backslash v_2$	**1**	**2**	**3**	**4**	**5**	**7**	**10**	**15**	**20**
1	161.45	199.50	215.71	224.58	230.16	236.77	241.88	245.95	248.01
2	18.513	19.000	19.164	19.247	19.296	19.353	19.396	19.429	19.446
3	10.128	9.5522	9.2766	9.1172	9.0135	8.8867	8.7855	8.7028	8.6602
4	7.7086	6.9443	6.5915	6.3882	6.2560	6.0942	5.9644	5.8579	5.8026
5	6.6078	5.7862	5.4095	5.1922	5.0504	4.8759	4.7351	4.6187	4.5582
7	5.5914	4.7375	4.3469	4.1202	3.9715	3.7871	3.6366	3.5108	3.4445
10	4.9645	4.1028	3.7082	3.4780	3.3259	3.1354	2.9782	2.8450	2.7741
15	4.5431	3.6823	3.2874	3.0556	2.9013	2.7066	2.5437	2.4035	2.3275
20	4.3512	3.4928	3.0983	2.8660	2.7109	2.5140	2.3479	2.2032	2.1241
30	4.1709	3.3159	2.9223	2.6896	2.5336	2.3343	2.1646	2.0149	1.9317

At this point, if the null-hypothesis is rejected, we can proceed with a post-hoc test. Otherwise, the methods are not statistically different. Therefore, either they have equal performance or we need more data sets in order to reject the null-hypothesis. There are two possible scenario: The Nemenyi test [112] is used when all classifiers are compared to each other. The performance of two classifiers is significantly different if the corresponding average ranks differ by at least the critical difference

$$CD = q_\alpha \sqrt{\frac{k(k+1)}{6N}} \tag{4.5}$$

where critical values q_α are based on the Studentized range statistic divided by $\sqrt{2}$ (see Table 4.3).

Table 4.2
F Distribution critical values for $\alpha = 0.05$

$v_1 \backslash v_2$	1	2	3	4	5	7	10	15	20
1	39.864	49.500	53.593	55.833	57.240	58.906	60.195	61.220	61.740
2	8.5264	8.9999	9.1618	9.2434	9.2926	9.3491	9.3915	9.4248	9.4413
3	5.5384	5.4624	5.3907	5.3426	5.3092	5.2661	5.2304	5.2003	5.1845
4	4.5448	4.3245	4.1909	4.1073	4.0505	3.9790	3.9198	3.8704	3.8443
5	4.0605	3.7798	3.6194	3.5202	3.4530	3.3679	3.2974	3.2379	3.2067
7	3.5895	3.2575	3.0740	2.9605	2.8833	2.7850	2.7025	2.6322	2.5947
10	3.2850	2.9244	2.7277	2.6054	2.5216	2.4139	2.3226	2.2434	2.2007
15	3.0731	2.6951	2.4898	2.3615	2.2729	2.1582	2.0593	1.9722	1.9243
20	2.9746	2.5893	2.3801	2.2490	2.1582	2.0397	1.9368	1.8450	1.7939
30	2.8808	2.4887	2.2761	2.1423	2.0493	1.9269	1.8195	1.7222	1.6674

Table 4.3
Critical values for the two-tailed Nemenyi test

# methods	**2**	**3**	**4**	**5**	**6**	**7**	**8**	**9**	**10**
$q_{0.05}$	1.960	2.343	2.569	2.728	2.850	2.949	3.031	3.102	3.164
$q_{0.10}$	1.645	2.052	2.291	2.459	2.589	2.693	2.780	2.855	2.920

When the aim is to compare the performance of a set of methods against a given one used as control method, an efficient alternative to Nemenyi test is the Bonferroni correction or similar procedures. The Nemenyi test adjust the critical value by means of $\frac{k(k-1)}{2}$ comparisons. However, for comparing a set of methods against a control method $k-1$ comparisons are enough. Although Bonferroni and similar test are generally conservative and can have little power, in this case, they are more powerful than the Nemenyi test. The test statistics for comparing the $i-$th and $j-$th classifier using these methods is

$$z = \frac{(Ri - Rj)}{\sqrt{\frac{k(k+1)}{6N}}} \tag{4.6}$$

The z value is used to find the corresponding probability from the table of normal distribution, which is then compared with an appropriate α. The tests differ in the way they adjust the value of α to compensate for multiple comparisons.

The Bonferroni-Dunn test [113] controls the family-wise error rate by dividing α by the number of performed comparisons $k-1$. The alternative way to compute the same test is to calculate the CD using equation (4.5), but now using the critical values for $\frac{\alpha}{(k-1)}$ (see Table 4.4). The comparison between tables for Nemenyi's and Bonferroni-Dunn's test shows that the power of the post-hoc test is much greater when all classifiers are compared only to a control classifier. We thus should not make pairwise comparisons when we, in fact, only test whether a newly proposed method is better than the existing ones.

Table 4.4
Critical values for the two-tailed Bonferroni-Dunn test. The number of methods include the control method

# methods	2	3	4	5	6	7	8	9	10
$q_{0.05}$	1.960	2.241	2.394	2.498	2.576	2.638	2.690	2.724	2.773
$q_{0.10}$	1.645	1.960	2.128	2.241	2.326	2.394	2.450	2.498	2.539

4.3 Vessel Structures

In this case, ground truth is given by manual identification of structures in IVUS images. Since discrepancies among experts provide a non-unique ground truth, we present a protocol based on comparisons of inter-observer variability to manual segmentations.

4.3.1 Ground truth

The study group has been designed to assess the ability of the reported algorithm to detect the adventitia border in the presence of different plaques, artifacts and vessel geometries. A total number of 5400 images extracted from 11 different cases have been tested. The sequences analyzed are clinical cases of a Boston Scientific Clear View Ultra scanner at 40 MHz with constant pull-back at 0.5 mm/s and acquisition rate of 25 frames/s from the Hospital Universitari Germans Trias i Pujol in Badalona (Spain). The digitalized sequences are 384×288 images with a spatial resolution of 0.0435 mm per pixel. We have segmented 22 vessel segments of a length ranging from 4 to 6 mm (200-300 frames) and including:

- 6 segments with uncomplete vessel borders due to side-branches and sensor guide shadows.
- 5 calcified segments.
- 9 segments with non calcified plaque.
- 2 normal segments.

For each segment, the adventitia has been manually traced every 10 frames by 4 experts in IVUS image interpretation, which yields a total number of 540 validated frames with 4 different manual models each.

4.3.2 Goodness Measures

To assess segmentation accuracy, the automatically detected borders have been compared to the manual models. Accuracy is quantified with the following standard measures:

1. *Absolute and Signed Distances.*

   Distance maps to manual contours serve to compute the difference in position between automatic and manually traced curves. Such maps encode for each pixel, $p = (x_p, y_p)$, its distance to the closest point on the manual contour:

$$\begin{aligned} D(p) &= \min_{q\in\gamma}(d(p,q)) \\ &= \min_{q\in\gamma}\left(\sqrt{(x_p - x_q)^2 + (y_p - y_q)^2}\right) \end{aligned} \tag{4.7}$$

   where q are points on the manually identified contour. Signed distances ($SgnD$) [82] weight the value $D(p)$ depending on wether the pixel p lyes inside or outside the target curve γ. Its mean value detects any bias in curve position, that is, wether detections are systematically bigger or smaller than manual segmentations.

   We will consider absolute (in mm) and relative (in %) distance errors. Absolute errors are given by formula (4.7), while relative ones are the ratio:

$$RelD(p) = 100 \cdot \frac{D(p)}{d(q,O)}$$

   where the origin, O, is the mass center of the manual contour and q is the point achieving the minimum in (4.7). Since relative errors take into account the true dimensions of the vessel, they reflect positioning errors better.

   For each distance error, its maximum and mean values on the automated contour are the error measures used to assess position accuracy. If PixSze denotes the image spatial resolution and p is any point on the automatically traced adventitia, then the set of functions measuring accuracy in positions are:

   - **Maximum distance errors** (in mm and %):

$$\begin{aligned} MaxD &= \max_p\left(D(p)\cdot PixSze\right) \\ RMaxD &= \max_p\left(RelD(p)\right) \end{aligned}$$

   - **Mean distance errors** (in mm and %):

$$\begin{aligned} MD &= \text{mean}_p\left(D(p)\cdot PixSze\right) \\ RMD &= \text{mean}_p\left(RelD(p)\right) \end{aligned}$$

   - **Mean signed distance error** (in mm):

$$MSD = \text{mean}_p\left(SgnD(p)\cdot PixSze\right)$$

2. *Area Differences.*

   Binary images of manual, $I_M(i,j)$, and automatic, $I_A(i,j)$, borders serve to compute the following measure for area accuracy:

- **Percentage of Area Differences**

$$AD = 100 \cdot \frac{\sum_{i,j} |I_M(i,j) - I_A(i,j)|}{\sum_{i,j} I_M(i,j)}$$

The interval given by the mean ± standard deviation computed over the 4 experts contours indicate the statistical range of values for each of the automated errors (MaxD, RMaxD, MD, RMD and AD).

Inter-observer variability is obtained by computing the error measures for the models made every two independent observers and it, thus, quantifies discrepancy among experts. A Student T-test is used to determine if there is any statistical significant difference between inter-observer and automated distance errors average.

Chapter 5

Experiments

5.1 In-plane Dynamics

5.1.1 Synthetic Data

Tables 5.1 and 5.2 report the absolute error ranges (E^1, E^∞) for synthetic motion profiles. Note that errors do not substantially differ between the two synthetic motion profiles considered (periodic and quadratic). As expected, error ranges increase in table 5.2 (Sequence Model) as morphological changes appear. Regarding the step, there is no difference in E^1 between 1° and 10°. Student (pairwise) t-tests return a p-value equal to 0.99 ($CI = (-0.0098, 0.0091)$) for Static models and equal to 0.98 ($CI = (-0.96, 0.95)$) for Sequence ones.

Table 5.1

Angle Absolute Error Ranges for Synthetic Profiles - Static Model

	1° step		10° step	
	E^1	E^∞	E^1	E^∞
Periodic	0.016 ± 0.081	0.032 ± 0.013	0.016 ± 0.008	0.036 ± 0.017
Quadratic	0.024 ± 0.017	0.051 ± 0.023	0.025 ± 0.013	0.053 ± 0.016

Table 5.2

Angle Absolute Error Ranges for Synthetic Profiles - Sequence Model

	1° step		10° step	
	E^1	E^∞	E^1	E^∞
Periodic	2.215 ±0.840	4.904 ±1.446	2.217 ±0.827	4.934±1.417
Quadratic	2.349 ±1.245	5.164 ±1.817	2.366 ±1.316	5.228±1.813

Figure 5.1 shows box plots for $(E_i^1)_{i=1,2,3}$ for *in vivo* profiles and Sequence models. A reference image from each of the sequences is shown at the bottom row. Case1 and Case2 are vessel segments centered at the catheter, Case3 and Case4 are off-center and Case5 is a branch with longitudinal motion. A horizontal line indicates the bound for sub-pixel accuracy. In general, there is an increase in angular error due to its dependency on the center of mass.

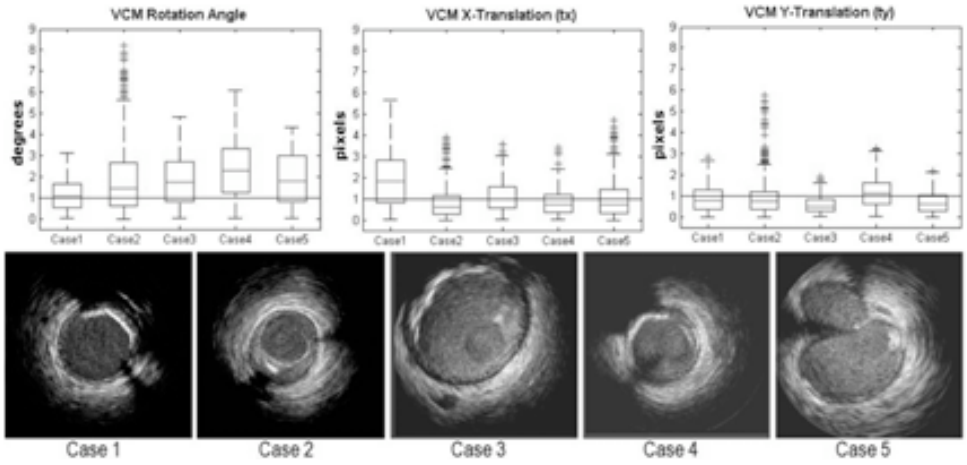

Figure 5.1: Box plots for the sequence-based phantoms (first row) and a representative image of the sequence for each phantom (second row)

In table 5.3 we summarize the absolute error ranges for *in vivo* motion profiles. Static models achieve sub-pixel accuracy for average ranges (E^1). As errors for synthetic profiles, errors increase for Sequence models, although average (E^1) ranges are below 1.67 pixels for translations (t_x) and 2.44° for rotations (θ).

Table 5.3

Absolute Error Ranges for *in vivo* Profiles.

	Static Model		Sequence Model	
	E^∞	E^1	E^∞	E^1
t_x	1.50 ± 1.23	0.49 ± 0.42	3.48 ± 0.90	1.09 ± 0.58
t_y	1.53 ± 0.88	0.48 ± 0.25	2.94 ± 1.24	0.79 ± 0.16
θ	1.13 ± 0.40	0.34 ± 0.17	4.98 ± 1.50	1.72 ± 0.72

Tables 5.4 and 5.5 report the statistics summary for the validation of *CDR* (using the upper 66% *CAR* percentile) as accuracy measure. In table 5.4 we report ranges for ε_3^1 and *CDR*, as well as, the (pairwise) t-test p-value and the confidence interval (CI). There is no significant difference in means between *CDR* and ε_3^1 with at most a ±9% of discrepancy. According to a Kolmogorov-Smirnov test for comparison of random variables, there is no evidence of difference in their distributions (with a p-

Table 5.4
CDR vs Angle Relative Error

	ε_3^1	*CDR*	p-val	CI
Static	95.09 ± 4.63	93.56 ± 4.86	0.3334	(-1.67, 4.73)
Sequence	76.83 ± 13.00	76.59 ± 8.39	0.9545	(-8.60, 9.08)

Table 5.5
CDR vs Other Alignment measures

	CDR	CC_0	CC_1	CAR on CC
Static	93.56 ± 4.86	89.27 ± 9.46	93.57 ± 8.43	70.95 ± 21.53
Sequence	76.59 ± 8.39	88.24 ± 6.24	89.58 ± 5.72	28.36 ± 45.63

value of 0.3334 and 0.9545 for Static and Sequence phantoms, respectively). Table 5.5 is devoted to comparison of *CDR* to normalized cross-correlation measures: CC_0, CC_1 and CAR *on* CC. Regarding CC, in the absence of morphological changes (Static Model), CC_1 and CDR ranges are similar. On Sequence phantoms, there is no significative difference between CC_0 and CC_1, which suggests using the CAR score. However, the global nature of CC, makes CAR on CC underestimate the amount of motion suppressed.

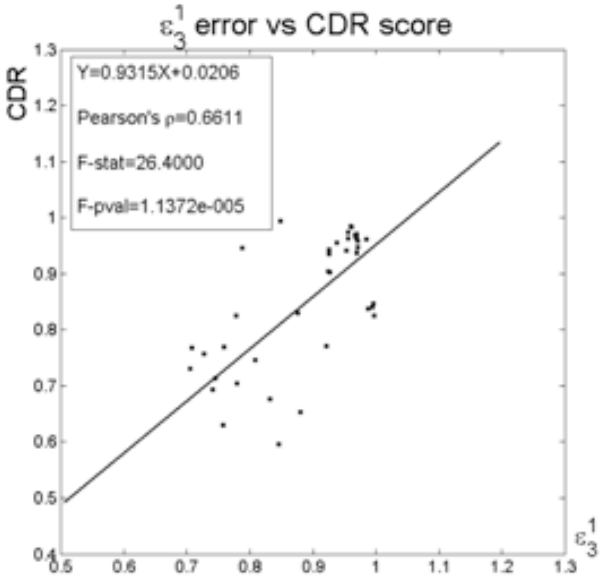

Figure 5.2: Linear Correlation between CDR and Angle Relative Accuracy (ε_3^1).

Figure 5.2 shows the regression line for the point cloud given by plotting ε_3^1 (X variable) against CDR (Y variable). The regression coefficients for the model $Y = b\ X + a$ are $b = 0.9315$ and $a = 0.0206$. Pearson's correlation coefficient (ρ) indicates a significant linear dependency ($\rho = 0.6611$). Finally, the F-statistics for testing $b = 0$ clearly show (with $F - pval = 1.1372e^{-5}$) that both scores are correlated.

5.1.2 In vivo Data

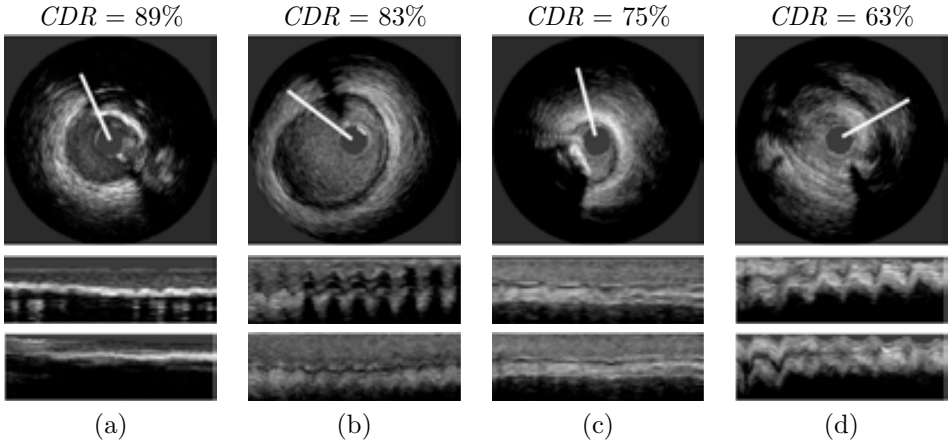

Figure 5.3: Longitudinal cuts for sequences of four different patients (columns), from the best corrected sequence (a) to the worst corrected one (d). Original frames are shown on the first row, original longitudinal cuts on the second row, and corrected ones on the third row.

Figure 5.3 shows four cases with decreasing *CDR* values (from left to right): 89%, 83%, 75%, and 63%. The first row shows a frame of the original sequences. The corresponding longitudinal cuts at the angles indicated by white lines are shown on the second row and the same cut after sequence alignment on the last one. The sequence in the first column (fig.5.3(a)) presents a structure misalignment due to rotation. The calcium shadow appears and disappears in the original longitudinal cut, whereas it shows a uniform appearance after alignment. In the second column (fig.5.3(b)) translation introduces a saw-shape in the original longitudinal cut (especially at the end of the segment). After compensation, only a faint undulation due to radial dilation remains. The longitudinal cut in fig.5.3(c) shows a straight profile (both before and after alignment) in spite of a lower *CDR*. This phenomenon, which appears in the absence of motion, is inherent to any relative measure like *CDR* [107]. Finally, in fig.5.3(d) we show the worst performer, both, in terms of longitudinal cut appearance and *CDR* value. Since a proper alignment is only achieved at the second half of the segment, we have 63% of motion reduction. Regarding objective measurement of IVUS alignment, we have that the statistical range for *CDR* gives an overall motion reduction of $82.05\% \pm 6.61\%$.

5.2 Longitudinal Dynamics

The methodologies were implemented in Matlab code on a Pentium(R) with 3GHz CPU. The average processing time per frame was 36 ms. The set of filters scanned, G_i for gaussian filters and B_i for Butterworth ones is the following.

$$G_1 : \{\sigma = 0.001\}; \quad G_2 : \{\sigma = 1.5\}; \quad G_3 : \{\sigma = 10\}$$

$$\begin{array}{lll} B_1 : \{n = 1, \delta = 0.5\}; & B_2 : \{n = 1, \delta = 0.05\}; & B_3 : \{n = 1, \delta = 0.005\}; \\ B_4 : \{n = 2, \delta = 0.5\}; & B_5 : \{n = 2, \delta = 0.05\}; & B_6 : \{n = 2, \delta = 0.005\}; \\ B_7 : \{n = 4, \delta = 0.5\}; & B_8 : \{n = 4, \delta = 0.05\}; & B_9 : \{n = 4, \delta = 0.005\} \end{array}$$

Tables 5.6 and 5.7, report the average ranks reflecting each filter performance (the smaller, the better).

Table 5.6

Average Rank of the Gaussian Filters with parameters given by σ for Nemenyi Test

σ	**0.001**	**1.5**	**10**
Rank	9.43	4.71	5.75

Table 5.7

Average Rank of the Butterworth Filters with parameters given by (n, δ) for Nemenyi Test

$\mathbf{n} \backslash^{\delta}$	**0.5**	**0.05**	**0.005**
1	4.93	4.71	8.12
2	5.28	4.96	8.62
4	5.81	6.18	9.43

For a significance level of 0.1, the Nemenyi critical difference (CD) is 3.86. The test detects that Butterworth filters with $n = 1, 2, 4$, $\delta = 0.005$ (B_3, B_6 and B_9) and Gaussian with $\sigma = 0.001$ (G_1), which are too restricted around ω_c, are significantly worst. The Nemenyi test also reports that there is not enough evidence of a significantly different performance among the remaining methods. Figure 5.4 shows the rank of filters from right to left (the best is on the right) together with the critical difference in order to visually compare all filters. There are two distinguished sets, but there are no significative differences between the filters in each set. Table 5.8 reports the ranges, by the mean $\pm$ the variance ($\sigma \pm \mu$) of the filters of the set with better ranks. Values in the first column are in frames, the ones of the second column

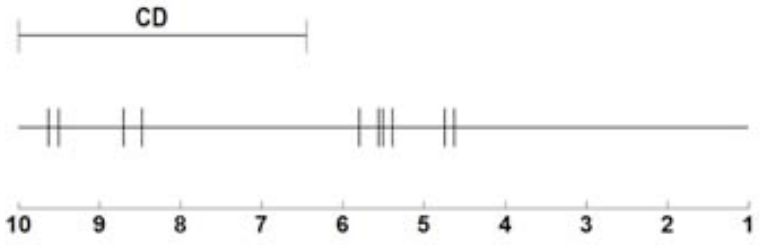

Figure 5.4: Comparison of different filters using the Nemenyi test.

are in seconds and the last column correspond to the values in millimeters. As figure 5.4 shows, there is no significative difference between them. The Gaussian filter with $\sigma = 1.5$ achieves the best results with an error within 3.26 ± 1.55 frames, which corresponds to 0.05 ± 0.03 mm.

Table 5.8
Average Errors of the best set of filters

Method	Frames	Seconds	Millimeters
G_2	3.2580 ± 1.5458	0.1086 ± 0.0515	0.0543 ± 0.0258
G_3	3.5499 ± 1.5352	0.1183 ± 0.0512	0.0592 ± 0.0256
B_1	3.4336 ± 1.6755	0.1145 ± 0.0558	0.0572 ± 0.0279
B_2	3.4455 ± 1.7838	0.1148 ± 0.0595	0.0574 ± 0.0297
B_4	3.3620 ± 1.7163	0.1121 ± 0.0572	0.0560 ± 0.0286
B_5	3.5272 ± 1.7959	0.1176 ± 0.0599	0.0588 ± 0.0299
B_7	3.4065 ± 1.7005	0.1136 ± 0.0567	0.0568 ± 0.0283
B_8	3.6655 ± 1.8971	0.1222 ± 0.0632	0.0611 ± 0.0316

Figure 5.5 shows an example of the automatic sampling on a real longitudinal cut. The top image is a longitudinal cut of 42 mm. long showing a side branch on the upper half. The left bottom image shows the image-based ECG sampling in dashed lines at the side branch segment. The right bottom image shows the longitudinal cut sampled at end diastole rate.

Figure 5.6 shows the performance of our method for the Gaussian filtering in 2 large longitudinal cuts. The original cuts are in the left, while the cuts sampled at end diastole rate are in the right. For the first segment, we can notice the continuous profile for the lumen contour, while in the second segment, we can follow up the calcium plaque present in the vessel.

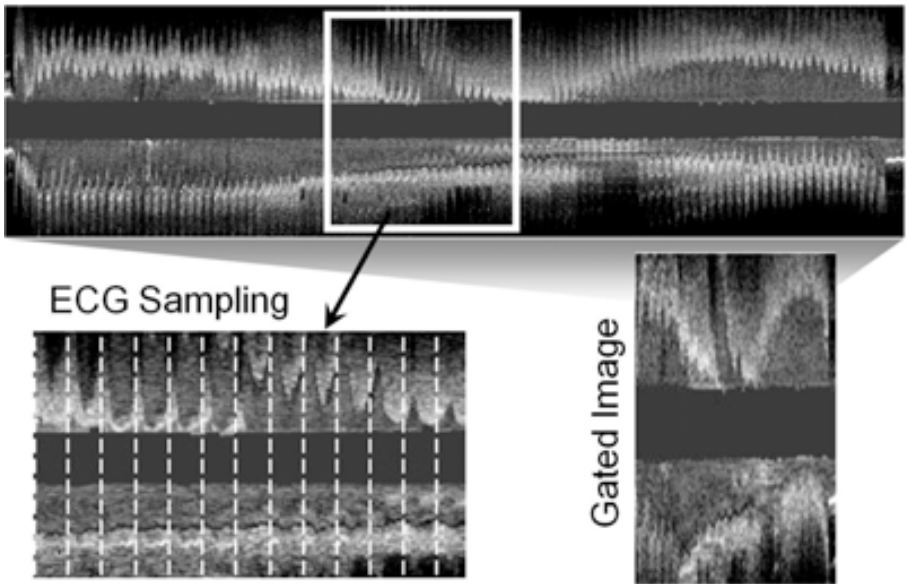

Figure 5.5: Image-based ECG sampling on a longitudinal cut.

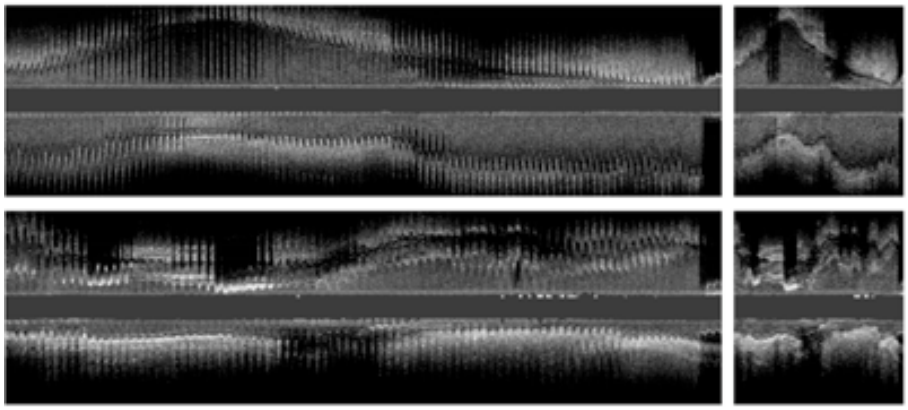

Figure 5.6: Results of Image-based ECG sampling for two different longitudinal cuts.

5.3 Vessel Structures

The set of optimal parameters for a Boston Clear View is given by:

$$PF1 = 0.1906X + 0.9817Y$$

with thresholding parameters set to:

$$\tau_{PF1} = 0.0567; \rho_X = 6\%; \rho_F = 85\%$$

for computation of vessel borders mask and

$$PF2 = -0.1498PF1 + 0.9887Z, \qquad \tau_{PF2} = -0.1241$$

for the calcium mask. The adventitia detection parameters ensure a 99.95% of true C_1 detections. We note that, by the feature space definition, we only have a 17% of false positives, which just represent 6% of the total number of points classified in C_1. This fact favors the use of a length filtering on adventitia detections as fake response remover. In the case of calcium extraction, the threshold achieves less than a 1% of noise and ensures 90.2156% of calcium detections. For the computation of the final B-snake model we have used 30 control points uniformly placed every 12 angles.

We have analyzed errors individually for each patient gathered by vessel plaque nature and globally. Whisker boxes are usual to analyze within patient variability and confident intervals serve to detect any significant difference between different plaques.

Figure 5.7 shows whisker boxes for mean distance absolute errors (top plot) and mean inter-observer variations (bottom plot) for soft plaque and calcium segments. Each box contains the mean distance errors obtained from the 4 experts segmentations (80 to 120 samples per box) for a single vessel segment. Boxes labeled with **NC** correspond to non-calcified segments and those labeled with **C** to calcified ones. An analysis of the whisker boxes reflects robustness of segmentations: the smaller the boxes are, the more reliable the method is. Whisker boxes serve to visually detect any anomaly in the models. In general terms, the means of automated errors are slightly higher than inter-observer variability means. However, since automatic segmentations present a significantly smaller variation range than inter-observer variability, our segmentations are within the experts discrepancy rate (see T-tests comparing means summarized in table 5.12. Lack of reliable information at large angular sectors, significantly increases errors variability in calcified segments,both for manual segmentations and automatic detections. The large range of the whisker box of the case C2 detects it as a vessel segment of difficult manual identification that should be excluded from any statistical analysis. Larger boxes for automated detections (top) in cases NC5 and C3 comparing to their counterparts (bottom) indicate that there are specially difficult cases for our segmenting strategy. At the end of the section, a detailed analysis of such miss detections is done.

Statistical ranges (mean $\pm$ standard deviation) for automatic errors (AUT) and inter-observer variability (INT-OBS) are summarized in tables 5.9, 5.10, and 5.11. Patients presenting an unusual large inter-observer variability have been excluded, since we consider they are anomalous cases with difficult and non robust manual

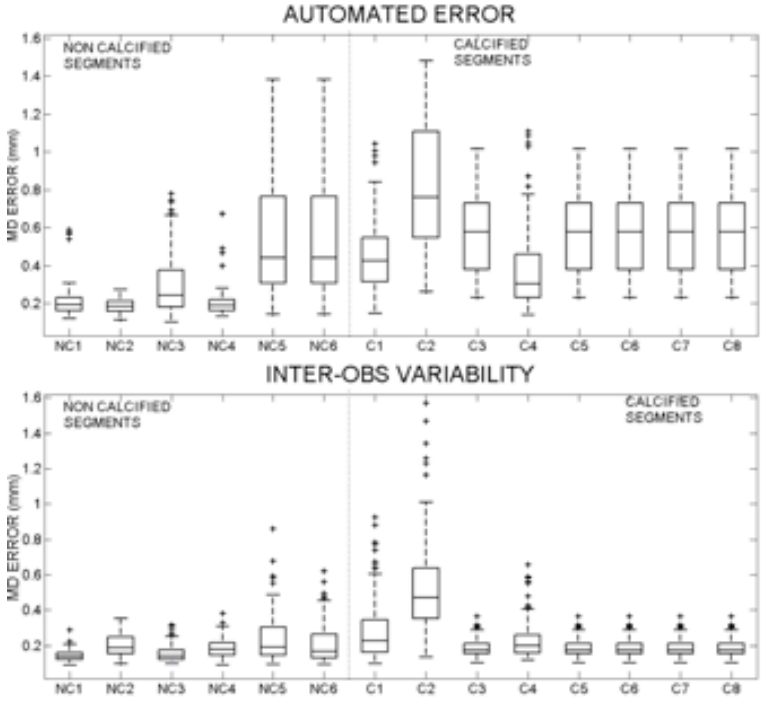

Figure 5.7: Whisker Boxes for Automated Error,(top), and Inter-Observer Variability, (bottom).

Table 5.9

Performance Evaluation of the Adventitia Segmentation Strategy. Automatic Errors versus Inter-Observer Variability for non-calcified

	INT-OBS	AUT
MaxD (mm)	0.4208 ± 0.1794	0.4238 ± 0.1026
RelMaxD (%)	0.3963 ± 0.1788	0.3868 ± 0.1075
MeanD (mm)	0.1783 ± 0.0698	0.1864 ± 0.0364
RelMeanD (%)	0.1647 ± 0.0668	0.1684 ± 0.0387
Area Dif. (%)	6.6799 ± 3.1579	7.2571 ± 1.9842
SgnMeanD (mm)	0.0004 ± 0.0769	0.0283 ± 0.0540

identification. We present statistics for non-calcified segments in table 5.9, calcified ones in table 5.10 and a total population of 20 vessel segments in table 5.11.

A summary of the results of the T-tests comparing the inter-observer variability

Table 5.10

Performance Evaluation of the Adventitia Segmentation Strategy. Automatic Errors versus Inter-Observer Variability for calcified segments

	INT-OBS	AUT
MaxD (mm)	0.6627 ± 0.3610	0.7161 ± 0.2532
RelMaxD (%)	0.5469 ± 0.3171	0.6116 ± 0.2665
MeanD (mm)	0.2650 ± 0.1306	0.2885 ± 0.0947
RelMeanD (%)	0.2142 ± 0.1113	0.2388 ± 0.0931
Area Dif. (%)	9.3511 ± 5.7529	10.0428 ± 4.0390
SgnMeanD (mm)	0.0163 ± 0.1213	-0.0381 ± 0.0912

Table 5.11

Performance Evaluation of the Adventitia Segmentation Strategy. Automatic Errors versus Inter-Observer Variability for all segments

	INT-OBS	AUT
MaxD (mm)	0.5386 ± 0.3075	0.5715 ± 0.2296
RelMaxD (%)	0.4697 ± 0.2664	0.5122 ± 0.2344
MeanD (mm)	**0.2206 ± 0.1126**	**0.2265 ± 0.0688**
RelMeanD (%)	0.1888 ± 0.0945	0.1972 ± 0.0662
Area Dif. (%)	**7.9813 ± 4.7962**	**8.6032 ± 3.3436**
SgnMeanD (mm)	0.0081 ± 0.1013	**0.0041 ± 0.0801**

and automatic errors averages is given in table 5.12. We report the p-value and the confidence interval for the difference in means. Statistics exclude outliers and T-tests are computed over the total errors in table 5.11.

According to a two tailed T-test, there is no significant difference between inter-observer and automated mean absolute distance errors and difference in areas. For mean distance errors the p-value equals $p = 0.177721$ and the confidence interval for the true difference in means at a significance level of 95% is $CI = (-0.002684, 0.014491)$. In the case of percentage in area difference, $p = 0.153404$ and the interval (also at a significance level of 95%) is $CI = (-0.017985, 0.114350)$. Maximum errors for automated detections are slightly above the range of maximum inter-observer variability. In order to robustly determine the fraction of increase, we use a single tailed T-test to check if the null hypothesis statement "the mean of automated maximum errors is above λ times the mean of maximum inter-observer variabilities" is true. The true proportion between maximum automated error and inter-observer variability is be-

Table 5.12
Statistics Summary on T-tests comparing the means of Inter-Observer Variability and Automatic Errors.

	Confidence Interval (CI)	p-value
MeanD	(-0.002684,0.014491)	0.177721
Area Dif.	(-0.017985,0.114350)	0.153404
SgnMeanD	(-0.002401,0.010787)	0.212219

tween the minimum λ rejecting the null hypothesis and the maximum accepting it. For $\lambda = 1.102$, the null hypothesis was accepted with a p-value, $p = 0.053901$ and for $\lambda = 1.103$, it was rejected with $p = 0.049846$. We conclude that the increase in maximum automated errors is under a 10.3%. Finally a T-test on the mean of the automated signed distance error shows that in average it is zero as the p-value equals $p = 0.212219$ and the confidence interval for the true mean is a tiny interval containing the zero value $CI = (-0.002401, 0.010787)$.

Some of the adventitia segmentations achieved with the presented strategy are shown in the next figures. We split them in four different cases: the first (figure 5.8) corresponds to normal vessel segments, the second (figure 5.9) to vessel segments with soft plaque. The third (figure 5.10) have been extracted from calcified vessel segments and finally, the last one (figure 5.11) shows images with missing information, mainly due to side branches and sensor guide shadows.

1. NORMAL SEGMENTS In the first column we present a normal segment, whereas in the second one, the vessel presents non-fibrous plaque.

2. SOFT PLAQUE SEGMENTS In the first column, we present a vessel segment with lipidic plaque, whereas, in the second column, the vessel segment contains soft plaque. Notice that in the anisotropic contour closing step (fig.5.9(l) to fig.5.9(m)) we use image borders continuity, since these images come from cartesian coordinates. Thus, although adventitia points before the ACC do not appear on the right of the image, ACC closes in the two directions from the left side of the image.

3. CALCIFIED PLAQUE SEGMENTS In this case, both vessels contain calcified plaque. Notice that, although intima is detected, both polar coordinates and a rigid snake, yield that the final closed model corresponds to the adventitia.

4. SIDE BRANCHES AND SENSOR SHADOW SEGMENTS Both vessel segments lack of information, the first due to a calcified area plus a side branch and the second column, because of sensor shadow and a little side branch. The key point of this kind of images is the sparse information, which we discuss in the next subsection.

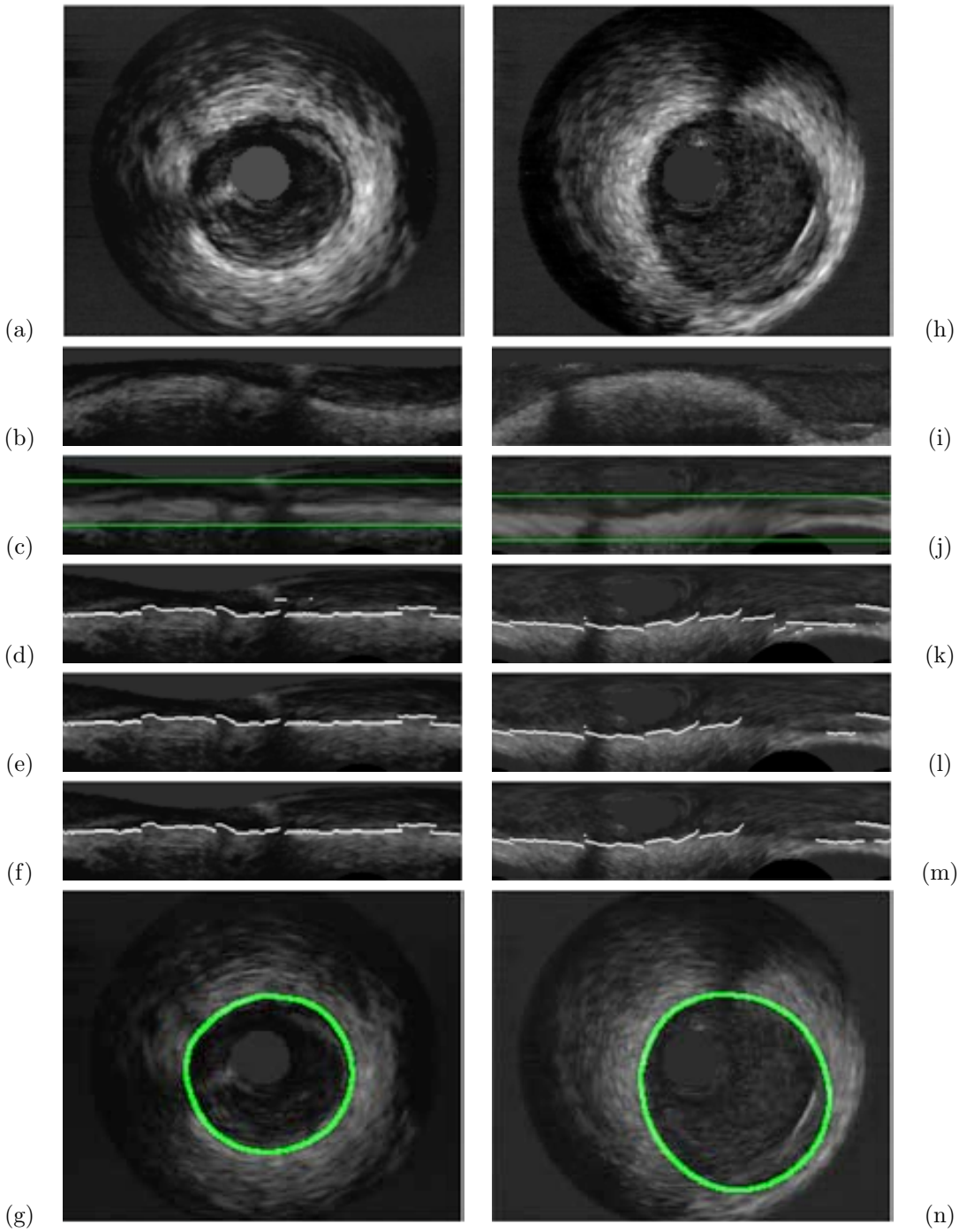

Figure 5.8: Automated Adventitia Detections for Normal Vessel Segments

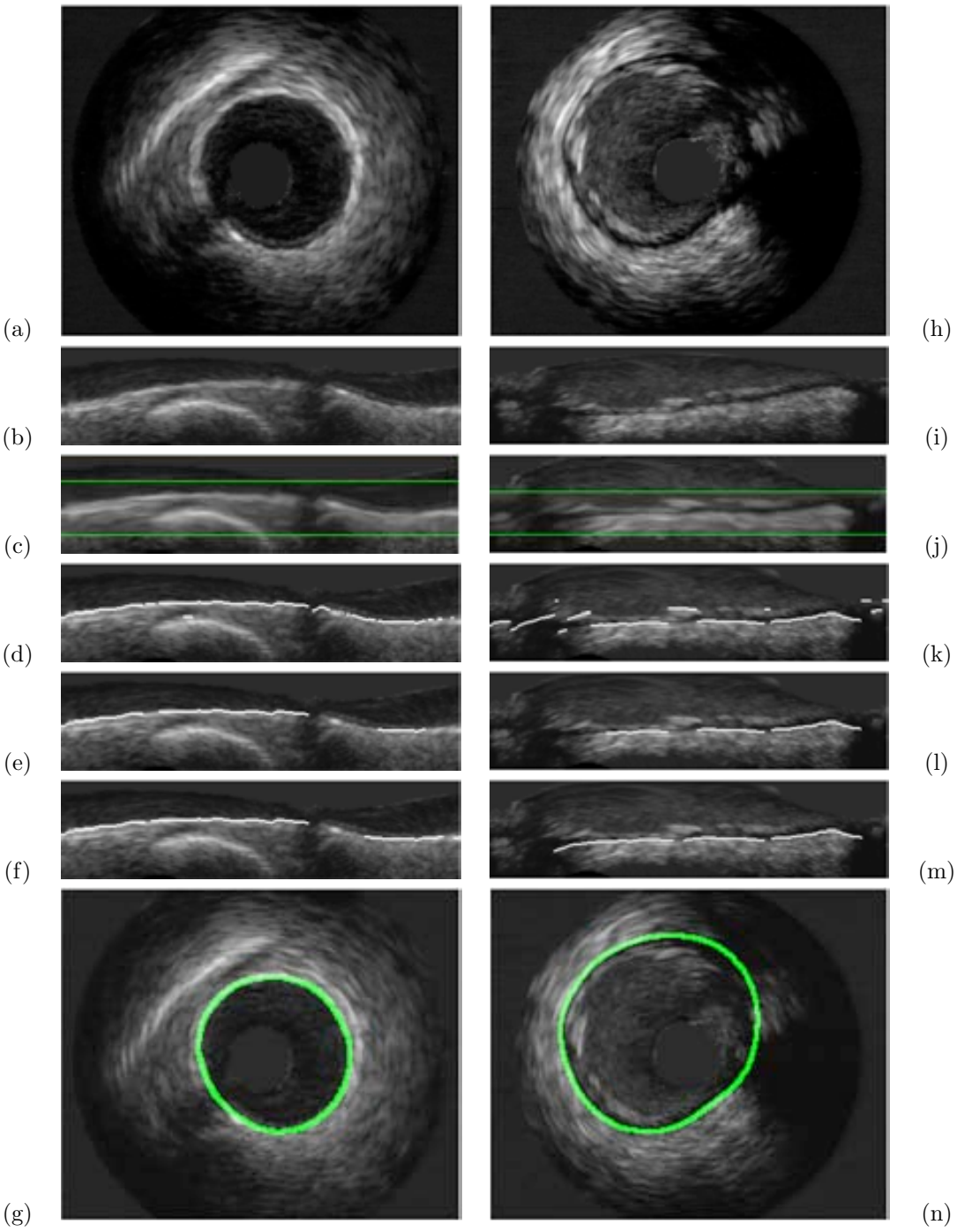

Figure 5.9: Automated Adventitia Detections for Vessel Segments with Soft Plaque

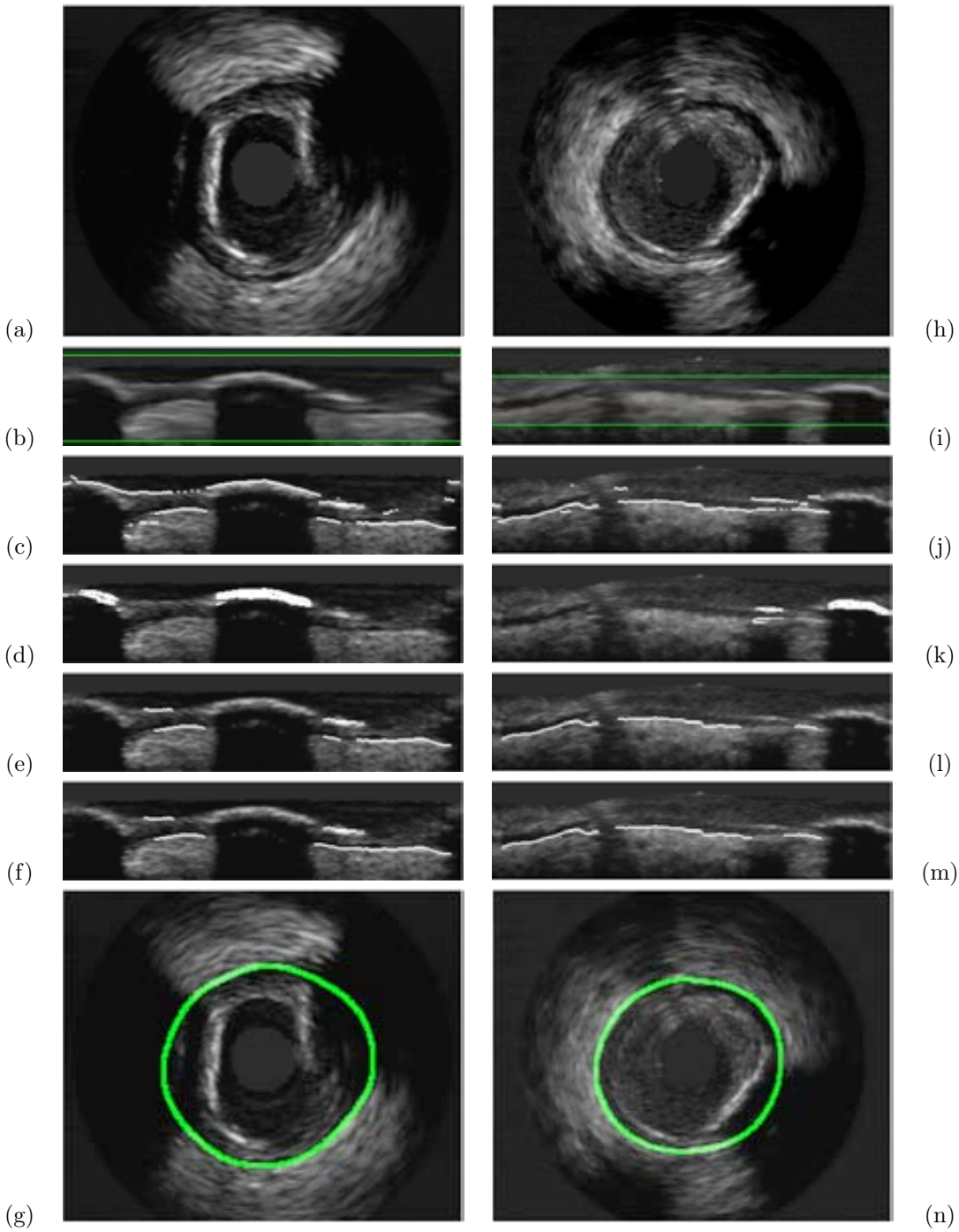

Figure 5.10: Automated Adventitia Detections for Calcified Vessel Segments

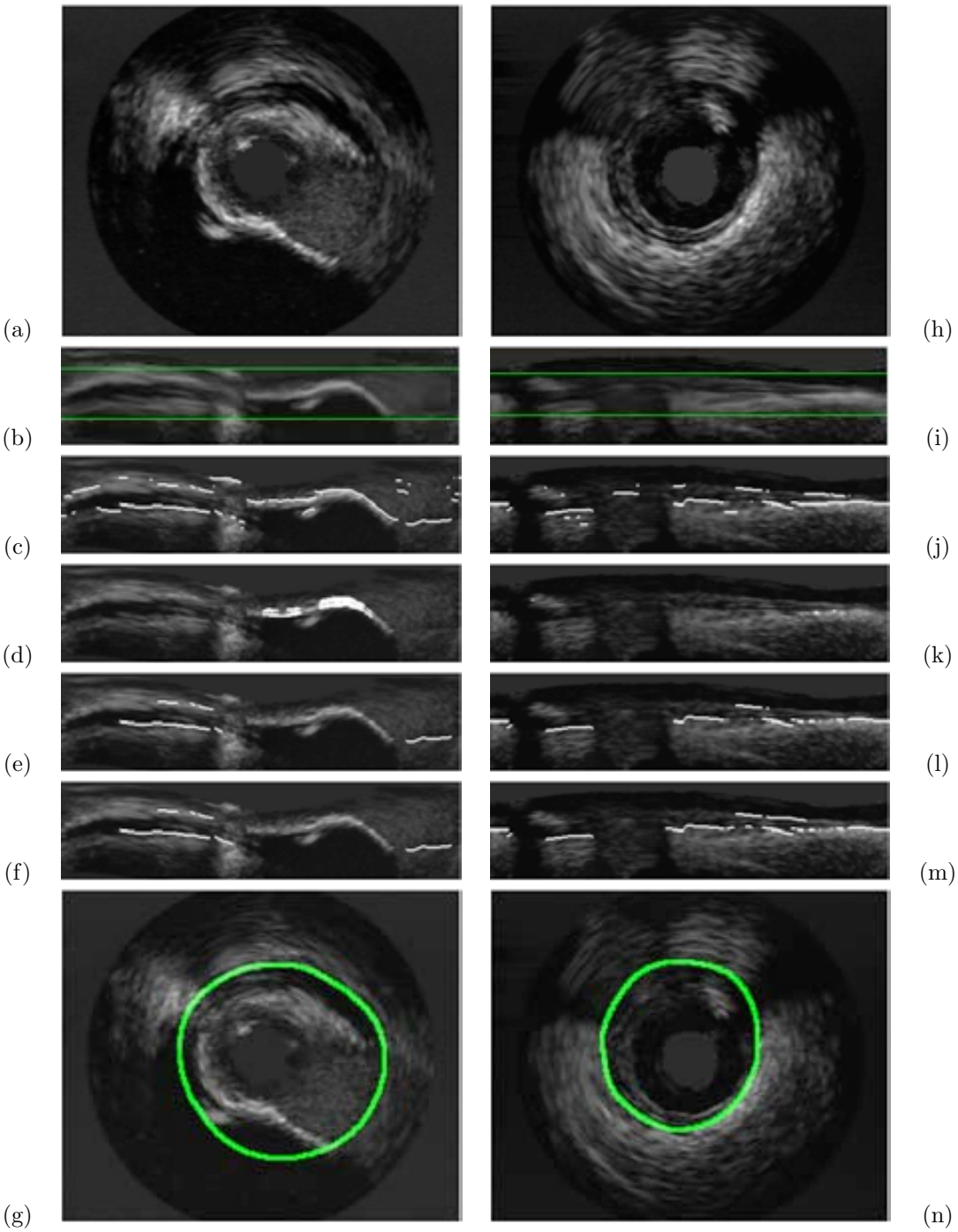

Figure 5.11: Automated Adventitia Detections for Uncomplete Vessel Segments

5.4 Discussion

By combining vessel appearance and shape, we provide explicit formulae for rigid in-plane motion parameters. This sets no limits to the capture range of motion parameters and we have equal performance (tables 5.1 and 5.2) for frame-to-frame steps of 1^o and 10^o. Translation is given (independently for each frame) in absolute terms, whereas rotation is computed by accumulating frame-to-frame transformations. In large segments, the latter might introduce accumulation errors. Alignment of large segments is a difficult task, due to morphological variations, which also might drop the accuracy of registration algorithms. Therefore, we consider that this does not represent a major limitation of our approach compared to registration strategies. Experiments on sequence-based synthetic models (table 5.3) show that the main source of error arises from morphological changes along the vessel, with average errors of 1.09 pixels $*$ 0.04 mm/pixel = 0.044mm for translations and 1.72^o for rotations. Our errors favorably compare to the numbers reported in [114], which achieve mean errors of 0.064mm and 7.8^o, provided that the catheter rotation does not exceed 5^o.

Our quality measure, CDR, bases on the conservation of the image local density of mass (given by the local mean) and only considers image pixels with noticeable motion. Results on Sequence models (table 5.4) show that CDR correlates to the angular relative accuracy. Results on real pullbacks show that, in general, CDR also correlates to the uniform and continuous appearance of longitudinal cuts (see figure 5.3(a), (b), and (d)). This fact validates CDR as an objective measure of image alignment. Comparison to global similarity scores, such as cross-correlation (table 5.5), indicates that global approaches are prone to underestimate motion reduction.

Experimental results detect two sources for under performance of the proposed methodology: sudden morphological changes and non-periodic random motion patterns. In the first case, which is a common limitation in most registration and tracking algorithms, changes in appearance mislead image alignment as the objects to be tracked have significantly changed. The second source of error is inherent to the definition of rigid (periodic) movement, which is the only motion considered. These extreme cases, which CDR might drop to 63%, only represent a 6% of the data analyzed.

Regarding longitudinal dynamics assessment, cardiac phase can be strongly affected by artery lesions and other cardiac factors. Thus, the strategy used to retrieve it has to be accurately chosen. We propose two different methods for extracting cardiac signal and a battery of filters to remove noise and other non-cardiac phenomena. Local approaches allow simple quantities (e.g. image intensity) efficiently (36ms per frame) retrieve an accurate cardiac phase. Band pass filters support should not be too restricted around ω_c in order to avoid uniform samplings. For segments of approximately 1 cm average length, the decay of Gaussian filters is better suited with an error within 0.054 ± 0.025 mm.

Finally, the reliability of the proposed strategy for adventitia segmentation is reflected in the global statistics extracted from in vivo sequences segmentation. The fact that, both, mean distances and vessel areas compare to inter-observer variation validates our method for extraction of clinical measurements. Since there is no bias in automated segmentations (the mean signed distance is statistically zero) we can

ensure that our method achieves an optimal compromise among experts criteria as automatically traced curves lie between the curves traced by different observers. The number of outlier bad segmentations requiring manual correction represent less than a 15% of the studied valid cases.

Still, the striking increase in the error range for the anomalous cases NC5 and C3 needs to be analyzed. Such miss detections correspond to vessel segments that either the adventitia is hardly identified or there is severe lack of valid information.

Weak visual appearance of the adventitia border is a technical limitation of the UltraSound acquisition technique and it is cause of disagreement among experts (case C2 in fig.5.7(b)) in 9% of the cases. Our strategy suffers this kind of error in 18% of the segments under study (boxes C5, NC2 and NC3 in fig.5.7(a)). We argue that the only way to minimize the impact of border blurring is taking into account tissue motion periodicity along the sequence. Even for physicians it is difficult to identify vessel borders by an analysis of still images. Often, they use cardiac periodicity in the movement of vessel structures to distinguish between tissue and other structures.

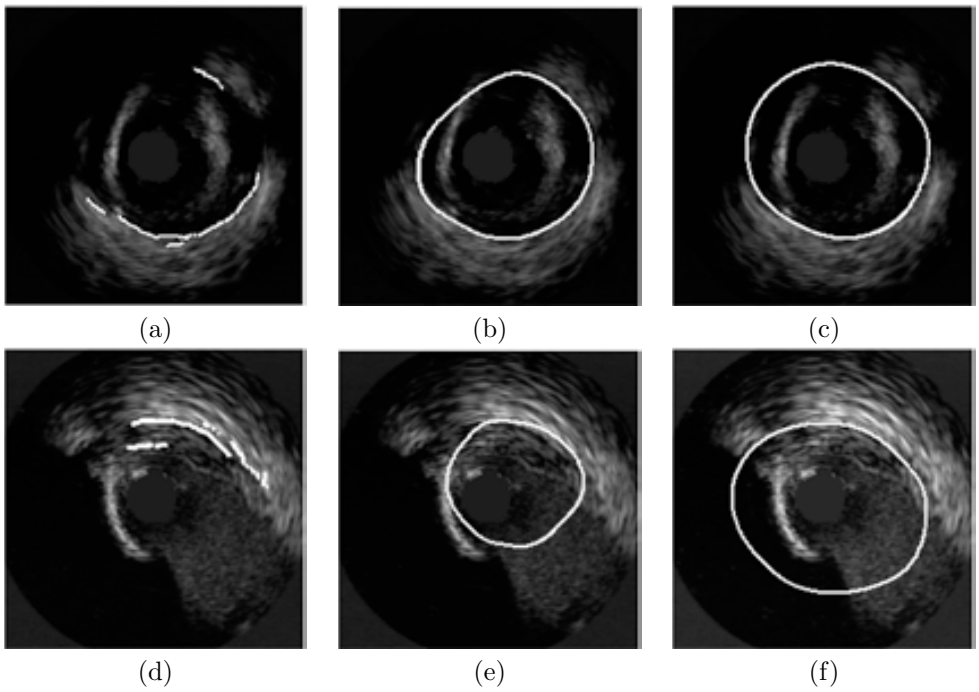

Figure 5.12: Adventitia models in images with sparse information. Points detected (a), (d), final snake (b), (e) and manual model (c), (f).

The second source of large error in automatic detections is lack of information. Calcium sectors or side branches can take up large angular sectors, thus, distorting information at these sectors. In the case that the sparse valid information is not uniformly distributed along angular sectors, the final model is prone to underestimate

the border true radial position. Fig.5.12 illustrates the scarce bad distributed information artifact. On the first column we show an image with uniformly enough point distribution and on the second column a pathological case with all available information gathered in the first quadrant of the image. Images in fig.5.12(a), (d) depict the ACC closure modeled by the B-snake in fig.5.12(b), (e). The reference manually traced contours are shown in fig.5.12(c), (f).

We note that it is reported in the literature [84] that measurements should not be reported if lack of information is more extensive than 90° of arc. Still our error analysis prompts that lack of strong 3D continuity in the B-snake closing of candidate points on the vessel borders is the main source of the above error. The use of 2D NURBS (spline surfaces) instead of 1D splines could reduce the impact of missing information. However, in our case, they might not succeed in correcting this kind of miss interpolations. On one hand, NURBS can only take into account local deformations and continuity of the surface. On the other hand, the previously described pathology is prone to happen at large vessel segments. It follows that NURBS interpolation might imply handling the segmentation of the whole image sequence block (over 1200 frames), which is computationally unfeasible. One possible way of overcoming lack of information for large vessel segments would be mimicking the experts strategy used for manually tracing the adventitia borders. Our application [115] to manually segment vessel borders shows the previous border on the current image to be segmented and allows the physician to modify it. An informal survey on the key points and frames used by the expert for border tracing at images with severe lack of information prompts that they usually keep the model traced on the last valid frame. This suggests using the information available at the last frame with adventitia points detected in more than 70% of the vessel angular sectors to complete vessel borders at images with sparse detections.

Conclusions and Further Lines

Image processing methodologies are becoming an important tool for using IntraVascular UltraSound for the diagnosis, treatment, and intervention of cardiovascular diseases. In this work we have approached three main challenging problems: rigid in-plane dynamics suppression, cardiac phase retrieval, and vessel-structures segmentation.

Rigid in-plane dynamics: We have described a method for estimating and compensating rigid in-plane dynamics. We have provided explicit formulae for motion parameters by combining vessel appearance and shape. Fourier development has shown to be a reliable tool for estimating rotation between consecutive frames as far as translation is well-estimated. As well, we have decomposed the rotation profile into its three main contributions: cardiac signal, breathing and geometric components. Results on synthetic experiments and *in vivo* segments show that the methods are suitable for exploring tissue bio-mechanical properties from *in vivo* clinical cases.

Longitudinal Dynamics: We have presented a methodology for retrieving cardiac phase from sequences without ECG signal. We have presented two different approaches to extract cardiac signal from IVUS sequences, as well as two families of filters for removing non-cardiac frequencies. On one hand, exploring LM evolution is a fast way to extract cardiac signal from IVUS sequences. On the other one, the profiles obtained from estimating cardiac rotation show that the algorithm seems to be a good candidate for globally retrieving cardiac signal. Regarding the filters used Band-pass filters support should not be too restricted around the main cardiac harmonic in order to avoid uniform samplings. For segments of approximately 1 cm average length, the decay of Gaussian filters is better suited.

Structures exploring: We have presented a statistical-deterministic strategy for detecting vessel borders in IVUS sequences. The combination of a priori knowledge (classification techniques) with filtering techniques based on continuity of image geometry has proven to be the key point for a robust characterization of vessel (the adventitia layer, in our case) borders. Once again, rigid in-plane dynamics estimation seems to be a straightforward method for previously filtering the sequence, although it can be less precise. By designing an accurate point selection strategy, we avoid human interaction and the use of longitudinal cuts and ECG-gated acquisitions.

Validation Protocols: Since validation is an essential part of any algorithm for ensuring a wide clinical applicability, we have taken special care in designing a validation protocol for each contribution. As well, since there is no objective measure for dynamics assessment in *in vivo* sequences, we have described a quantitative score to objectively assess the amount of motion suppressed.

Further Lines

The methods proposed in this PhD thesis pave the way for several studies.

1. **Vessel bio-mechanical properties:** Tissue bio-mechanical properties is an active research area due to its prediction potential. The main artifact hindering its assessment in coronary arteries is the in-plane rigid motion. Once the sequences are stabilized, tissue bio-mechanical properties can be investigated by applying an elastic motion estimation on segments with uniform kind of plaques. Furthermore, blood flow can also be explored as far as pixel precision allows to observe significant changes along the sequence.

2. **Objective validation of Longitudinal Dynamics:** Lumen area changes are related to cardiac phenomena, and its comparison to automated sampling encouraging. Nevertheless, samplings obtained from ECG signals are an objective ground truth for validating the method for retrieving cardiac phase.

3. **3D Reconstruction:** Although 3D reconstruction only from IVUS sequences is not feasible without an external reference system, segmentation of vessel structures is a first step towards the next dimension

4. **Structures and dynamics exploring workstation:** Rigid motion estimation seems to be a useful algorithm for exploring both, structures and cardiac dynamics. Preliminary results encourage an exhaustive validation for the assessment of motion estimation as the basis of a framework exploring vessel dynamics and structures. It would increase the computation efficiency of a workstation for helping physicians in diagnosing and treating cardiovascular diseases.

Bibliography

[1] V. Fuster, "Mechanisms leading to myocardial infarction: Insights from studies of vascular biology," *Circulation*, vol. 90, no. 4, pp. 2126–2146, October 1994.

[2] I. Kakadiaris, S. O'Malley, M. Vavuranakis, S. Carlier, R. Metcalfe, C. Hartley, E. Falk, and M. Naghavi, "Signal-processing approaches to risk assessment in coronary artery disease," *IEEE Signal Processing Magazine*, vol. 23, no. 6, pp. 59–62, Nov. 2006.

[3] E. Céspedes, C. Korte, and A. van der Steen, "Intraluminal ultrasonic palpation: assessment of local cross-sectional tissue stiffness," *Ultrasound Med. Biol.*, vol. 26, pp. 385–396, March 2000.

[4] J. Wentzel, R. Krams, J. H. Schuurbiers, J. Oomen, J. Kloet, W. van der Giessen, P. Serruys, and C. Slager, "Relationship between neointimal thickness and shear stress after wallstent implantation in human coronary arteries," *Circulation*, vol. 103, no. 13, pp. 1740–5, 2001.

[5] D. Cavaye, R. White, K. GE *et al.*, "Intravascular ultrasound imaging: The new standard for guidance and assessment of endovascular interventions," *J Clin Laser Med Surg*, vol. 10, no. 5, pp. 3349–353, 1992.

[6] I. Fontaine, M. Bertrand, and G. Cloutier, "A system-based approach to modelling the ultrasound signal backscattered by red blood cells," *Biophysical Journal*, vol. 77, no. 5, pp. 2387–2399, 1999.

[7] M. Rosales, P. Radeva, J. Mauri, and O. Pujol, "Simulation model of intravascular ultrasound images," in *MICCAI*, vol. 3217, Sept. 2004, pp. 200–7.

[8] G. Mintz, S. Niessen, W. Anderson, S. Bailey, R. Erbel, P. Fitzgerald, F. Pinto, K. Rosenfield, R. Siegel, E. Tuzcu, and P. Yock, "Acc clinical expert consensus document on standards for acquisition, measurement and reporting of intravascular ultrasound studies (IVUS)," *Journal of the American College of Cardiology*, vol. 37, no. 5, pp. 1478–92, 2001.

[9] A. Arbab-Zadeh, A. DeMaria, W. Penny, R. Russo, B. Kimura, and V. Bhargava, "Axial movement of the intravascular ultrasound probe during the cardiac cycle: implications for three-dimensional reconstruction and measurements of coronary dimensions," *Am. Heart J.*, vol. 138, pp. 865–872, 1999.

[10] P. Delachartre, C. Cachard, G. Finet, F. Gerfault, and D.Vray, "Modeling geometric artefacts in intravascular ultrasound imaging," *Ultrasound Med. Biol.*, vol. 25, no. 4, pp. 567–575, May 1999.

[11] N. Bruining, C. von Birgelen, P. J. de Feyter, J. Ligthart, W. Li, P. Serruys, and J. R. Roelandt, "ECG-gated versus nongated three-dimensional intracoronary ultrasound analysis: Implications for volumetric measurements," *Catheter Cardiovasc. Diagn.*, vol. 43, no. 3, pp. 254–260, Mar. 1998.

[12] C. von Birgelen, G. Mintz, A. Nicosia, D. P. Foley, W. J. van der Giessen, N. Bruining, S. Airiian, J. T. C. Roelandt, P. de Feyter, and P. Serruys, "Electrocardiogram-gated intravascular ultrasound image acquisition after coronary stent deployment facilitates on-line three-dimensional reconstruction and automated lumen quantification," *J. Amer. Coll. Cardiol.*, vol. 30, no. 2, pp. 436–443, Aug. 1997.

[13] S. Winter, R. Hamers, M. Degertekin, K.Tanabe, P. Lemos, P. Serruys, J. R. Roelandt, and N. Bruining, "Retrospective image-based gating of intracoronary ultrasound images for improved quantitative analysis: The intelligate method," *Catheter Cardiovasc. Interv.*, vol. 61, no. 1, pp. 84–94, Jan. 2004.

[14] A. Wahle, S. C. Mitchell, S. D. Ramaswamy, K. Chandran, and M. Sonka, "Four-dimensional coronary morphology and computational hemodynamics," in *SPIE Medical Imaging 2001: Image Processing Conference*, vol. 4322, February 2001, pp. 743–754.

[15] S. . Nadkarni, D. . Boughner, and A. . Fenster, "Image-based cardiac gating for three-dimensional intravascular ultrasound imaging," *Ultrasound in Medicine and Biology*, vol. 31, no. 1, pp. 53–63, 2005.

[16] H. Zhu, K. D. Oakeson, and M. H. Friedman, "Retrieval of cardiac phase from IVUS sequences," in *Medical Imaging 2003: Ultrasonic Imaging and Signal Processing*, vol. 5035, 2003, pp. 135–146.

[17] M. M. S. Matsumoto, P. A. Lemos, T. Yoneyama, and S. S. Furuie, "Cardiac phase detection in intravascular ultrasound images," in *Medical Imaging 2008: Ultrasonic Imaging and Signal Processing*, February 2008.

[18] I. A. K. Sean M. O'Malley, Morteza Naghavi, "Image-based frame gating for contrast-enhanced IVUS sequences," in *International Workshop on Computer Vision for Intravascular and Intracardiac Imaging, International Workshop on CVIII, MICCAI*, 2006.

[19] J. Barajas, K. L. Caballero, O. Rodriguez, and P. Radeva, "Cardiac phase extraction in IVUS sequences using 1-D gabor filters," in *29th Annual International Conference of the IEEE EMBS*, August 2007.

[20] J. Shaw, B. Kingwell, A. Walton, J. Cameron, P. Pillay, C. Gatzka, and A. Dart, "Determinants of coronary artery compliance in subjects with and without angiographic coronary artery disease," *JACC*, vol. 39(10), pp. 1637–1643, 2002.

[21] S. Nadkarni, H. Austin, and et al., "A pulsating coronary vessel phantom for two and three-dimensional intravascular ultrasound studies." *Ultrasound Med. Biol.*, vol. 29, no. 4, pp. 621–628, 2003.

[22] K. Y. E. Leung, R. Baldewsing, F. Mastik, J. Schaar, and D. Gisolf, "Motion compensation for intravascular ultrasound palpography," *IEEE Trans. UFFC*, vol. 53, pp. 1269–1280, 2006.

[23] A. Jeremias, C. Spies, N. A. Herity, E. Pomerantsev, P. G. Yock, P. J. Fitzgerald, and A. C. Yeung, "Coronary artery compliance and adaptive vessel remodelling in patients with stable and unstable coronary artery disease," *Heart*, vol. 84, pp. 314–319, 2000.

[24] C. L. de Korte, G. Pasterkamp, A. F. van der Steen, H. A. Woutman, and N. Bom, "Characterization of plaque components with intravascular ultrasound elastography in human femoral and coronary arteries in vitro," *Circulation*, vol. 102, pp. 617–623, 2000.

[25] Y. Shi, F. de Ana, S. Chetcuti, and M. O'Donell, "Motion artifact reduction for IVUS-based thermal strain imaging," *IEEE Trans. Ultrason. Ferroelect. Freq. Contr.*, vol. 52, pp. 1312–1319, August 2005.

[26] M. Danilouchkine, F. Mastik, and A. van der Steen, "A study of coronary artery rotational motion with dense scale-space optical flow in intravascular ultrasound," *Phys. Med. Biol.*, vol. 54, pp. 1397–1418, February 2009.

[27] Y. Saijo, A. Tanaka, N. Owada, Y. Akino, and S. Nitta, "Tissue velocity imaging of coronary artery by rotating-type intravascular ultrasound," *Ultrasonics*, vol. 42, pp. 753–757, 2004.

[28] B. Zitova and J. Flusser, "Image registration methods: a survey," *Image Vision Comput.*, vol. 21, no. 11, pp. 977–1000, Oct. 2003.

[29] A. Hernàndez, P. Radeva, A. Tovar, and D. Gil, "Vessel structures alignment by spectral analysis of IVUS," in *Computer Vision for Intravascular Imaging*, Oct. 2006, pp. 30–37.

[30] J. Dijkstra, G. Koning, J. Tuinenburg, P. Oemrawsingh, and J. Reiber, "Automatic border detection in intravascular ultrasound images for quantitative measurements of the vessel, lumen and stent parameters," in *Computer Assisted Radiology and Surgery - CARS 2001*, 2001, pp. 916–922.

[31] C. von Birgelen, C. Mario, W. Li, J. Schuurbiers, C. Slager, P. de Feyter, J. Roelandt, and P. Serruys, "Morphometric analysis in three-dimensional intracoronary ultrasound: An in vitro and in vivo study performed with a novel system for the contour detection of lumen and plaque," *Am. Heart Journal*, vol. 132, pp. 516–527, 1996.

[32] C. von Birgelen, G. S. Mintz, A. Nicosia, D. P. Foley, W. J. van der Giessen, N. Bruining, S. G. Airiian, J. R. T. C. Roelandt, P. J. de Feyter, and P. W.

Serruys, "Electrocardiogram-gated intravascular ultrasound image acquisition after coronary stent deployment facilitates on-line three-dimensional reconstruction and automated lumen quantification," *J. Amer. Coll. Cardiol.*, vol. 30, pp. 436–443, 1997.

[33] M. Sonka, X. Zhang, S. C. DeJong, S. M. Collins, and C. McKay, "Automated detection of coronary wall and plaque borders in ECG-gated intravascular ultrasound pullback sequences (abstract)," *Circulation*, vol. 94, pp. 1—-653, 1996.

[34] P. Brathwaite, K. Chandran, D. McPherson, and E. Dove, "Lumen detection in human IVUS images using region-growing," in *Computers in Cardiology*, 1996, pp. 37–40.

[35] D. Gil, P. Radeva, and J. Saludes, "Segmentation of artery wall in coronary IVUS images: a probabilistic approach," in *Intern. Conf. Pat. Recog.*, 2000, pp. 352–355.

[36] P. Brathwaite and K. C. D. McPherson, "3D IVUS border detection in highly diseased arteries with dissecting flaps," in *Comp. in Card.*, 1998, pp. 157–160.

[37] Z. Luo, Y. Wang, and W. Wang, "Estimating coronary artery lumen area with optimization-based contour detection," *IEEE Transactions on Medical Imaging*, vol. 22, no. 4, pp. 564–566, 2003.

[38] E. Brusseau, C. de Korte, F. Mastik, J. Schaar, and A. F. W. van der Steen, "Fully automatic luminal contour segmentation in intracoronary ultrasound imaging: A statistical approach," *IEEE Trans. Med. Imag*, vol. 23, no. 5, 2004.

[39] G. Mendizabal-Ruiz, M. Rivera, and I. Kakadiaris, "A probabilistic segmentation method for the identification of luminal borders in intravascular ultrasound images," in *IEEE Conference on Computer Vision and Pattern Recognition. CVPR 2008.*, June 2008, pp. 1–8.

[40] C. J. Bouma, W. J. Niessen, K. J. Zuiderveld, E. J. Gussenhoven, and M. A. Viergever, "Automated lumen definition from 30 MHz intravascular ultrasound images," *Med. Image Anal*, vol. 1, pp. 363–377, September 1997.

[41] M. Hansen, J. Møller, and F. Tøgersen, "Bayesian contour detection in a time series of ultrasound images through dynamic deformable template models," *Biostatistics*, vol. 3, no. 2, pp. 213–228, 2002.

[42] M. Sonka, X. Zhang, and M. Siebes, "Segmentation of intravascular ultrasound images: A knowledge based approach," *IEEE Med. Imag.*, vol. 14, pp. 719–732, 1995.

[43] M. E. Olszewski, A. Wahle, S. C. Mitchell, and M. Sonka, "Segmentation of intravascular ultrasound images: a machine learning approach mimicking human vision," in *CARS*, 2004, pp. 1045–1049.

[44] O. Pujol and P. Radeva, *Handbook of Medical Image Analysis: Advanced Segmentation and Registration Models*. Kluwer Academic/ Plenum Publishers, 2005, pp. 57–110.

[45] C. Haas, H. Ermert, S. Holt, P. Grewe, A. Machraoui, and J. Barmeyer, "Segmentation of 3D intravascular ultrasonic images based on a random field model," *Ultrasound Med. Biol.*, vol. 26, no. 2, pp. 297–306, 2000.

[46] A. Takagi, K. Hibi, X. Zhang, T. J. Teo, H. N. Bonneau, P. G. Yock, and P. J. Fitzgerald, "Automated contour detection for high-frequency IVUS imaging: a technique with blood noise reduction for edge enhancement," *Ultrasound Med. Biol.*, vol. 26, no. 6, pp. 1033–1041, 2000.

[47] M. Plissiti, D. Fotiadis, L. Michalis, and G. Bozios, "An automated method for lumen and media-adventitia border detection in a sequence of IVUS frames," *IEEE Infor. Tech. Biomed.*, vol. 8, no. 2, pp. 131–141, 2004.

[48] J. Klingensmith, R. Shekhar, and D. Vince, "Evaluation of three-dimensional segmentation algorithms for the identification of luminal and medial-adventitial borders in intravascular ultrasound," *IEEE Med. Imag.*, vol. 19, no. 10, pp. 996–1011, 2000.

[49] J. Dijkstra, G. Koning, and J. Reiber, "Quantitative measurements in IVUS images," *Inter. Journal of Cardiovas. Imag.*, vol. 15, no. 6, pp. 513–522, 1999.

[50] A. Hernandez, D. Gil, P. Radeva, and E. Nofrerias, "Anisotropic processing of image structures for adventitia detection in IVUS images," in *Comp. in Card.*, vol. 31, Sep. 19–22, 2004, pp. 229–232.

[51] G. Unal, S. Bucher, S. Carlier, G. Slabaugh, T. Fang, and K. Tanaka, "Shape-driven segmentation of intravascular ultrasound images," in *Proc. of the International Workshop on Computer Vision for Intravascular Imaging (CVII), MICCAI*, October 2006, pp. 50–57.

[52] A. Taki, Z. Najafi, A. Roodaki, S. K. Setarehdan, R. A. Zoroofi, A. Konig, and N. Navab, "Automatic segmentation of calcified plaques and vessel borders in IVUS images," *Int J CARS*, vol. 3, pp. 347–354, June 2008.

[53] J. Weickert, "A review of nonlinear diffusion filtering," in *First International Conference on Scale-Space Theory in Computer Vision*, 1997, pp. 3–28.

[54] W. Young and S. McLaughlin, "Pseudo-inverse filtering of IVUS images," in *IEEE Proc. Science, Measurement and Technology*, vol. 145, 1998, pp. 321–326.

[55] X. Pardo, P. Radeva, and D. Cabello, "Discrimant snakes for 3D reconstruction of anatomical organs," *Med. Imag. Ana.*, vol. 7, pp. 293–310, 2003.

[56] D. Gil, A. Hernàndez, O. Rodriguez, J. Mauri, and P. Radeva, "Statistical strategy for anisotropic adventitia modelling in IVUS," *IEEE Transactions on Medical Imaging*, vol. 25, no. 6, pp. 768–778, 2006.

[57] D. Gil, "Geometric differential operators for shape modelling," Ph.D. dissertation, Universitat Autónoma de Barcelona, 2004. [Online]. Available: http://www.cvc.uab.es/~debora/

[58] D. Gil and P. Radeva, "Extending anisotropic operators to recover smooth shapes," *Comp. Vis. Imag. Unders.*, vol. 99, pp. 110–1257, 2005.

[59] T. Kapur, "Segmentation of brain tissue from magnetic resonance images," Master's thesis, Massachusetts Institute of Technology, February 1995.

[60] F. Lupotti, F. Mastik, S. Carlier, C. de Korte, W. van der Giessen, P. Serruys, and A. van der Steen, "Quantitative IVUS blood flow: validation in vitro, in animals and in patients," *Ultrasound Med. Biol.*, vol. 29, no. 4, pp. 507 – 515, 2003.

[61] S. Langeland, J. D'hooge, T. Claessens, P. Claus, P. Verdonck, P. Suetens, G. R. Sutherland, and B. Bijnens, "RF-based two-dimensional cardiac strain estimation: A validation study in a tissue-mimicking phantom," *IEEE transactions on ultrasonics, ferroelectrics, and frequency control*, vol. 51, no. 11, pp. 1537–1546, November 2005.

[62] P. Shi, A. Amini, G. Robinson, A. Sinusas, C. Constable, and J. Duncan, "Shape-based 4D left ventricular myocardial function analysis," in *Proceedings of the IEEE Workshop on Biomedical Image Analysis*, June 1994, pp. 88–97.

[63] J. Landis and G. Koch, "The measurement of observer agreement for categorical data," *Biometrics*, vol. 33, pp. 159—-174, 1977.

[64] G. Gerig, M. Jomier, and M. Chakos, "Valmet: A new validation tool for assessing and improving 3D object segmentation," in *MICCAI 2001*, 2001, pp. 516–528.

[65] M. Rosales, P. Radeva, O. Rodriguez, and D. Gil, "Suppression of IVUS image rotation. a kinematic approach," in *FIMH*, vol. 3504, 2005, pp. 359–368.

[66] R. A. Baldewsing, J. A. Schaar, F. Mastik, C. W. J. Oomens, and A. F. W. van der Steen, "Assessment of vulnerable plaque composition by matching the deformation of a parametric plaque model to measured plaque deformation," *IEEE Transactions on Medical Imaging*, vol. 24, no. 4, pp. 514–528, April 2005.

[67] G. D. Giannoglou, Y. S. Chatzizisis, G. Sianos, D. Tsikaderis, A. Matakos, V. Koutkias, P. Diamantopoulos, N. Maglaveras, G. E. Parcharidis, and G. E. Louridas, "In-vivo validation of spatially correct three-dimensional reconstruction of human coronary arteries by integrating intravascular ultrasound and biplane angiography," *Coronary Artery Disease*, vol. 17, no. 6, pp. 533–543, September 2006.

[68] M. Brejl and M. Sonka, "Object localization and border detection criteria design in edge-based image segmentation: Automated learning from examples," *IEEE Transactions on Medical Imaging*, vol. 19 (10), pp. 973–985, October 2000.

[69] S. E. Hardt, A. Just, R. Bekeredjian, W. K. bler, H. R. Kirchheim, and H. F. Kuecherer, "Aortic pressure-diameter relationship assessed by intravascular ultrasound: experimental validation in dogs," *Am J Physiol Heart Circ Physiol*, vol. 276, no. 3, pp. 1078 – 1085, March 1999.

[70] S. Whitaker, *Introduction to Fluid Mechanics*. Krieger Pub Co, 1992.

[71] J. Mazumdar, *Biofluids Mechanics*. World Scientific Publishing, 1992.

[72] G. Holzapfel, T. Gasser, and M. Stadler, "A structural model for the viscoelastic behavior of arterial walls: continuum formulation and finite element analysis," *Eur. J. Mech. A-Solids*, vol. 23, pp. 1–162, 2002.

[73] E. Waks, J. Prince, and S. Andrew, "Cardiac motion simulator for tagged MRI," in *IEEE Proceedings of MMBIA*, 1996.

[74] S. Lang, *Linear Algebra*. Addison Wesley, 1971.

[75] S. Mallat, *A Wavelet Tour of Signal Processing*. Academic Press, 1998.

[76] L. Evans, *Partial Differential Equations*. Berkeley Math. Lect. Notes, 1993.

[77] K.Chen, "Adaptive smoothing via contextual and local discontinuities," *IEEE Trans. Pat. Ana. Mach. Intel.*, vol. 27(10), pp. 1552–1567, 2005.

[78] K. Mikolajczyk, T. Tuytelaars, C. Schmid, and et. al., "A comparison of affine region detectors," *Int. J. Comp. Vis.*, vol. 65, pp. 43–72, 2005.

[79] B. Jähne, *Spatio-temporal image processing*. Lecture Notes in Comp. Science, 1993.

[80] M. Spivak, *Calculus*, 3rd ed., C. U. Press, Ed., 2006.

[81] W. Pratt, *Digital Image Processing*, 2nd ed. New York: Wiley, 1991.

[82] V. Caselles, R. Kimmel, and G. Sapiro, "Geodesic active contours," *Int. Journal of Comp. Vis.*, vol. 22, no. 1, pp. 61–79, 1997.

[83] H. Goldstein, C. Poole, and J. Safko, *Classical Mechanics*, 3rd ed. Addison Wesley, 2002.

[84] G. Mintz and S. Nissen, "Clinical expert consensus document on standards for acquisition, measurement and reporting of intravascular ultrasound studies (IVUS)," *J. Am. Coll. of Card.*, vol. 37, no. 5, pp. 1478–92, 2001.

[85] K. Caballero, J. Barajas, O. Pujol, N. Salvatella, and P. Radeva, "In-vivo IVUS tissue classification: A comparison between RF signal analysis and reconstructed images," in *Progress in Pattern Recognition, Image Analysis and Applications*, vol. 4225, Nov. 2006, pp. 137–146.

[86] M. D. Rosales, "A physics-based image modelling of IVUS as a geometric and kinematics system," Ph.D. dissertation, Universitat Autònoma de Barcelona, 2005.

[87] A. Oppenheim and A. Willsky, *Signals and Systems*, 2nd ed. Englewood Cliffs, NJ: Prentice-Hall, 1997.

[88] C. Kuglin and D. Hines, "The phase correlation image alignment method," in *Int. Conf. on Cybernetics and Society*, 1975, pp. 163–165.

[89] S. Alliney, "Spatial registration of multiespectral and multitemporal digital imagery using fast-fourier transform techniques," *IEEE PAMI*, vol. 15, no. 5, pp. 499–504, 1993.

[90] D. Rotger, P. Radeva, and O. Rodriguez, "Vessel tortuosity extraction from IVUS images," in *Comp. in Card.*, Sept. 2006, pp. 689–692.

[91] D. Gil, O. Rodriguez-Leor, P. Radeva, and J. Mauri, "Myocardial perfusion characterization from contrast angiography spectral distribution," *IEEE Trans. on Med. Imag.*, vol. 27, no. 5, pp. 641–649, 2008.

[92] J. C. Russ, *The Image Processing Handbook*, 5th ed. CRC Press, 2002.

[93] R. Duda and P. Hart, *Pattern Classification*. Wiley-Interscience, 2001.

[94] A. Klug and D. J. DeRosier, "Optical filtering of electron micrographs: reconstruction of one-sided images," *Nature*, vol. 212, pp. 29–32, 1966.

[95] T. R. C. Johnson, K. Nikolaou, B. Wintersperger, A. Leber, F. von Ziegler, C. Rist, S. Buhmann, A. Knez, M. F. Reiser, and C. Becker, "Dual-source CT cardiac imaging: initial experience," *European Radiology*, vol. 16, pp. 1409 – 1415, 2006.

[96] M. Williams, R. Stewart, C. Low *et al.*, "Assessment of the mechanical properties of coronary arteries using intravascular ultrasound: an *in vivo* study," *Int J Card Imaging*, vol. 15, no. 4, pp. 157–160, 1999.

[97] J. Dodge, B. Brown, E. Bolson, and H. Dodge, "Lumen diameter of normal human coronary arteries. influence of age, sex, anatomic variation, and left ventricular hypertrophy or dilation," *Circulation*, vol. 86, no. 1, pp. 232–46, 1992.

[98] M. Brejl and M. Sonka, "Object localization and border detection criteria design in edge-based image segmentation: automated learning from examples," *IEEE. Transactions on Medical Imaging*, vol. 19, no. 10, pp. 973–985, 2000.

[99] T. F. Cootes, A. Hill, C. J. Taylor, and J. Haslam, "Use of active shape models for locating structures in medical images," *Imag. Vision Comput.*, vol. 12, pp. 355–365, 1994.

[100] R. Carmona and S. Zhong, "Adaptative smoothing respecting feature directions," *IEEE Imag. Proc.*, vol. 7, no. 3, 1998.

[101] G. Kanizsa, *Organization in Vision: Essays in Gestalt Continuation*. Praeger, 1979.

[102] D. Martin, C. Fowlkes, and J. Malik, "Learning to detect natural image boundaries using local brightness, color and texture cues," *IEEE PAMI*, vol. 26, pp. 1–20, 2004.

[103] F. Vilariño and P. Radeva, "Cardiac segmentation with discriminant active contours," in *Artificial Intelligence Research and Development*, 2003, pp. 211–215.

[104] P. Viola and W. Wells, "Alignment by maximization of mutual information," *Journal of Computer Vision*, vol. 24, pp. 137–154, 1997.

[105] J. P. W. Pluim, J. B. A. Maintz, and M. A. Viergever, "Mutual information based registration of medical images: a survey," *IEEE Transactions on Medical Imaging*, vol. 22, no. 8, pp. 986–1004, 2003.

[106] P. Rousseeuw and A. Leroy, *Robust Regression and Outlier Detection.* John Wiley and Sons, 1987.

[107] R. Burden and J. Faires, *Numerical Analysis.* Brooks-Cole, 2004.

[108] J. Demsar, "Statistical comparisons of classifiers over multiple data sets," *Journal of Machine Learning Research*, vol. 7, pp. 1–30, 2006.

[109] J. Zar, *Biostatistical Analysis.* Prentice Hall, 1998.

[110] D. Sheskin, *Handbook of parametric and nonparametric statistical procedures.* Chapman & Hall/CRC, 2000.

[111] R. Iman and J. Davenport, "Approximations of the critical region of the friedman statistic," in *Communications in Statistics*, 1980, pp. 571–595.

[112] P. Nemenyi, "Distribution-free multiple comparisons." Ph.D. dissertation, Princeton University, 1963.

[113] O. Dunn, "Multiple comparisons among means," *Journal of the American Statistical Association.*, vol. 56, no. 293, pp. 52–64, Mar. 1961.

[114] M. Danilouchkine, F. Mastik, and A. van der Steen, "Accuracy in prediction of catheter rotation in IVUS with feature-based optical flow; a phantom study," *IEEE Trans. Inf. Tech. in Biomedicine*, vol. 12, no. 3, pp. 356–365, 2008.

[115] D. Rotger, M. Rosales, J. García, O. Pujol, J. Mauri, and P. Radeva, "Activevessel: A new multimedia workstation for IVUS and angiography fusion," in *Comp. in Card.*, sep 2003, pp. 21–24.

Publications

Journal Papers

- A. Hernàndez-Sabaté, D. Gil, E. Fernandez-Nofrerias, P. Radeva, E. Martí, "Approaching Artery Rigid Dynamics in IVUS", IEEE Transactions on Medical Imaging, in press.

- D. Gil, A. Hernàndez, J. Mauri, P. Radeva, "A Deterministic-Statistic Strategy for Media-Adventitia Border Modeling in IVUS sequences", IEEE Transactions on Medical Imaging , vol. 25, n.6, June 2006.

- O. Rodríguez, J. Mauri, E. Fernández, A. Tovar, V. Valle, A. Hernàndez, D. Gil, P. Radeva, "Utilización de la estructura de los campos vectoriales para la detección de la adventicia en imágenes de ecografía intracoronaria", Revista Española de Cardiología , Octubre 2004; vol. 57(Supl. 2), pg. 100.

- O. Rodríguez, A. Carol, H. Tizón, E. Fernández, J. Mauri, V. Valle, D. Gil, A. Hernàndez, P. Radeva, " Model estadístic-determinístic per la segmentació de l'adventícia en imatges d'ecografia intracoronària ", Rev. Soc. Cat. Cardiol. Vol. 5, nº4, supl., pàg. 41.

Conference papers

- Debora Gil, Aura Hernàndez-Sabaté, Mireia Brunat, Jordi Martínez-Vilalta, Steven Jansen, "Structure-Preserving Smoothing of Biomedical Images", In Proc. of the 13th International Conference on Computer Analysis of Images and Patterns (CAIP'2009) , Münster, Germany, September 2009, *accepted*.

- Aura Hernàndez-Sabaté, David Rotger, Debora Gil, "Image-based ECG Sampling of IVUS Sequences", In Proc. of the 2008 IEEE International Ultrasonics Symposium , Beijing, November 2008, pp. 1330-1333.

- Debora Gil, Petia Radeva, Oriol Rodriguez-Leor, Aura Hernàndez, "Assessing Artery Motion Compensation in IVUS", In Proc. of the 12th International Conference on Computer Analysis of Images and Patterns (CAIP'2007) , Vienna, Austria, August 2007. LNCS 4673, pp. 213-220.

- Aura Hernàndez, Oriol Rodriguez, Debora Gil, "Quantitative Assessment of Artery Motion Compensation in IVUS Sequences", In Computer Vision: Advances in Research and Development. Proc. of the 2nd CVC International Workshop (CVCRD '07), Bellaterra (Spain), October 2007, pp. 83-88.
- Aura Hernàndez, Debora Gil, " How Do Conservation Laws Define A Motion Suppression Score in in-vivo IVUS Sequences? ", In Proc. of the 2007 IEEE International Ultrasonics Symposium , New York, October 2007, pp. 2231-2234.
- F. Guirado, A. Ripoll, C. Roig, A. Hernàndez, E. Luque, "Exploiting throughout for pipeline execution in streaming image processing applications", Euro-Par 2006, Parallel Processing, 12th International Euro-Par Conference , LNCS 4128 , Dresden, Germany, Sept. 2006, pp. 1095-1105.
- A. Hernàndez, D. Gil, J. Mauri, P. Radeva, "Reducing Cardiac Motion in IVUS Sequences", Computers in Cardiology 2006 , Valencia, Spain, 2006, pp. 685-688.
- A. Hernàndez, P. Radeva, A. Tovar, D. Gil, "Vessel Structures Alignment by Spectral Analysis of IVUS Sequences", The 1st International Workshop on Computer Vision for Intravascular and Intracardiac Imaging , MICCAI, 2006, pp. 29-36.
- P. Fritzsche, C. Roig, A. Ripoll, E. Luque and A. Hernández, "A Performance Prediction Methodology for Data-dependent Parallel Applications", In IEEE International Conference on Cluster Computing, September 2006, pp. 1-8.
- D. Gil, A. Hernàndez, A. Carol, O. Rodríguez, P. Radeva, " A deterministic-statistic adventitia detection in IVUS images", Functional Imaging and Modeling of the Heart 2005, LNCS 3504, Barcelona, Spain, June 2:4, pp. 65—74, 2005 .
- A. Hernàndez, D. Gil, P. Radeva, "On the usefulness of supervised learning for vessel border detection in IntraVascular Imaging", Frontiers in artificial intelligence and applications, IOS Press, pp 67—74, 2005.
- O. Rodríguez, J. Mauri, E. Fernández, A. Carol, V. Valle Tudela, D. Gil, A. Hernàndez, P. Radeva., " A deterministic-statistic adventitia modeling IVUS images ", ESC Congress 2005 , Stockholm.
- A. Hernàndez, D. Gil, P. Radeva , "Anisotropic Processing of Image Structures for Adventitia Detection in intravascular Ultrasound Images", Computers in Cardiology, vol. 31, pp. 229-232, Chicago (USA).

Technical Reports

- A. Hernàndez, D. Gil, P. Radeva, "A Deterministic-Statistical Strategy for Adventitia Segmentation in IVUS images", CVC Tech. Report n 89 , August 2005.
- A. Hernàndez, " Automatic adventitia segmentation in IntraVascular UltraSound images" , CVC Tech. Report, n85, August 2005.